The interaction of hydrogen with CeO$_2$ (111)/Ru (0001) and surface action spectroscopy: setup and first experiments

vorgelegt von

M. Sc.

Agata Plucienik

von der Fakultät II – Mathematik und Naturwissenschaften

der Technischen Universität Berlin

zur Erlangung des akademischen Grades

Doktor der Naturwissenschaften

Dr. rer nat.

genehmigte Dissertation

Promotionsausschuss:

Vorsitzender: Prof. Dr. Peter Hildebrandt

Gutachter: Prof. Dr. Hans-Joachim Freund

Gutachter: Prof. Dr. Reinhard Schomäcker

Tag der wissenschaftlichen Aussprache: 07. November 2019

Berlin 2019

Abstract

The first part of this thesis describes the setup of an apparatus for vibrational surface action spectroscopy as well as first experiments with this new method employing infrared radiation from the free electron laser of the Fritz Haber Institute. Vibrational action spectroscopy has been used previously mostly for the characterization of clusters in the gas phase. We have extended this method towards an application to solid surfaces with a $V_2O_3(0001)$ film on Au(111) as a model system for the first studies. This oxide has vanadyl groups at the surface but not in the bulk, and therefore these groups could be used to show that the method is surface sensitive.

The second part of my thesis treats the interaction of hydrogen with $CeO_2(111)$ thin films on Ru(0001). Experiments are carried out under UHV conditions using different surface science techniques such as low energy electron diffraction (LEED), thermal desorption spectroscopy (TDS), high resolution electron energy loss spectroscopy (HREELS) and scanning tunneling microscopy (STM). Cerium oxide (ceria) plays a crucial part in catalytic reactions due to its ability to store and release oxygen. There are many studies about the interaction of atomic hydrogen with ceria, but a comprehensive picture is still lacking. Hydrogen was dosed at pressures of at least 10 mbar in the studies discussed here. Stoichiometric $CeO_2(111)$ is not very much affected by exposure to hydrogen at room temperature, while, contrary to results found in the literature, exposure to reduced $CeO_2(111)$ does not lead to the formation of hydroxyl groups but to hydride species. Moreover, the Ce^{3+} in the reduced oxide is re-oxidized to Ce^{4+}. At elevated temperatures, hydrogen additionally reduces the sample. This thesis confirms that oxygen vacancies play an important role in the interaction of hydrogen molecules with $CeO_2(111)$, and it confirms that hydrogen may be stored as a hydride species in the oxide. The electronic and morphological changes through the hydrogenation process are discussed.

Zusammenfassung

Der erste Teil dieser Arbeit beschreibt den Aufbau einer Apparatur für die Schwingungs-Aktions-Spektroskopie von Oberflächen und erste Versuche mit dieser neuen Methode unter Verwendung von Infrarotstrahlung des Freie-Elektronen-Lasers des Fritz-Haber-Instituts. Schwingungs-Aktions-Spektroskopie wurde bisher hauptsächlich zur Charakterisierung von Clustern in der Gasphase eingesetzt. Wir haben die Methode für die Anwendung auf feste Oberflächen erweitert. Erste Studien wurden mit einem $V_2O_3(0001)$-Film auf Au(111) als Modellsystem durchgeführt. An der Oberfläche dieses Oxids befinden sich Vanadylgruppen, die sich aber nicht im Volumen finden. Daher konnten diese Gruppen verwendet werden, um zu zeigen, dass die Methode oberflächensensitiv ist.

Der zweite Teil meiner Arbeit befasst sich mit der Wechselwirkung von Wasserstoff mit $CeO_2(111)$-Dünnschichten auf Ru(0001). Die Experimente wurden unter UHV-Bedingungen unter Verwendung verschiedener oberflächensensitiver Techniken wie der Beugung niederenergetischer Elektronen (LEED), thermischer Desorptionsspektroskopie (TDS), hochauflösender Elektronenenergieverlustspektroskopie (HREELS) und Rastertunnelmikroskopie (STM) durchgeführt. Ceroxid (Ceria) spielt aufgrund seiner Fähigkeit, Sauerstoff zu speichern und freizusetzen, eine entscheidende Rolle bei katalytischen Reaktionen. Es gibt viele Studien zur Wechselwirkung von atomarem Wasserstoff mit Ceroxid, die aber bislang kein einheitliches Bild ergeben. In den hier diskutierten Studien wurde Wasserstoff bei Drücken von 10 mbar und mehr dosiert. Stöchiometrisches $CeO_2(111)$ wechselwirkt nicht nennenswert mit Wasserstoff bei Raumtemperatur, während die Wechselwirkung mit reduziertem $CeO_2(111)$ im Widerspruch zu Literaturberichten nicht zu Hydroxylgruppen, sondern zu einer

Hydridspezies führt. Darüber hinaus wird das Ce^{3+} im reduzierten Oxid zu Ce^{4+} oxidiert. Bei erhöhten Temperaturen reduziert Wasserstoff zusätzlich die Probe. Diese Arbeit zeigt, dass Sauerstofffehlstellen eine wichtige Rolle bei der Wechselwirkung von Wasserstoffmolekülen mit $CeO_2(111)$ spielen und dass Wasserstoff als Hydridspezies im Oxid gespeichert werden kann. Die elektronischen und morphologischen Veränderungen während des Hydrierungsprozesses werden diskutiert.

I am among those who think that science has great beauty. A scientist in his laboratory is not only a technician: he is also a child placed before natural phenomena which impress him like a fairy tale.

Maria Skłodowska-Curie

Table of content

1. Introduction.

1.1. Motivation.

Heterogeneous catalysis is a process of improving the rate of chemical reactions. It is also one of the pillars of the chemical industry. [1] To improve efficiency and comprehend the chemical reactions, it requires knowledge about catalytic materials on an atomic level. Surface science plays a major role in understanding complicated catalytic processes, as it analyses the physical and chemical processes occurring at the interface between solid, gas and vacuum. [2] On the one hand, conducting experiments under UHV conditions with reduced complexity of the catalytic process allows creating an environment, where particles (electrons, ions and atoms) employed in the surface science techniques are not scattered by residual gases. On the other hand, the UHV environment also creates the so-called *pressure gap* between the environmental conditions of technical catalysis and the UHV setup parameters. Due to that, the results obtained through surface science need to be carefully selected according to the needs of the chemical industry. To overcome this problem, one can introduce a high-pressure cell to the UHV setup. There, a sample can be treated under elevated pressure conditions and then transferred back to ultra-high vacuum for the following measurement; or the experiment can be conducted *in-situ* or *in-operando*. [3]

Heterogeneous catalysis studies may be challenging. Samples frequently have complicated morphology, various kinds and number of defects and deformed crystallographic surfaces. Furthermore, samples with a similar structure can vary depending on the preparation parameters such as temperature or pressure. Thus, sample analysis is highly demanding, but when performed properly- rewarding. Certain attention should be brought to metal oxides, commonly investigated in heterogeneous catalysis, where they not only act as substrates but also actively take part in catalysis. [4]

Cerium oxide is an important compound, frequently used in the catalysis, for example in automotive catalysis. CeO_2 removes pollutants (carbon monoxide, nitric oxides and unburned hydrocarbons) from combustion exhaust as well as it actively influences the production of dihydrogen from ethanol and ethanol-water mixtures. [5] The catalytic properties of cerium dioxide are associated with its oxygen storage capacity or in other words, cerium can store and easily release oxygen in a reversible way. Apart from oxidation reactions, pure cerium is not that commonly used in the heterogeneous catalysis. [6] Regarding the interactions with hydrogen, various groups published both experimental [7] [8] and theoretical [9] evidence that H_2 dissociates on CeO_2 (111) surfaces with a low activation barrier (0.2 eV), forming hydroxyl groups. Perez-Ramires *et al.* [10] reported the partial hydrogenation of alkynes to olefins. The yield of this reaction was highly influenced by the degree of surface reduction. As reported by Mullins [5] stoichiometric CeO_2 (111) surface has higher activity in selective hydrogenation than CeO_2 (100), since the (111) structure is naturally richer in vacancies. [5] This behaviour suggests, that the amount of oxygen vacancies influences the hydrogenation process. To study this aspect, a model system is required where the amount of CeO_2 defects can be controlled. As reduced cerium dioxide is highly susceptible to contaminations, an ultrahigh vacuum (UHV) environment is required. In this thesis, the interaction of H_2

with stoichiometric CeO_2 (111) and reduced CeO_{2-x} on Ru (0001) as a model system was studied.

Another complex issue, which surface science may contribute to is the interaction of adsorbed species with the surface. For many years, vibrational and structural properties of gas-phase aggregates have been studied using vibrational action spectroscopy employing infrared radiation from a free-electron laser. [11] Yet, such experiments have not been conducted at solid samples. Most of the surface science methods are not well suited for examining clusters deposited on the surface. From STM one can learn only the state of the top layer, while IRAS and HREELS are not surface sensitive enough to record vibrational data of metal clusters in the presence of an oxide substrate. [12] In the Fritz Haber Institute a new apparatus was constructed to apply vibrational surface action spectroscopy (SAS) employing infrared radiation from a free-electron for the first time. In the thesis, the first results of this technique are presented. The surface sensitivity of the method was examined by detecting the characteristic vanadyl groups (V=O) vibration at the surface of V_2O_3 (0001) films on Au (111).

1.2. Thesis organization.

This work is organized as follows. Basic techniques used during the experiments, as well as the physical concepts helping to understand them, are explained in Chapter 2. Chapter 3 is devoted to a detailed description of all three experimental setups. In order to conduct surface action spectroscopy experiments, a new set up had to be constructed. The construction, including crucial modifications of the QMS as well as the manipulator is explained. The work dedicated to the interaction of hydrogen with CeO_2, was performed first in a UHV system, where the main component was an HREEL spectrometer, followed by experiments in the system equipped with STM. The results section is divided into two

parts. First, in Chapter 4 the results obtained using the Free Electron Laser are described. The next part starts with the characterization of CeO_2 (111) in Chapter 5, followed by a discussion of the effect of exposure to 10 mbar of H_2 at room temperature (Chapter 6) and at the elevated temperatures (Chapter 7). The studies were conducted with stoichiometric (Chapter 6.1) as well as with reduced samples (Chapter 6.2.), with different oxygen vacancy concentrations. High resolution electron energy loss spectroscopy (HREELS), supported with temperature programmed desorption (TPD) and low energy electron diffraction (LEED) were used for these experiments. Additionally, the morphology was studied with scanning tunnelling microscopy (STM). Finally, results are discussed in the light of density functional theory (DFT) (Chapter 7).

2. Basic techniques.

Here, most of the experimental methods used to obtain the results for the thesis are described. First, high resolution electron energy loss spectroscopy (HREELS) is discussed. The quality of the sample was controlled by Low Energy Electron Diffraction (LEED) and Temperature Program Desorption (TPD). For characterizing the morphology of the sample surface Scanning Tunnelling Microscopy (STM) was applied. The last part introduces Surface Action Spectroscopy using a Free Electron Laser.

2.1. High Resolution Electron Energy Loss Spectroscopy (HREELS)

High resolution electron energy loss spectroscopy (HREELS) is a method used for studying vibrational and electronic excitations at solid surfaces under UHV conditions. Moreover, the method can provide information about the chemical bonding and geometry of adsorbents. [13]

As shown in Fig. 1, electrons are generated in the electron source by heating a tungsten cathode. Next, through the set of lenses electrons are focused on the monochromators, where they increase their initial electron energy. Only electrons with previously chosen energy can pass through the monochromators. Then, the electrons are focused on the sample by a system of lenses, which help to improve the resolution. The scattered

electrons have around 10^{-3} lower flux than before scattering. After scattering, analyser

passes through electrons with a certain energy, which then are being transferred to a

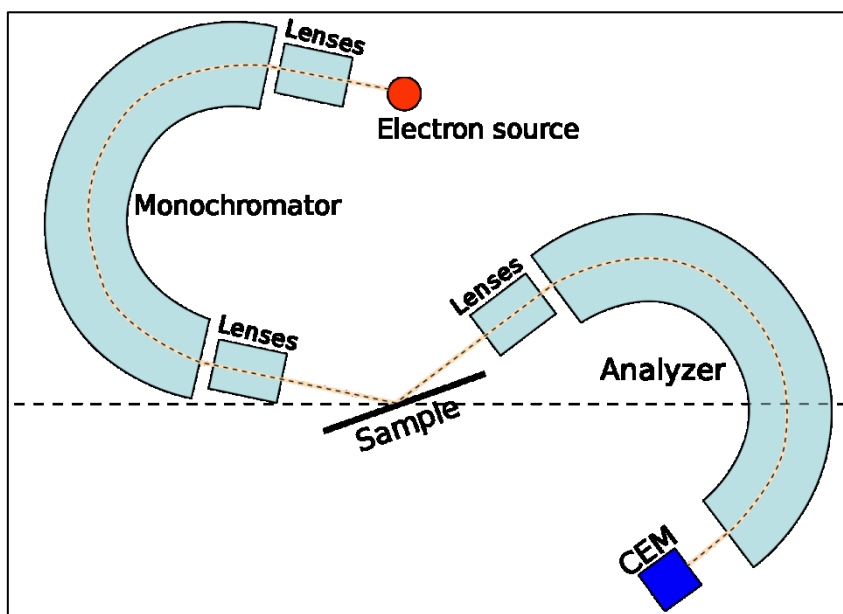channel electron multiplier (CEM), a detecting unit. [14]

Figure 1. Scheme of the HREELS setup. Adapted from [15].

 HREELS has a couple of advantages over other spectroscopic methods. In comparison

with infrared absorption spectroscopy (IRAS), it has a higher surface sensitivity and can

be used to analyse a wider range of vibrations (usually 5 to 500 meV). [13] Additionally,

in the IRAS spectroscopy two spectra are required, one for reference and one sample

spectrum. An IRAS spectrum is produced by the division of the sample spectrum by the

reference spectrum, hence, the bulk-related part of the spectrum is removed by the

division procedure. On the other hand, IRAS method has better resolution (1cm^{-1} against

1 meV). [1] Plus, since in HREELS electrons are being used, HREELS requires an

ultrahigh vacuum and relatively flat surface like single crystal or foil. The penetration

depth of electrons, in case of the kinetics energy from 20 to 200 eV, is in the range of 2-3 surface layers. [16]

When the electrons are being scattered on the sample surface, they may lose energy by exciting excitations at the substrate surface, by losing a certain amount of energy:

$$E=E_0-hv \qquad\qquad (2.1)$$

where:

E is the energy of the scattered electrons;

E_0 is the energy of the incident electrons;

h is the Planck's constant;

v is the frequency of the excited vibration.

The electrons can be scattered at the surface in an elastic or inelastic way. During elastic scattering, there is no transfer of energy between the particles, whereas during inelastic scattering at least one of the particles is losing part of its energy during the collision. In case of HREELS, in the course of the collision, the electron from the electron beam loses its part of the kinetic energy, which is then used for the excitation of the sample atoms. One can distinguish three inelastic scattering mechanisms in HREELS:

a) **Dipole scattering**- it is based on the excitation of a vibrational normal mode of an adsorbate, for example a molecule. Through the excitation, the electric dipole moment μ creates an electric field in the vacuum above the crystal, which scatters the incoming electron inelastically. The mechanism of dipole scattering can take place already when the electron is at far distance from the sample plane (around 100 Å). [13] In case

of molecules on non-metallic surfaces, the orientation of the dipole moment is not restricted; the mechanism only requires its change during excitation. Molecules on metals, on the other hand, are restricted by the metal-surface selection rule, which requires that only vibrations, which result in the dipole change perpendicular to the surface, can be observed in the specular mode. The reason is the higher frequency of metal electronic oscillations compared to the frequency of molecular vibrations (several eV compared to <0.6 eV). [17] The electrons at the surface can screen parallel vibrations by creating a dipole image in the opposite direction. As a result, the total oscillating dipole moment for the dipole moments perpendicular to the surface is double the strength; whereas for dipole moments parallel it is equal to 0 (see Fig. 2). Therefore, only molecules with a dynamic dipole perpendicular to the surface are detectable. The scattered electron wave loses the amount of energy equal to $h\nu$ [see the equation above] and is scattered mainly in the specular direction. [4]
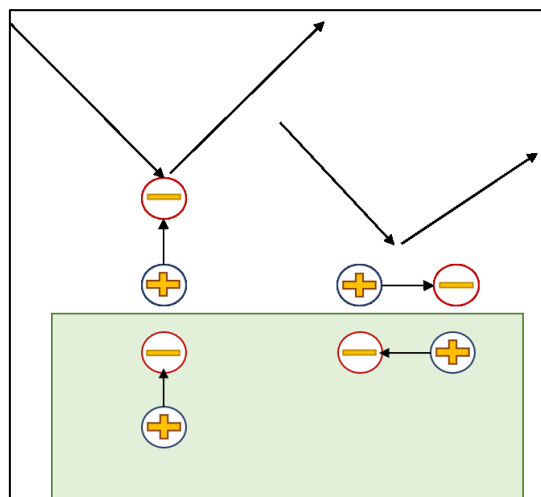

Figure 2. Schematic illustration of dipole scattering.

b) **Impact scattering** -occurs when low energy electrons collide with electrons of a substrate or adsorbate atoms, characterized by short-range direct Coulomb interaction. The angular distribution of the impact scattering is broad due to the large momentum

transfer and it is not focused in the specular direction. The scattering probability is described as follows [13]:

$$\frac{dP}{d\Omega} = \frac{mE_0}{2\pi^2\hbar^2} \frac{cos^2\theta_s}{cos\theta_0} S|M(k_0, k_s, q_{II}, u)|^2 \qquad (2.2)$$

Where E_0 is the primary kinetic energy, θ_S and θ_0 are impinging and scattering angles, m is the electron mass, S is the surface area hit by the beam and M is the multiple scattering element for an electron with initial wave vector k_0 into a state with final vector k_s. The E_0 factor indicates that scattering probability increases with kinetic energy. In case of impact scattering, the dipole moment change is not required, and all vibrations may be excited, apart from surface phonons. Sometimes the outgoing electrons detain energy from the excited molecules, leaving the surface with energy E_0 + $h\nu$, as in the dipole scattering. [18]

c) **Negative ion resonance (NIR)** –at low kinetic energy the incoming electron is trapped in the empty orbital above the vacuum level, which increases the probability of its energy loss. As a result, the potential energy surface (PES) changes. That change triggers the movement of nuclei, which aim to be in equilibrium position with respect to changed PES. Depending on the position of the created ion regarding the ground state of the neutral molecule, one can distinguish two kinds of resonance: *Shape* (ion above the ground state) and *Feshbach* (ion below the ground state). The NIR mechanism has the advantage of angular distribution in the emission and high intensity of the intermolecular vibrations. The mechanism of negative ion resonance is common for gas-phase scattering. [1]

The problematic case of the HREELS method is the presence of the intense optical surface phonons *(Fuchs-Kliewer* phonons). [17] On the one hand they provide crucial

information about the stoichiometry and structure of oxide surfaces. On the other hand, their intensity may produce overtones, blocking the weak vibrational modes of the adsorbed species. This effect can be minimized by using Fourier deconvolution and off-specular measurement. [19]

For the deconvolution of recorded spectra, the starting point is using the *Bose-Einstein* occupation factor *n(ω, T),* which describes the temperature dependence of loss function, do determine the loss function *p(ω, T)* at definite temperature *T* [20] :

$$p(\omega, T) = [1 + n(\omega, T)] \, p \, (\omega, 0) \tag{2.3}$$

The spectrum *s(ω)* consists of no single, but multiple loss events:

$$s(\omega) = i \, (\omega) * \left[\delta(0) + p(\omega, T) + \frac{1}{2!} p(\omega) * p(\omega) + \frac{1}{3!} p(\omega) * p(\omega) \, ... \right] \tag{2.4}$$

where:

i(ω) is an instrumental broadening function;

δ(ω) is the elastic peak;

* represents the convolution of two functions.

In the next step, it is important to remember that *a (ω)* after *Fourier* transformation has a form of *A* (τ) as well as * after transformation equals multiplication. The *Fourier* transform of the spectrum $S(\tau)$ can be shown as follows:

$$S(\tau) = I(\tau) \left[1 + P(\tau) + \frac{1}{2} P(\tau)^2 + \frac{1}{3} P(\tau)^3 + \cdots \right] \tag{2.5}$$

This sums up to expression for loss functions without multiple loss structure:

$$S(\tau) = I\,(\tau)\exp[P(\tau)] \qquad\qquad (2.6)$$

Followed by:

$$P(\tau)^2 = \log_e[S(\tau)/I(\tau)] \qquad\qquad (2.7)$$

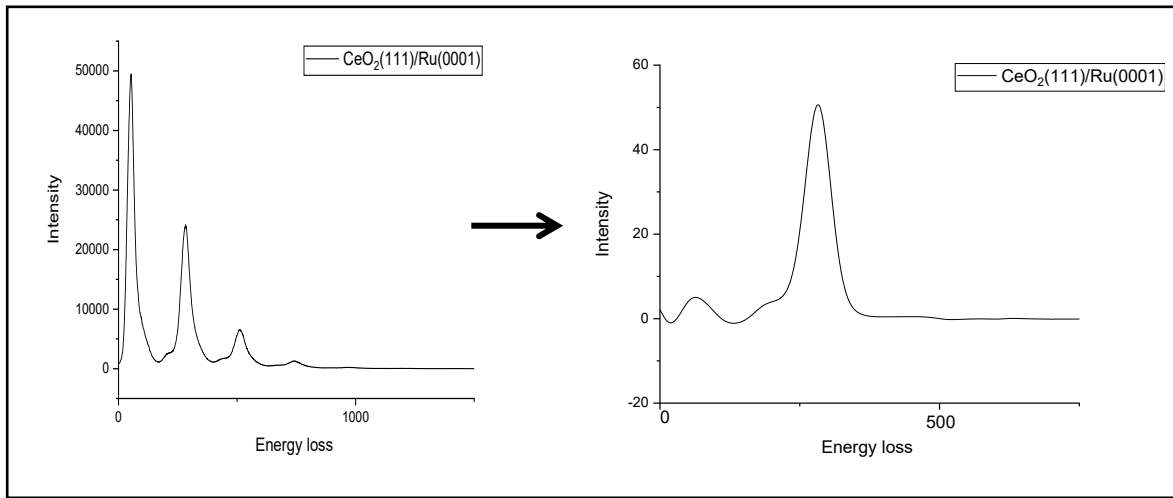The transformation leads to a smooth loss function as shown in figure 3.

Figure 3. HREELS spectrum of CeO₂ (111)/Ru (0001) before (left) and after (right) deconvolution.

Molecular vibrations

Each molecule has specific levels of rotational and vibrational energy. When energy from the incoming electrons is being absorbed, there is a visible transition in the mid-infrared region between these levels. For the small changes in atoms' positions, the potential energy *V(r)* can be calculated:

$$V(r) = \tfrac{1}{2}k\bigl(r - r_{eq}\bigr)^{2} \qquad\qquad (2.8)$$

where:

r is the distance between the vibrating atoms;

r_{eq} is the equilibrium distance between the atoms;

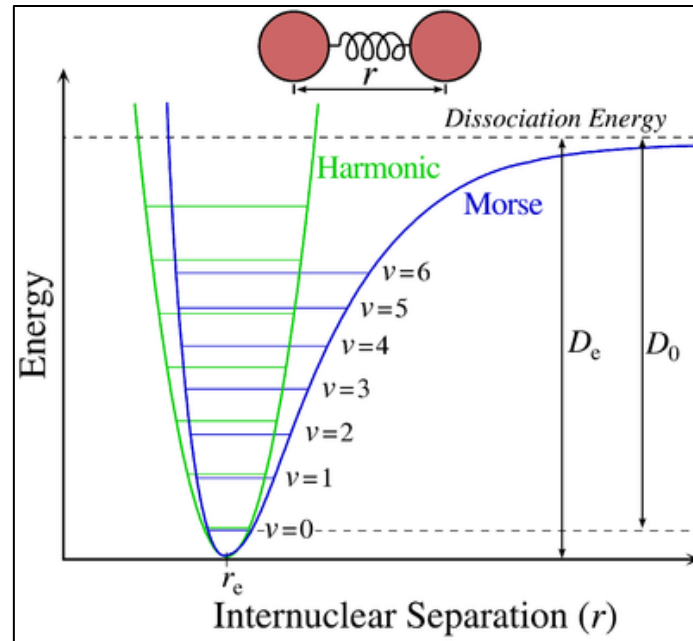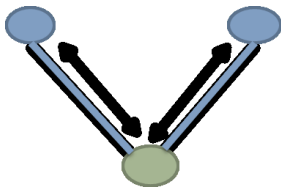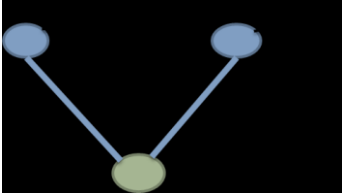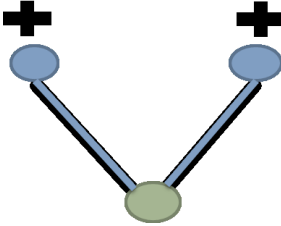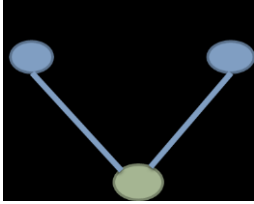k is the force constant of the vibrating mode.

Figure 4. Scheme of the Morse potential (blue) and harmonic oscillator potential (green). Adapted from [15].

Figure 4 presents the relation between the potential energy and the distance between the atoms, resulting in a harmonic or a Morse potential. In case of the harmonic potential, during the excitation by light absorption, transitions between vibrational levels v are only allowed if the vibrational quantum number changes by one unit ($\Delta n = 1$). The harmonic potential model is also only valid for the small-scale changes in the atoms' original position, as it assumes that the bond between the atoms cannot break. The Morse potential has a more physically realistic approach, presuming that the energy levels are not in an equal distance and overtones ($\Delta n > 1$) are allowed. [13]

While interpreting vibrational spectroscopy spectra, the important information is a number and type of vibrations in the molecule. The number of fundamental vibrations for a linear molecule is *3N-5* and for non-linear *3N – 6*, where *N* is the number of atoms in the molecule. [1] The difference between the numbers is based on the small number of rotational degrees of freedom for the linear molecular, as there is no energy required for the rotation along the main axis.

One can distinguish four main types of vibration:

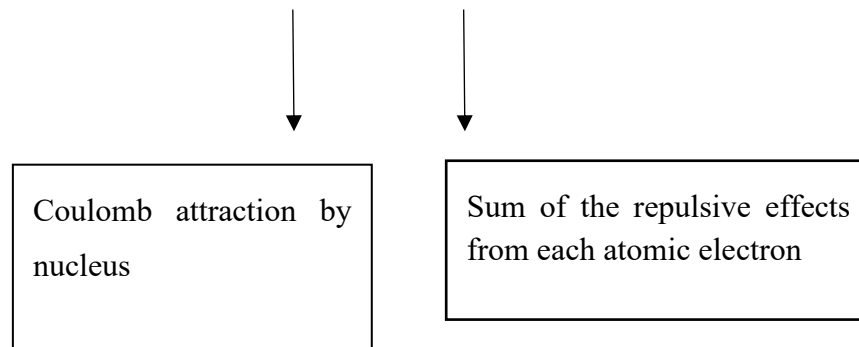|	
ν – stretch vibrations responsible for varying the length of the bond;	δ – one plane bending vibrations, not affecting the bond length, only the angles;
γ – out of plane bending vibrations, one atom vibrates out of the plane with respect to the central atom	τ – torsion vibrations, one atom moves in plane, other out of plane with respect to the central atom

Physics of electron scattering

Inner-shell scattering

To describe the inelastic scattering of electrons by a single atom in a solid, *Bethe theory* is a practical tool.

The interaction potential, which in this case is electrostatic energy between an incident electron and an atom, can be described as:

$$V(r) = \frac{Ze^2}{4\pi\varepsilon_0 r} - \frac{1}{4\pi\varepsilon_0}\sum_{j=1}^{Z}\frac{e^2}{|r-r_j|} \qquad (2.9)$$

| Coulomb attraction by nucleus | Sum of the repulsive effects from each atomic electron |

In the inner-shell scattering, an electron from the beam is interacting with a shell electron well below the *Fermi* level. To trigger the upward transition of the electron, it must absorb energy greater than its binding energy. After the inner-shell scattering, the targeted atom is in a highly excited, unstable state. In the process of relaxation, the outer-shell electron loses the energy in the form of electromagnetic radiation (x-rays) or it can convey the energy to another electron (*Auger* electron).

Outer-shell scattering

Compared to inner-shell scattering, describing outer-shell scattering is more complicated since the valence-electron wave functions are influenced by a chemical bonding, plus outer-shell scattering involves no single but many, delocalized electrons. To characterize the interaction of a scattered electron with an entire surface, one can use the dielectric response function $\varepsilon(q, \omega)$. Based on the function proposed by Ritchie [4] the expression for the electron scattering power on an infinite surface can be expressed as:

$$\varepsilon_0 \varepsilon(q, \omega) \nabla^2 \emptyset(r, t) = e\delta(r, t) \qquad (2.10)$$

Where the transmitted electron, characterized by coordinate r and moving with a velocity v is described as a point charge $e\delta(r, t)$, which generates within the surface a time-dependant electrostatic potential $\emptyset(r, t)$.

In semi-classical theory, the surface is described as a perfect reflector. The reflection probability equals the ratio of the intensity of the loss I_{loss} to intensity of the elastic peak I_{el}. Depending on the spatial restrictions, this ratio is related to the scattering probability (equation 2.2) in the following way:

$$\frac{I_{loss}}{I_{el}} \propto \frac{1}{cos\theta \sqrt{E_0 \omega^2}} \qquad \text{for surface phonons and plasmons;} \qquad (2.11)$$

$$\frac{I_{loss}}{I_{el}} \propto \frac{1}{cos\theta E_{0\omega}} \qquad \text{for adsorbate modes. [16]} \qquad (2.12)$$

Plasma oscillations (or plasmons) are collective excitations, which run as longitudinal charge density fluctuations through the volume of the solid (volume plasmon) or along its

surface (surface plasmon). Plasmon energy, $E_p = \hbar\omega_p$, where $\hbar$ is *Planck's* constant and

ω_p is the plasmon frequency in radians per second. For most of the solids E_p is in the

range 5-30 eV. [13] Because of the collective nature of the plasmon losses, the energy is

shared among many atoms. The electrons taking part in the oscillation share their energy,

which is only possible in the delocalized states. [13]

Spectrum

A typical spectrum in the range of 700 eV is shown in figure 5. The first characteristic

peak is a so-called zero-loss or an elastic peak. It is representing the intensity of the

electrons that do not lose any energy during the measurement. It includes electrons

scattered elastically and those contributing to the phonon modes excitation, for which the

energy loss is smaller than the experimental resolution. The region 4-40 eV corresponds

with the outer-shell electrons. The inner-shell excitation (core loss) is represented by

sharp, rising rapidly edge, decreasing gradually with the intensity loss. The beginning of

the steep edge of inner-shell peaks is dictated by the ionization threshold, which is the

binding energy of the corresponding atomic shell. Remembering that the position of core

binding energy depends on the atomic number of the scattering atom, one can deduct

from the spectrum analysed elements. In case of the thin samples, usually each feature at

the spectrum is related to the different excitation process. However, at thicker samples,

electrons may be scattered multiple times, which results in the higher number of peaks
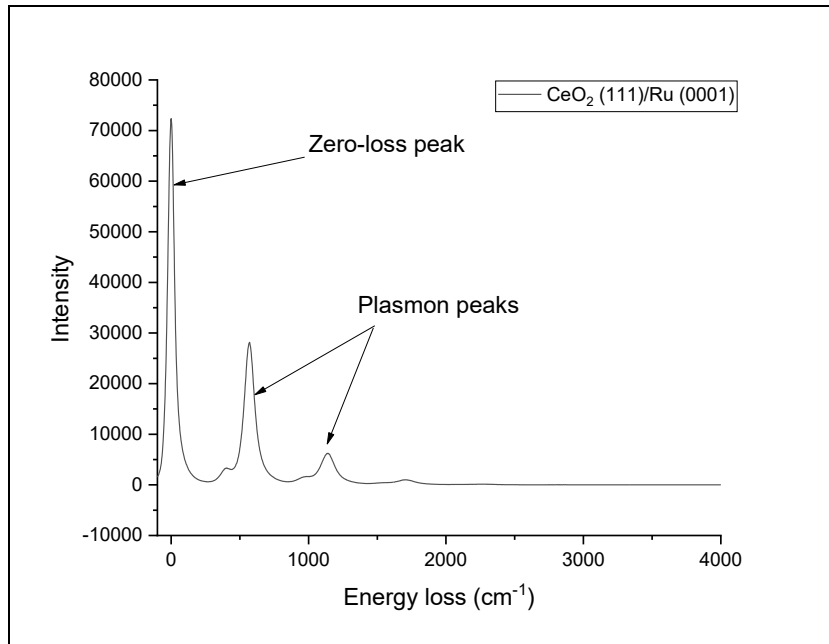
originating from the same scattering process.

Figure 5. HREELS example spectrum with characteristic regions of zero loss peak and plasmon peaks.

2.2. Low Energy Electron Diffraction (LEED)

LEED is a standard, surface science technique used to characterize periodic surface structures. The first LEED experiment was performed by Davisson and Germer in 1927 [18]; the theory behind the experiment was based on the fact that electrons have properties of waves. Since the 1960's the technique has been improved and nowadays it is not only a tool to take a picture of the diffraction pattern, but also to measure the influence of electron energy on the diffraction (IV-LEED) and the size of the crystal domains (SPA-LEED).
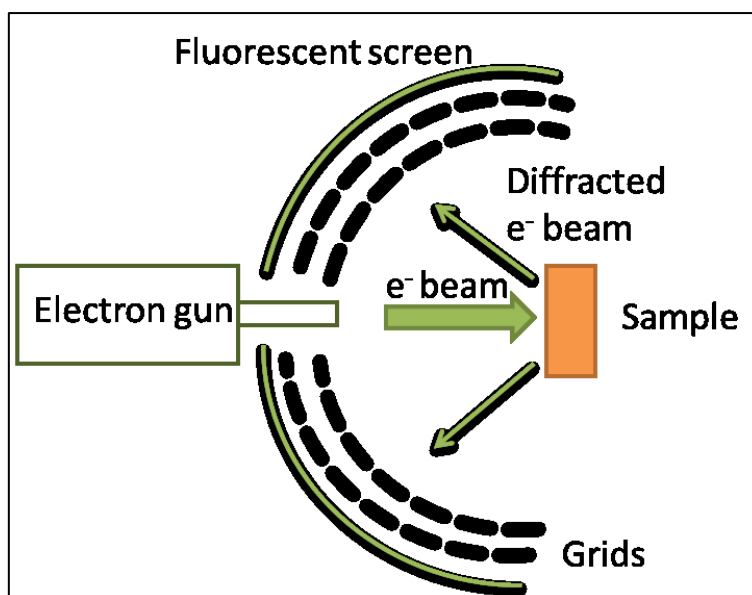
Figure 6. Schematic drawing of a Low Energy Electron Diffractometer (LEED).

During the LEED experiment [Fig. 6], an electron gun generates a monochromatic electron beam, in energy between 20-300 eV. The beam is focused on the grounded sample, where the electrons are elastically scattered, producing a diffraction pattern on a fluorescent screen. With the purpose to accelerate the electrons towards the screen, high voltage (~6000 eV) is applied. Retarding voltage is applied to grids to block inelastically scattered electrons. The LEED pattern is consisting of bright spots, reflecting the symmetry and crystalline order of the surface and it can be viewed either by using a digital camera connected to the computer or by eyes. The method is surface sensitive as the mean free path of the electron is short and the scattering occurs in a distance 5-10 Å of the surface. [1]

Assuming, that the electrons scattered from the crystal surfaces have the wave nature, the wavelength λ of the electrons with the momentum p can be calculated using *de Broglie* relation:

$$\lambda = \frac{h}{p} \qquad (2.13)$$

Followed by:

$$p = mv = \sqrt{2mE_K} = \sqrt{2meV} \qquad (2.14)$$

Where:

m- mass of electron [kg];

v- velocity [m/s];

E_K- kinetic energy [J];

e- electronic charge [C];

V- acceleration voltage [V].

The electron beam used in the LEED experiments has an electron energy in the range V=10-200 eV. As the result the wavelength is very small, in the range of interatomic distances in a crystal lattice (< 3Å). [4] The scheme of the electron scattering at the crystal surface is shown in figure 7.
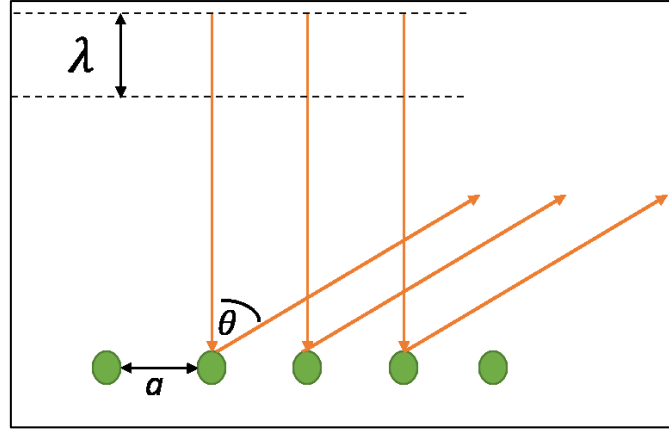
Figure 7 Scheme of the electron diffraction at the sample surface.

Elastically scattered electrons follow *Wulff–Bragg's* condition [21] stating that the path difference between the electrons coming from the different atoms is equal to a multiple of the wavelength:

$$2dsin\theta = a\lambda \qquad\qquad (2.15)$$

assuming that d is the interplanar distance in the crystal lattice, θ is the angle between the beam and the sample plane, a is an integer and λ is the wavelength. Each crystal has different interatomic and interplanar distances. The set of the distances creates a fingerprint, a diffraction pattern, supporting sample characterization. The obtained diffraction pattern is a direct image of the reciprocal lattice of the surface. The picture of an atomically well-ordered surface presents bright and sharp spots on the low background intensity. The quality of the image decreases with the appearance of impurities and structural defects on the surface.

2.3. Temperature Programmed Desorption (TPD)

Another useful tool to understand the interactions between reactants and a surface is Temperature Programmed Desorption (TPD) also called Thermal Desorption Spectroscopy (TDS). It is a technique where desorption of atoms and molecules from the surface is analysed by the mass spectrometer, during heating with the constant rate $\beta=dT/dt$. [4] The TPD method gives a straightforward result in case of homogenous and flat surfaces. Moreover, it is simple and inexpensive. With the sufficiently high heating rate constant, the desorption reaches its maximum and the coverage plunges as the surface is free of molecules. The peak area should be proportional to the amount of the desorbed species. By analysing the desorption properties of a gas, acting as a probe molecule, it is possible to determine certain aspects of the morphology of the sample. The total number of molecules desorbing in the certain amount of time (desorption rate r) is described by the *Polanyi-Wigner* equation [1]:

$$r = -\frac{d\theta}{dt} = v\theta^n e^{-E_d/RT} \qquad\qquad (2.16)$$

Where R is the gas constant, T is the temperature, t is the time and v is the pre-exponential *Arrhenius* factor. As in the case of adsorption, a molecule can directly desorb from the surface (first-order process), or two neighbouring atoms can form a molecule and desorb together (second-order). In the special case of zero-order desorption process (n = 0), for multilayers of adsorbates, desorption rate does not depend on the initial coverage. In the first-order process, the desorption rate is proportional to the initial surface concentration θ (n=1). The popular tool for the first order desorption analysis is the *Redhead* method, where the activation energy of desorption E_{des} is given:

$$E_{des} = RT_{max}[\ln\left(\frac{\nu T_{max}}{\beta}\right) - 3.46]$$ (2.17)

R - gas constant;

T_{max} – peak maximum temperature;

ν – pre-exponential factor;

β – heating rate dT/ dt.

In general, a first-order desorption peak in a TPD spectrum will reach its maximum at the same temperature regardless of the initial coverage. Nonetheless, that adsorption of the atoms on different sites of the surface, as well as multiple binding states, can create more complex spectra with multiple peaks.
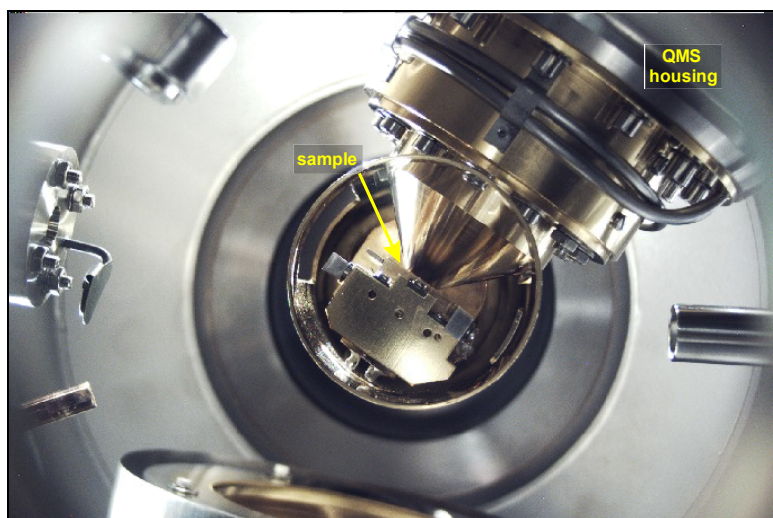

Figure 8. Picture taken from the bottom of the chamber in the FEL setup shows the position of the QMS facing the sample.

In a case of the described setups a thermocouple spot-welded to the crystal allows temperature reading. Desorption rate is measured by the quadrupole mass spectrometer placed in front of the sample [Fig. 8]. QMS mechanism is based on atoms ionized by

electrons emitted from the cathode in the ionizer. Ions are then separated by mass-to-charge (m/e) ratio and transported to the detector. The result is a spectrum of intensity vs. mass-to-charge ratio. Pumping speed is a crucial parameter during TPD experiments, and it should be efficient enough to prevent re-adsorption of the desorbed species on the surface. [22]

Adsorption

In a process of adsorption, a bond is formed between a surface and an atom or a molecule from a liquid or a gaseous phase. The strength of the bond depends particularly on the position of the adsorbate on the surface (terrace, step edge, defect, etc.). In the adsorption process sufficient amount of energy must be delivered to the reactants in order to break the bond. This energy is called the bonding energy or bonding enthalpy. The higher the energy, the stronger the bond is. [23] The energy required to start the reaction and create the bond is called the activation energy. Adsorption can occur molecularly (first-order process) or it can be followed by dissociation of the molecule (second-order). Molecular adsorption on surfaces can be characterized by the *Langmuir* model, which restricts the molecules to adsorb on empty sites on the surface as an ideal gas at isothermal conditions. [1] Under these conditions the process of adsorbate binding is treated as a chemical reaction between the adsorbate molecule and an empty site on the surface, creating an adsorbate complex. The occupancy of the adsorption sites θ, is described as a number of occupied adsorption sites N_{occ} divided by the number of existing sites N:

$$\theta = \frac{N_{occ}}{N} \tag{2.18}$$

Depending on the type of binding process and a binding strength, one can distinguish between chemisorption and physisorption. In physisorption the interaction between an

atom and a surface is on the ground of the weak *van der Waals* forces. The forces originate from dipole moment changes. The change is triggered by the interaction between the electron clouds of adsorbate and a substrate. Low temperature is required for adsorption and the usual bond energy is in the range 50-500 meV/atom. [21] An example of physisorption is adsorption of rare gas atoms like Ar on metal surfaces at temperatures <30K. [24] Chemisorption is based on a strong interaction between adsorbate and substrate. As a result, it may lead to irreversible changes of the molecular properties. In the majority of cases, an adsorption energy per atom is higher than 0.3 eV, typically $\geq$ 1 eV/atom. [22] Chemisorbates form only a single layer on the substrate surface. However, specific binding sites may be favoured over other depending on the surface potential. [22] Examples of chemisorbates are O_2 and H_2 molecules dissociating on transition metal surfaces (such as Rh, Pd and Ru surfaces) at room temperature (300 K), creating a saturation layer of atomic O or H, respectively [22] [23].
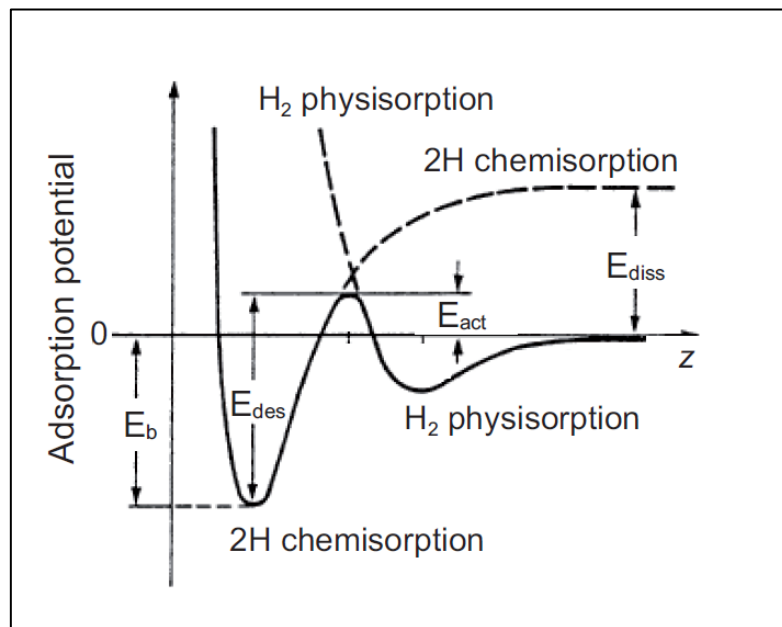

Figure 9. Illustration of the adsorption of H_2 on the metal surface. Here, E_{diss} it the dissociation energy of H_2 in the gas phase, E_{act} the activation energy for adsorption, E_b the binding energy in the chemisorption, and E_{des} the activation energy for re-combinative desorption ($H + H \rightarrow H_2$). Adapted from [22]

As shown in figure 9, at first, when reaching the surface, H_2 follows the physisorption potential curve. Nevertheless, if it has enough energy to overcome the activation barrier, hydrogen may follow the chemisorption potential curve, which leads to dissociation into two atoms, adsorbing on the metal surface.

2.4. Scanning Tunnelling Microscopy (STM)

Invented in 1983 by Bining and Rohrer, scanning tunnelling microscopy is a method used for imagining the local surface topography. [22] The resolution of the obtained data depends on the quality of the tip and the interaction between the tip and the surface, with possibility of receiving atomic resolution.
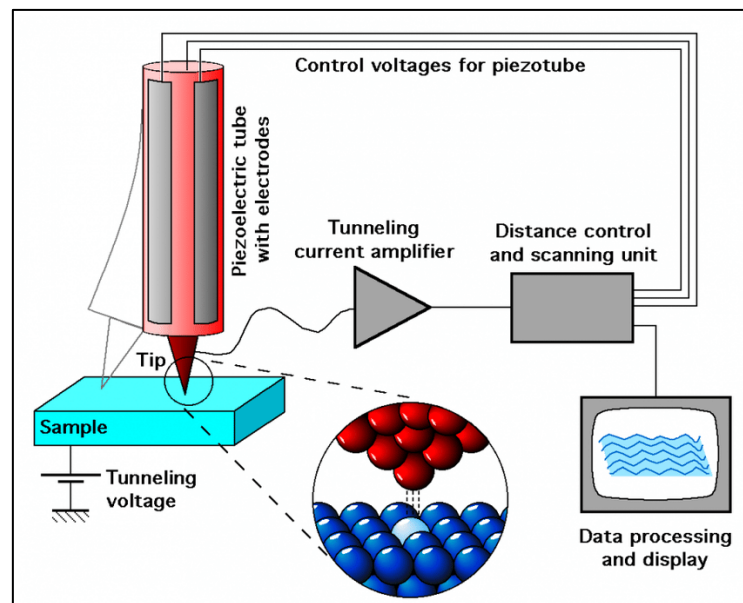

Figure 10. The STM setup, adapted from [25]

The general idea behind this method is based on a movement of a sharp tip across the surface, induced by piezoelectric translators (Fig. 10). The tip is placed on a piezo-electric scanner in few Angstroms from the surface. At the same time changes in tunnelling current are being monitored. The STM experiment can be conducted in one of the following ways:

a) in *constant current mode* when the constant tunnelling current is held, but the z value (height) changes according to topography of the sample surface;

b) in *constant height mode* when changes in the tunnelling current with constant z value are measured.

The mechanism of the STM is based on the fact that electrons at the surface form some sort of a cloud of electrons. When the sharp tip approaches the sample surface (<10Å), the clouds of electrons coming from the sample and the tip start to overlap. By applying a positive or negative potential to the tip, electrons can tunnel between the tip and the sample. Depending on the size of the gap, tunnelling current varies from pico- to nanoampers and is calculated as follows: [4]

$$ j = \propto_1 \frac{\sqrt{\varphi_{av}}}{s} V e^{-\alpha_2 \sqrt{\varphi_{av} s}} \qquad (2.19) $$

where:

s is the distance between the tip and the surface;

V is the potential between tip and the surface;

φ_{av} is the average between the work functions of tip and the sample;

$\propto_{1,2}$ are constants.

As shown on the diagram [Figure 11] after applying voltage V the electron in the sample rearranges upwards or downwards with respect to the tip's electrons. [23] Only when the tunnelling gap is small enough, valence electrons near the Fermi level tunnel to unoccupied states of the tip. However, the STM method may not work for some of the semiconductors as the difference between the Fermi levels of sample and tip is too narrow. Another requirement for successful measurement is sample conductivity, for example insulators with no conductivity cannot be measured.
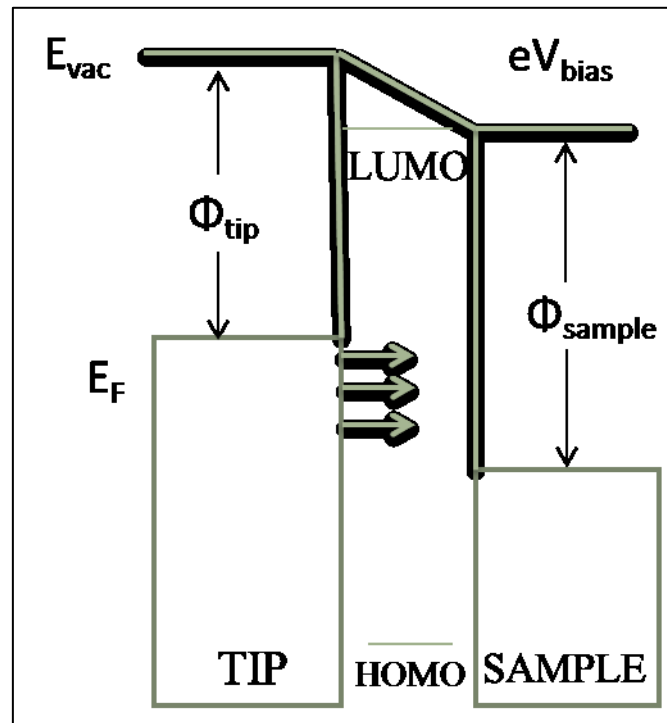

Figure 11. Energy scheme of tip-sample energetics, when a positive voltage is applied to the surface.

One must keep in mind that STM presents the density of states near the Fermi level, not actual images of atoms. Nevertheless, the method is widely used in surface science.

2.5. Vibrational Action Spectroscopy

The idea of the vibrational action spectroscopy is to use "action" resulting from the excitation of a vibration in the aggregates as an indicator for the excitation. [12] An example of such action is desorption of rare gas atoms (Ar, Kr or Xe) from the metal oxide clusters, as a result of the increase of temperature, due to the absorption of the energy from the infrared beam. [12] Even single absorbed photon can induce this behaviour. [24] By monitoring the desorption yield as a function of wavelength, the absorption spectrum can be obtained. Analysis of the vibrational modes helps to determinate the molecular structure of the sample. Vibrational spectra are the fingerprints of the electronic and structural properties of matter.

So far vibrational action spectroscopy has been mostly employed in characterization of the small aggregates in the gas phase. [11] [26] IR FEL has been used for example to characterise the bonding of CO to transition metal clusters [11], to investigate structural properties of water clusters such as $H_3O^+(H_2O)_{20}$ [27] as well as in combination with ion mobility spectroscopy in order to investigate bio-molecules in the gas phase [28]. During the vibrational action spectroscopy experiment, clusters are decorated at low temperatures with gas messenger atoms, which weakly interact with clusters, without changing their properties. Next, due to the IR radiation, aggregates absorb photons energy, which excites a vibration in the cluster and may trigger rare gas desorption. Rate of this process as a function of the photon energy is the output of the experiment. Depending on the size of the clusters, different amount of the infrared radiation is required to cause the action. As much as in clusters with weak atomic bond the energy required for this purpose is in the range of only a few photons, transition metal and semiconductor clusters are more demanding. [29] Decorating the clusters with rare gas atoms can increase the sensitivity

of the method. As a result, lower energy is required to induce desorption, in some cases even a few photons. Rare gas atoms are the most suitable for the messenger function also because the lighter they are, the weaker they bond to the cluster, causing minor changes in its properties. [30]

A similar technique can be also used in case of crystals and thin films, where all non-reflected intensity of the infrared beam may be absorbed at resonance energies, causing the warmup of the sample and desorption. In this case, comparing to gas clusters, interaction of the film with the substrate is another parameter that one must pay attention to, since it may influence the rare gas desorption for example if the substrate has low heat conductivity. Low enough temperature of the sample is required during the experiment as the adsorbate desorption should be influenced only by the laser illumination. Regarding FHI free electron laser, the increase of the temperature is in the range of few Kelvins as the time-averaged laser power is around 1 W. [12] Part of the infrared power can be absorbed by bulk vibrations, appearing in the rise of the temperature. At the same time, absorption of the infrared beam power by monolayer or sub-monolayer of adsorbate, as well as surface vibration is rather limited. There are two main cases leading to the rare gas desorption:

I.   **Indirect channel** - high energy uptake and temperature rise cause significant rise of the temperature and consequently gas desorption. Also called thermal channel, is common for vibrations with a high absorption cross section like bulk polariton, where much of the energy is absorbed.

II.   **Direct coupling (vibrational) channel** –small energy uptake and hence small rise of the temperature. Temperature increase is not a cause of desorption.

Excitation of surface vibration can lead to desorption if enough energy is transferred to the bond between the rare gas atoms and the surface.

Photon absorption by a substrate or adsorbates on it can induce breaking the bond in the adsorbed molecule or between adsorbate and substrate. During that process, the electrons building the bond rearrange themselves to occupy the excited state wave function, which can lead to desorption or reaction. The excitation process can be conducted in three different ways:

1. **An adsorbate localized** process or else **direct excitation**, when a photon is directly absorbed by an adsorbate molecule. This leads to an excitation of the molecule from a ground state to an excited state. [31]

2. **A substrate mediated process** also called an **indirect excitation**, where an adsorption of a photon by the surface drives an electronic transfer to the bond between the adsorbate and the surface. If the photon wavelength is in the IR region and smaller, adsorption is accompanied with the creation of a charge in the substrate, which can induce adsorbate reactions, if the vibrations are excited. [31] The substrate mediated process has been reported for the metals and the semiconductors, supported by a theoretical model of the process reported by Gadzuk et al. [32]. According to him the process is a hot electron mechanism, which is divided into three stages. At first electrons are being excited in the bulk, and then transported to the surface, where they are conveyed to the unoccupied orbital of the adsorbate.

3. **Laser induced surface phonon excitation**- when reactions at the surface are induced by surface heating due to absorption of the phonons. The energy gained by the vibrations during the short laser radiation is usually much higher than the energy they can transfer to the lattice. [33]

The FEL at FHI is a perfect radiation source for the surface action spectroscopy, due to its high beam intensity and wide range of available photon energies for a given set of FEL parameters.

The method allows analysis of different scientific topics:

- vibrations of deposited clusters;

- surface vibrations;

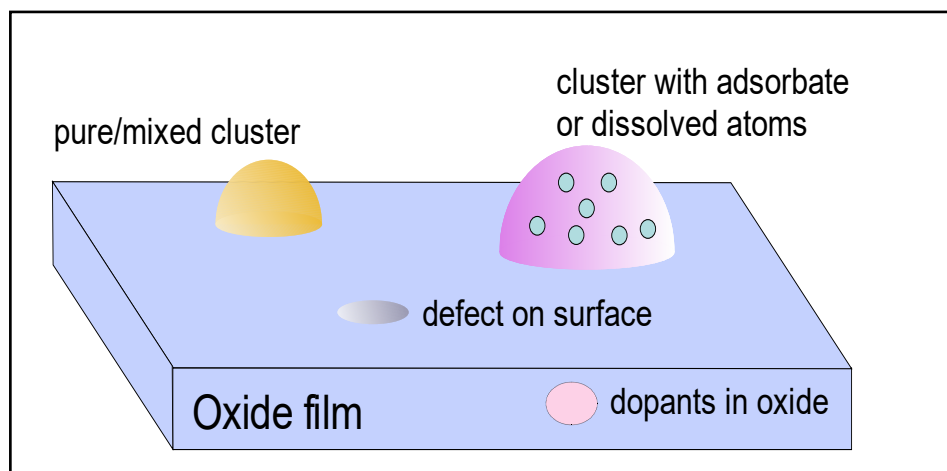- oxide layer impurities, dopants and defects;

- adsorbate vibrations.

Figure 12. Scheme of impurities, dopants and clusters on the oxide surface

3. Experimental Setup.

This chapter aims to provide information on the experimental setups used in the present study. All the experiments were conducted in Fritz-Haber-Institute, in three different ultra-high vacuum (UHV) systems. The morphology of the sample was investigated in the STM chamber while the vibrational and electronic structure in the HREELS and FEL systems. In all the systems, only pressures in the low 10^{-10} mbar range were employed, in order to provide well-defined conditions for the sample preparation and analysis.

3.1. The HREELS system

The HREELS system consists of the two stainless steel chambers and a high-pressure cell, which can be separated by a gate valve. The upper chamber is the preparation chamber, where samples can be prepared. It is equipped with a commercial electron-beam evaporator (single evaporator from *Focus*), a quartz-crystal microbalance, an ion gun for sputtering, a low-energy electron diffraction (LEED) apparatus, which is used for identifying the degree of surface crystallinity and measuring the periodicity of ordered surface structures, AES optics (from *Omicron*) and a quadrupole mass spectrometer (QMS). The QMS analyser is located in differentially pumped stainless-steel housing with a 2 mm diameter nozzle directed towards the centre of the chamber. During TPD measurements the crystal was positioned at about 0.5 mm in front of the nozzle.
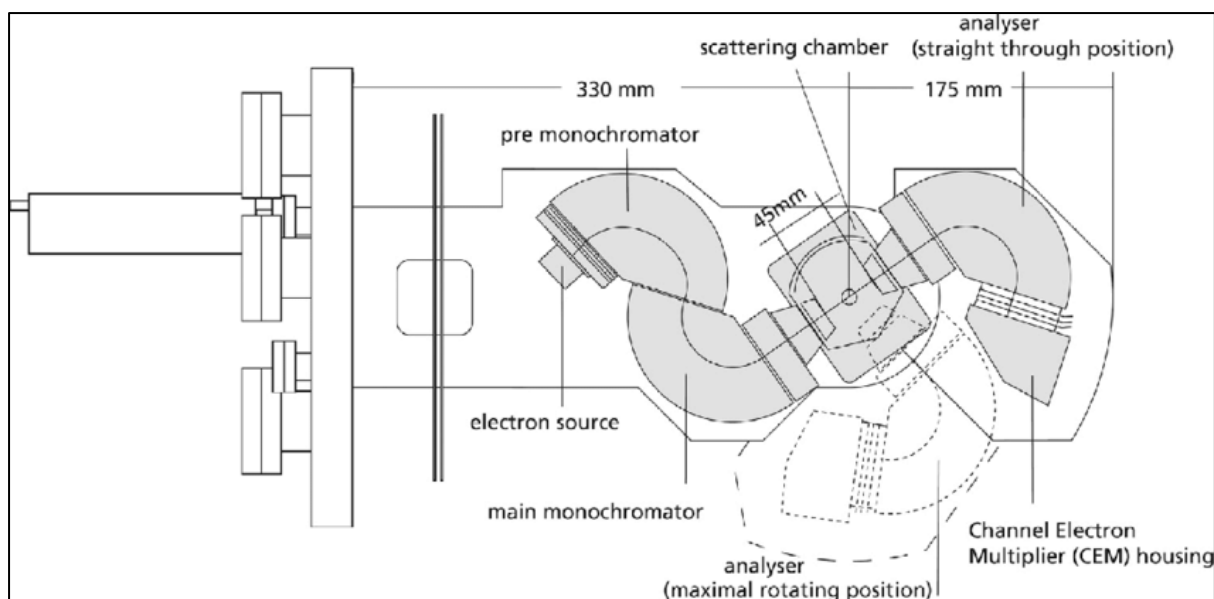
Figure 13 HREELS spectrometer Delta 0.5, designed by Ibach [18]

HREELS spectra were recorded in the lower chamber, which was equipped with a VSI Delta 0.5 spectrometer [Fig.13]. The electrons are emitted from an electron source and then conveyed through the pre and main monochromator. Due to the special construction of monochromators, it is possible to obtain both good energy resolution and a high electron flux. After leaving the last monochromator, a focused electron beam is reflected by the sample and analysed. The intensity of the detected electrons as a function of their energy loss is recorded by the spectrometer.

All spectra presented in this thesis were recorded in specular geometry (angle$_{in}$ = angle$_{out}$ = 35° with respect to the surface normal). The incident beam energy was 6 eV for HREELS spectra with the resolution of about 30 cm^{-1}. In the case of electronic spectra, the energy was 25 eV, with the resolution of 250 cm^{-1}. A high-pressure cell was used for sample treatment at high pressures.

High-pressure cell

A high-pressure cell was constructed especially for this study. A small UHV chamber was connected directly to the preparation chamber by a gate valve through which sample can be transferred in vacuum pressure. The important part of the high-pressure cell is a movable heating stage, which consists of the socket, to insert the sample holder, a 150 W halogen lamp and thermocouple connectors for temperature measurement. The halogen lamp (*Osram*) is in a fixed distance below the backside of the sample. The focal distance is 2 cm and the power max. 150 kW. During the experiment, hydrogen (99,999% purity, *Linde Gas*) is dosed, until the 10 mbar pressure is reached. To decrease the possible surface contamination, hydrogen first flows through liquid nitrogen cold trap, next over the sample and then it is evacuated from the cell by a roughing pump. The pumping speed and the gas flow are adjusted to keep the pressure constant at 10 mbar. In order to limit adsorption of contamination, the inner walls of the high-pressure cell are coated with gold. During annealing, the cell is cooled by water flowing through the copper tubes, welded on the outer walls of the cell.

3.2. The Free Electron Laser system

In the Fritz-Haber-Institute a new system was constructed to characterize oxide surfaces via action spectroscopy using FEL Infrared Radiation.

Figure 15 shows the FHI FEL setup. Electrons emitted from the electron beam, are being accelerated to energy up to 50 MeV by two LINACs (accelerators). Next, the electron beam reaches the resonator, which consists of two high-reflectivity mirrors at each end of

the undulator. An undulator is a device, which consists of dipole magnets creating a magnetic field which is perpendicular to the direction of the electron beam [Fig.14]. Periodical changes in the magnetic field polarity bend the electron beam causing a `wiggling' motion of the electrons. This motion results in radiation of light with a wavelength depending on the electron energy and the undulator parameters. [12]
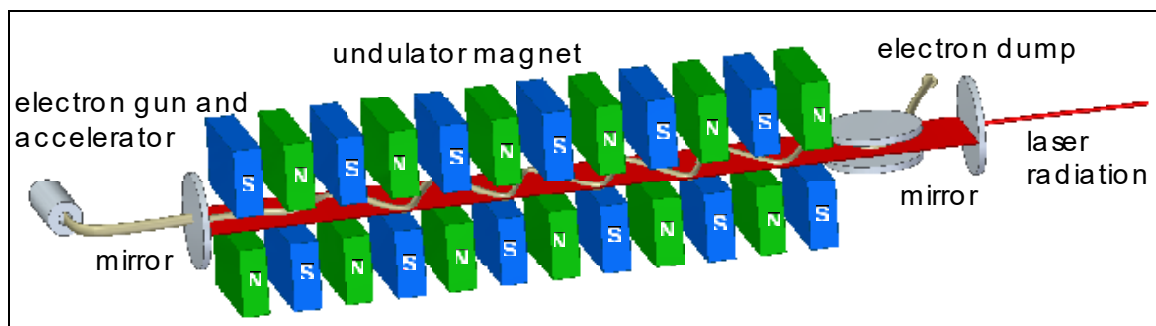

Figure 14. Illustration of the undulator, adapted from [15]

The emitted light is amplified in the resonator by the interaction with successive electron bunches. In the end, the light is reflected in the mirrors and sends to the specific user through the hole in the resonator. The FEL laser radiation can be tuned from 4 to 50 um- mid-infrared wavelength range. [12] Such radiation can be used as in the example of FHI FEL in vibrational spectroscopy of clusters and molecules in the gas phase, molecular spectroscopy of ions embedded in superfluid helium nano-droplets and second-harmonic generation in the *Reststrahlen* bands of solids.
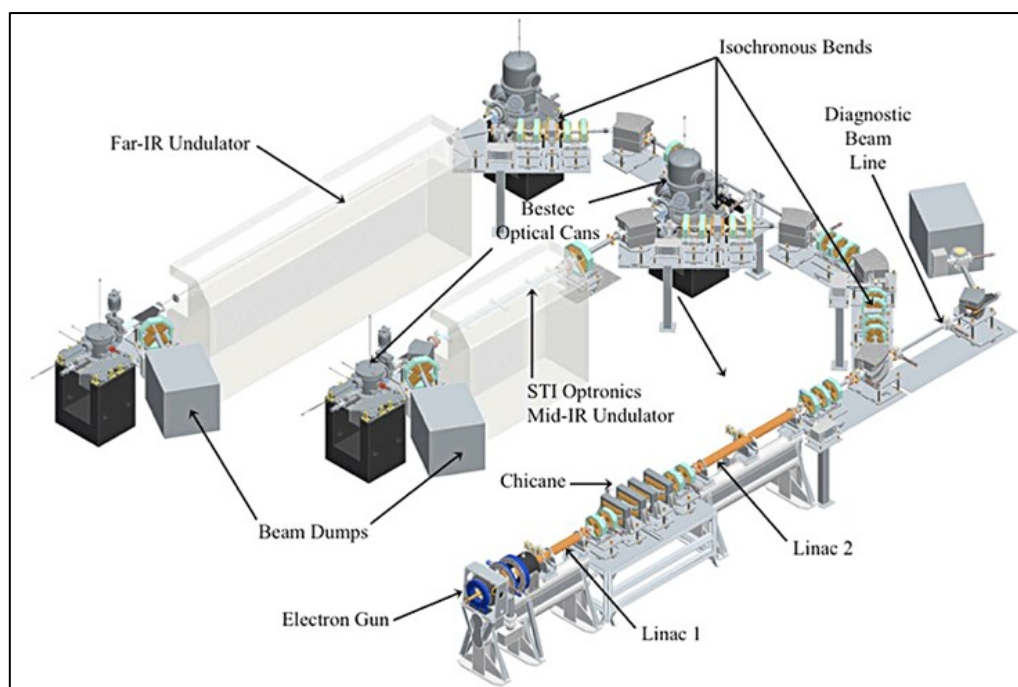
Figure 15. A layout of the FHI FEL. Adapted from [12]

The Fritz Haber FEL generates macropulses (5–8 μs long pulse trains at 10 Hz repetition rate) consisting of some thousand micropulses at a rate of 1 GHz, each of them a few psec long. [23] The energy per micropulse is close to 10 μJ corresponding to ~50–80 mJ per macropulse. The spectral width of the radiation is about 0.5% (full width at half maximum) of its central wavelength. [12]

The FEL setup used to perform the described experiments, constructed in 2016, consists of two stainless steel chambers: preparation chamber and STM chamber, nevertheless during described experiments only the first one has been used. The most important components of the preparation chamber are highly sensitive quadrupole mass spectrometer (QMS) from *Extrel* (Extrel MAX 500 HT) and a helium cryostat for cooling the sample (Janis). As shown in the drawing [Fig. 16], the laser beam is reflected by the set of mirrors into the chamber through a cesium iodide window, where it illuminates the sample surface at an angle of 70-83 with respect to the surface normal. Such a grazing

angle allows lowering the distance between the sample and the QMS. The beam illuminates roughly 3 mm diameter area of the sample. The beam power is measured by a type K thermocouple coated with an infrared absorbing layer, located between the cesium iodide window and the sample. Vibrational action spectra described in this thesis are recorded by the messenger atom method [24], employing adsorbed argon or neon. After the modifications of the manipulator and QMS, which resulted in achieving a lower temperature during the experiments, also molecular hydrogen was used as a messenger gas.
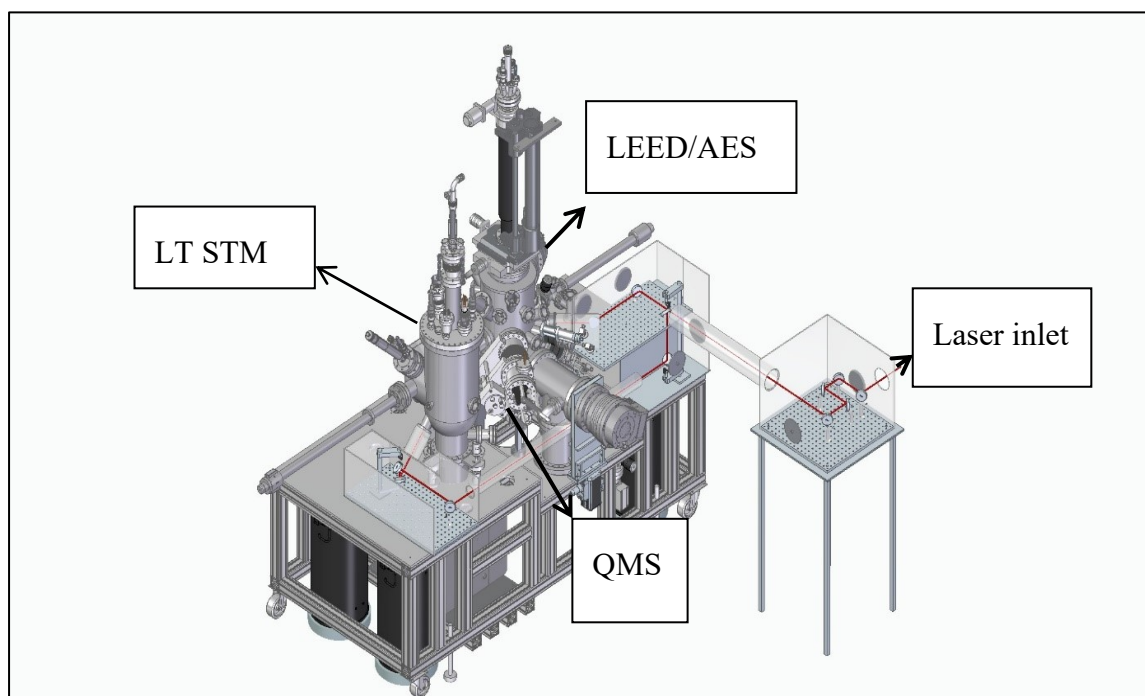
Figure 16 Design of action spectroscopy experimental setup. Adapted from [24]

The QMS, mounted in a pumped housing, has a small opening (4 mm diameter) for detection of desorbed rare gas atoms. During the experiments, the sample is positioned at a distance of a few millimetres from the opening. The sample is heated by tungsten wires with the heating rate of 0.1 to 25K/s. The temperature measurement is performed using a K-type (*Chromel-Alumel*) thermocouple spot-welded to the sample, which is sufficient at

the high temperatures, but inaccurate at the very low temperatures required for the action spectroscopy experiments. Consequently, it is possible only to estimate the temperature during the experiment by comparison to well-known desorption temperatures of previously used rare gases. We can certainly say that at first, the temperature was too high for the neon multilayer formation (less than ~ 6K), yet too low for neon monolayer desorption [above ~10K for Ru (0001)]. Neon, the most often used rare gas, was dosed by filling the QMS housing, while the sample was positioned in front of the opening. The gas flow was controlled through computerized piezo dosing valve.

With the time, a couple of modifications to the original system were made, in order to reduce the infrared radiation power originating from the surrounding (chamber walls, QMS housing, etc.). Firstly, liquid nitrogen cooling of the QMS housing, which also reduces the chamber pressure and the pressure in the QMS housing and at the same time the contaminations from residual gases. Secondly, the direct view of the sample to the filament of the mass spectrometer was blocked with two cold metal sheets [Fig. 17].
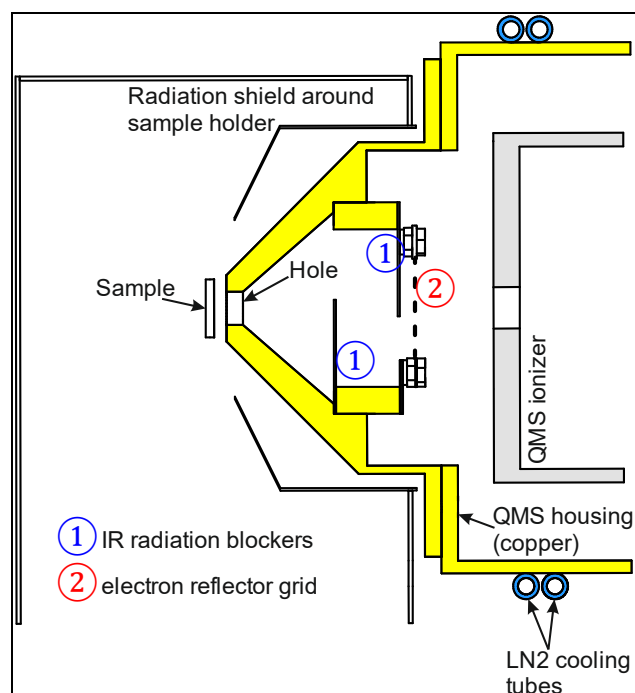
Figure 17 Modifications in the QMS improving cooling. Adapted from [24]

The experiment described in this thesis was conducted following the procedure illustrated in Fig 18. First, the sample is decorated with the rare gas atoms. Next, the sample surface is irradiated with IR light, which causes desorption of the gas. Meanwhile, the gas is directly detected with a QMS as a function of the IR energy. In the future, it will be possible to perform STM measurement during the FEL irradiation.
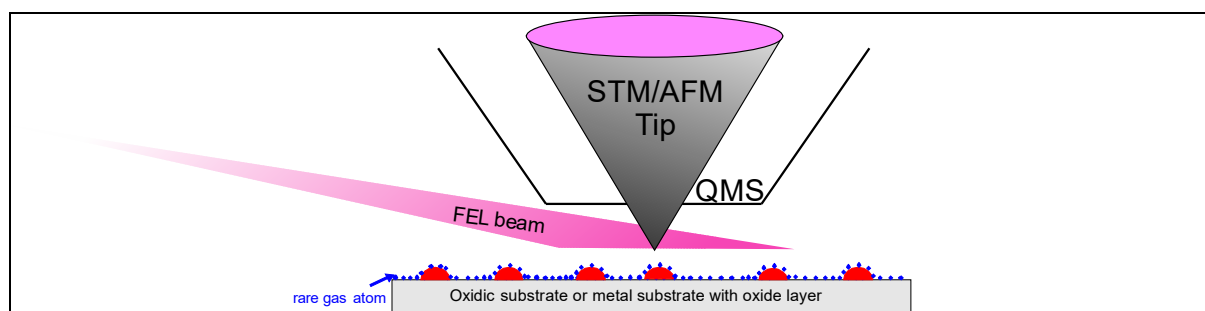
Figure 18. Scheme of action spectroscopy procedure.

3.3. The STM system

The STM experiments were performed in the UHV system consisting of the sample preparation setup, the STM chamber and the high-pressure cell moved from the previous HREELS setup. Transport of the sample between the chambers was possible due to the system of cross-mounted manipulators. The usual operating pressure of around 1×10^{-10} mbar was kept by two turbo-molecular pumps supported by an ion pump (*Varian*) and titanium sublimation pump (*TSP, Varian*). The main chamber was equipped with all necessary instruments required to obtain the comparable quality of the sample as in the previously mentioned systems, such as sputter gun, evaporators, LEED, AES, QMS and temperature control system. To avoid the contamination, the sample stage was made of the ceramics, which were placed on a copper block. During the heating procedure, the sample holder was cooled with air through the metal coil. If required, as like during the thin film preparation, the air was additionally cooled with liquid nitrogen, allowing reaching a sample temperature of less than 200K. During the STM measurements, the mechanical noise was partially canceled by the electronic vibration isolation system (*Herzan*)

3.4. The sample setup

The sample was mounted on a specially designed sample plate, as schematically described in figure 19, to allow the transfer between the manipulator in the preparation chamber and a heating stage in the high-pressure cell as well as to the STM stage.
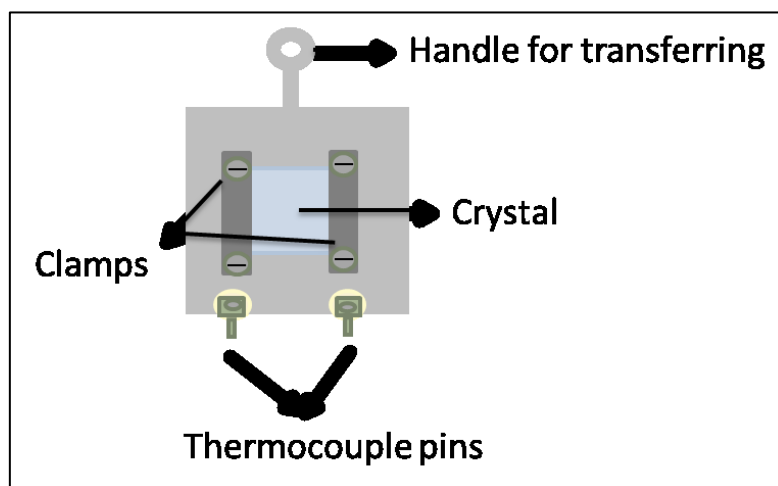

Figure 19. Scheme of the sample plate.

The plate allows sample heating and temperature measurement in chambers. The clamps are inserted in the slits on the sides of the sample to fix it against the base plate of the holder. A *chromel/alumel* thermocouple is welded to one of the clamps and to properly isolated pins on the sample plate. The pins are then inserted in corresponding thermocouple sockets in the manipulator or high-pressure cell sample stage. The base plate of the holder has a hole behind the sample for heating. In the preparation chamber, the sample could be heated radiatively from the backside with a tungsten filament. An additional electron beam heating, for temperatures higher than 400°C, was applied by setting the sample to a positive high voltage (the W filament is electrically isolated from the rest of the manipulator and remains at ground potential). In the high-pressure cell, as mentioned before, the sample was heated from the backside with a halogen lamp. Most of

the sample holder parts (the base plate, the clamps and the screws) are made of platinum. This is to avoid extensive adsorption or any gas phase transport of hydrogen from the holder to the sample surface during the high pressure (10 mbar) hydrogenation.

4. Surface Action Spectroscopy-the first results.

In this section, the results obtained through the vibrational action spectroscopy are presented. After constructing the first setup equipped with free electron laser to analyse solid surfaces, model systems were required. The ideal model system sample should be previously well described in the literature, to easily identify vibrations. Plus, there should be a difference between bulk and surface vibrations, which helps to determine surface sensitivity of the method. Here, two systems are described: $V_2O_3(0001)/Au(111)$ as an example of the direct vibrational coupling and a single crystal TiO_2 (110), where the rare gas desorption was induced by the rise of the temperature.

4.1. Direct vibrational coupling

Vanadium oxide was prepared using the recipe reported before. [34] The first step in the film preparation was the evaporation by direct electron beam heating of a 2 mm thick vanadium wire (mounted in a *Focus EFM3* electron beam evaporator) in an oxygen atmosphere (1 × 10^{-7} mbar) at 600 K. The deposition rate of the evaporator was beforehand calibrated with a quartz microbalance, usually between 0.5 and 1 Å/min. The next step of the film preparation was annealing at 670 K in 1 × 10^{-7} mbar of oxygen followed by annealing in vacuum at 850 K. Those two steps were repeated in cycles until the 10 nm thickness was obtained. Figure 20 (left) shows characteristic Au(111) (1x1) LEED image, where every integral spot is surrounded with some visible streaky lines, indicating the herringbone structure. The second image presents the vanadium oxide (√3x√3) R30° superstructure.
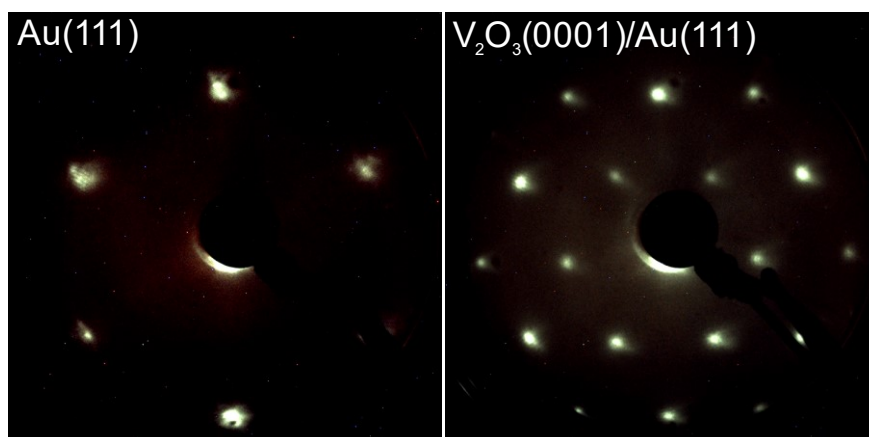
Figure 20. LEED images of Au (111) on the left side and V_2O_3 (0001)/Au(111) on the right side obtained at 70 eV.

Vanadium oxide (V_2O_3) is a perfect model material to characterise surface sensitivity of the method, as its film is terminated by characteristic vanadyl groups [Fig. 21]. This V=O double bond has been determined to only exist in the top layer of the film by HREELS and IRAS. [35] [36]
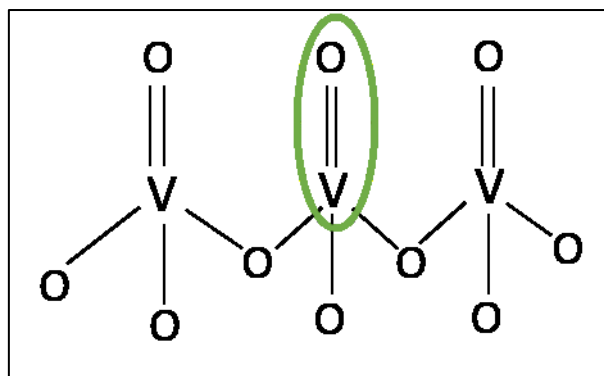

Figure 21. Schematic structure of V_2O_3 with characteristic V=O bond circled in green.

Vanadyl groups have specific vibrational energy around 1000 cm^{-1}. [37] Gold crystal was chosen as the substrate due to the highest mid-infrared reflectivity among all metals, which results in the small risk of the sample warming up as the thermal conductivity is high, plus the IR absorption of the V_2O_3 will be high as IR intensity at the surface is increased [38]. The radiation intensity was adjusted in a way that it does not destroy the surface, yet it is sufficient to cause desorption.
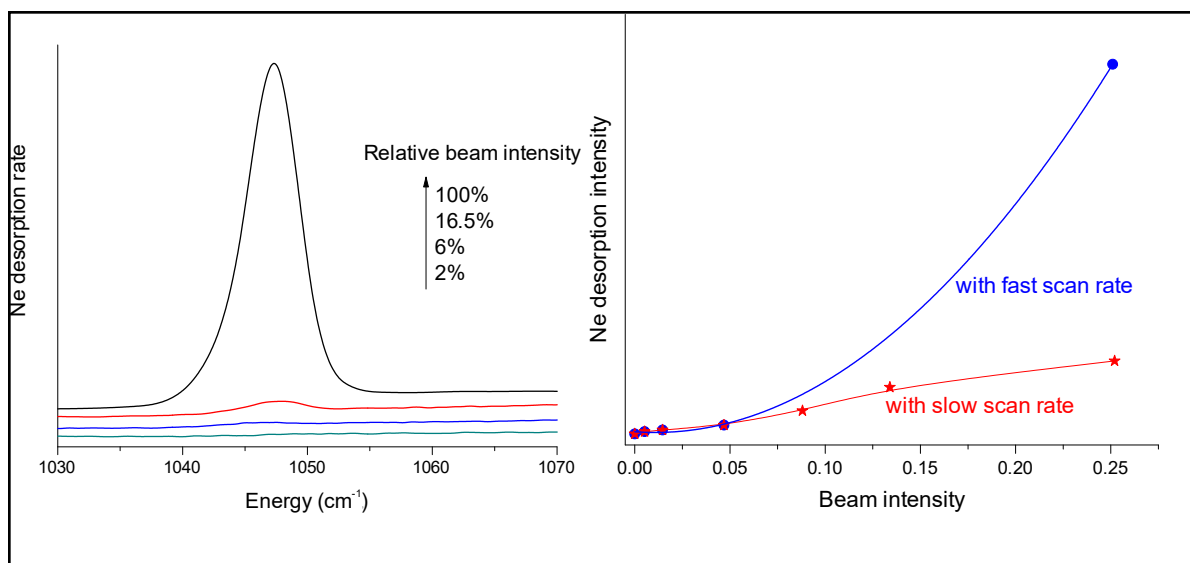
Figure 22 Relationship between beam intensity (on the left), scanning speed (on the right) and desorption rate.

From figure 22 it can be concluded that the best desorption parameters can be obtained when the beam is at above 16.5% intensity when the scan is performed with a slower rate. With too high intensity there is a risk of desorbing all the gas before the scan is finished. However, during the experiment, the beam intensity was constantly adjusted, since the efficiency of desorption may vary between the samples.

Figure 23 shows the results of action spectroscopy with different messenger gases, compared to previously reported data obtained using IR and HREELS. The temperature spectrum is shown for reference.
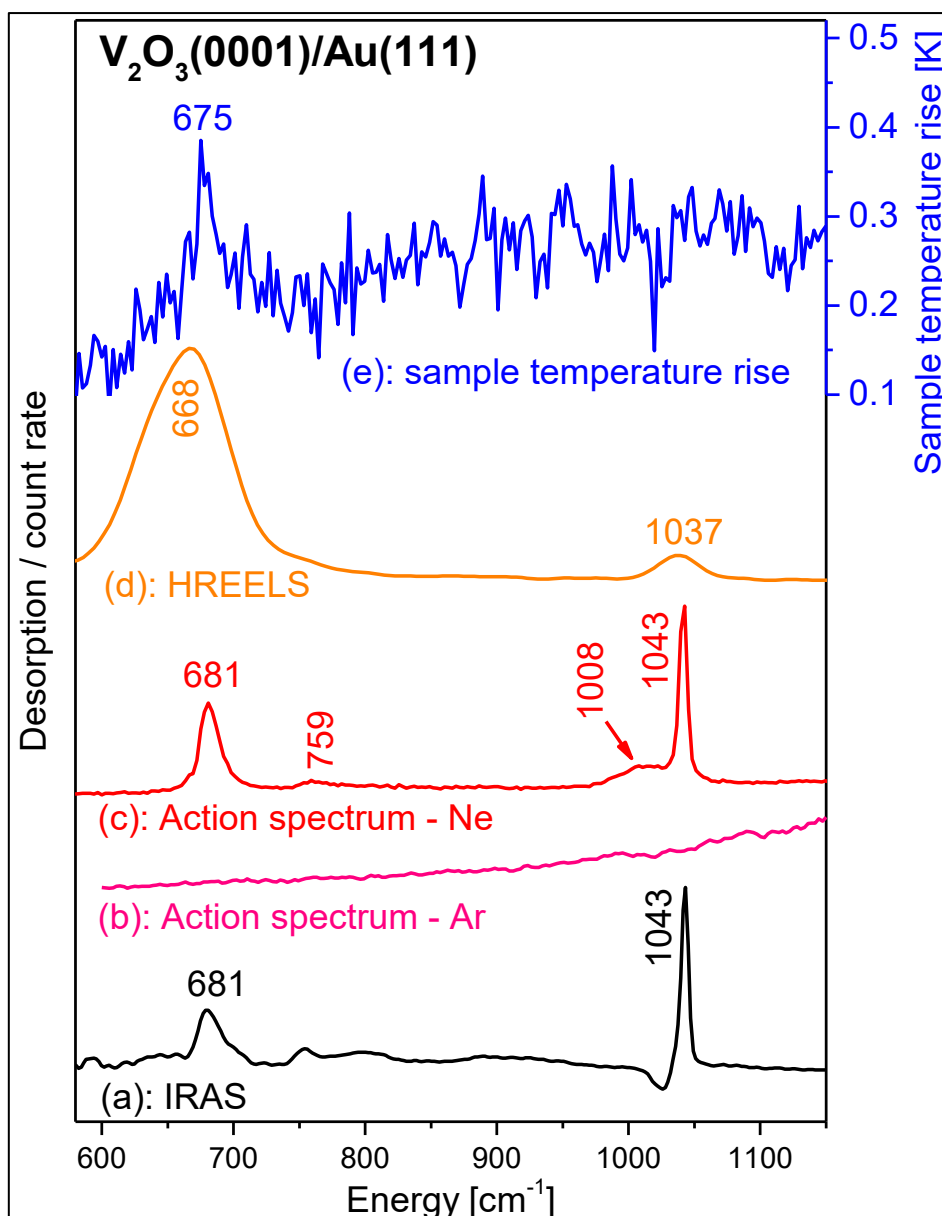
Figure 23 Spectra of V_2O_3 on Au (111) obtained using a) IRAS method, infrared action spectroscopy with b) Ar and c) Ne as a messenger atom, d) HREELS and e) temperature curve. Adapted from [24]

The first curve shows IRAS spectrum with characteristic peaks at 681 and 1043 cm^{-1}. [39] The 1043 cm^{-1} peak originates from V-O vibration in the vanadyl groups, while the vibrations in the 600-700 range are correlated with the bulk. As noticed before, IRAS experiments require a reference spectrum. Therefore, a clean sample is irradiated with electrons, which removes the vanadyl groups from the surface. The reduced surface is highly reactive and by interaction with carbon dioxide, new vanadyl groups are formed,

with lower density and lower dipole coupling. [35] This behaviour is expressed by a negative intensity at about 1025 cm^{-1}, representing the missing vanadyl groups. As a comparison to IRAS, there are presented two vibrational action spectroscopy spectra of Ar (b) and Ne (c). As seen at the spectrum, argon cannot be desorbed from the sample surface, which can be explained by results published by Schlichting [40]. He reports that Ar requires more energy to desorb than Ne. Probably, the amount of energy conveyed to the Ar bond with the sample was too low to cause desorption. In the neon spectrum, compared to IRAS results, there are two additional small peaks at 759 and 1010 cm^{-1}, which are related to the defects at the surface. It is known from STM that V=O vacancies and protrusions are characteristic for V_2O_3. [41] It is possible that the intense 1010 cm^{-1} peak is correlated with vanadyl groups placed next to defects. Curve (d) shows the HREELS spectrum, proving the biggest disadvantage of this method-low resolution. Yet, one can distinguish two peaks- at 668 cm^{-1} (sub-surface mode) and 1031 cm^{-1} (surface), which correspond with previously reported data. [42] As shown on the curve (e), absorption of the radiation and the resulting rise of the temperature, accompanies the surface action spectroscopy method. The peak at 680 cm^{-1} (bulk region) corresponds with the temperature increase. Still, in the Ne spectrum, the intensity at 600 cm^{-1} is incomparably lower, as the method is highly *surface* sensitive, but rather insensitive to *subsurface* and *bulk* vibrations.

In the vibrational action spectroscopy, the energy from the laser radiation is conveyed by direct vibrational coupling from the excited vanadyl vibration, to the bond between the sample and the rare gas atoms.

V=O-Rg (RG=Ne, Ar)

As a result of the vibrational coupling of the vibrational states, energy may be transferred to the O-Rg bond. If the amount of energy is high enough, the rare gas atoms will desorb. The energy transfer will only take place if the vibrational wave function of the excited mode is overlapping with the wave function of Rg vs V=O vibration. This specific condition results in high sensitivity of the vibrational action spectroscopy technique.
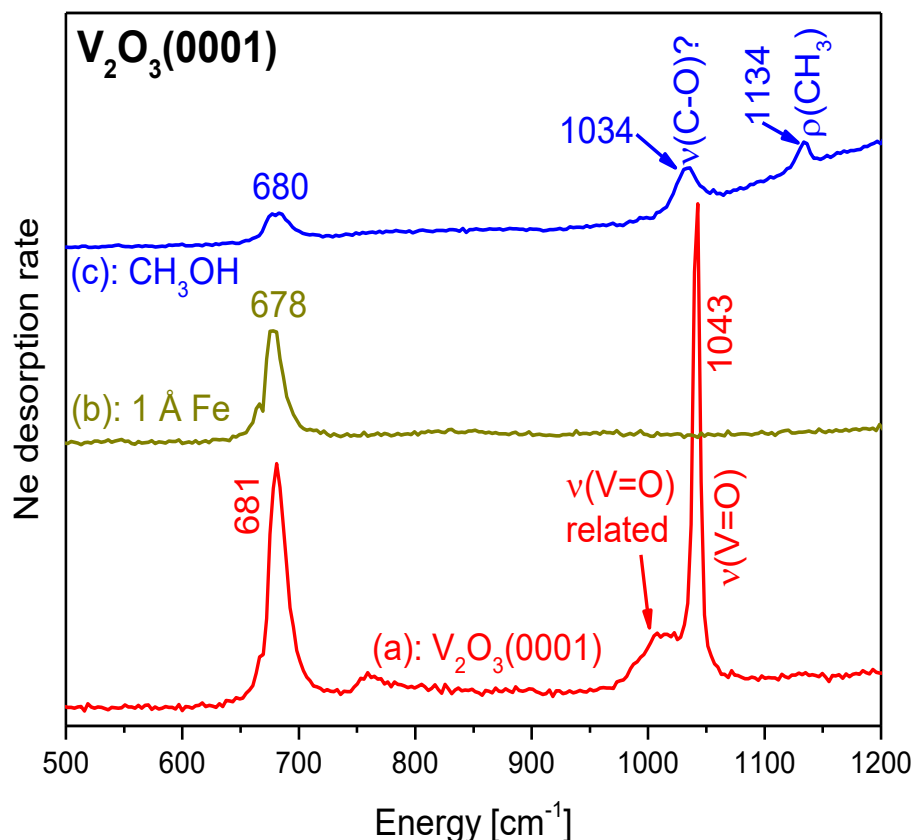

Figure 24 Infrared action spectra of V₂O₃ (0001) on Au (111) a) clean; b) with 1 A of Fe; c) with a monolayer of CH₃OH. Adapted from [24]

For further surface sensitivity investigation, the V_2O_3 (0001) film on Au (111) was covered with the layer of methanol CH_3OH to produce a molecular layer. Such sample was treated as reported by D. Göbke [39] by first dosing methanol at 10K onto the sample, which was then flashed to 200K in order to remove the multilayer, resulting with just a single layer. As seen in Figure 24c, the characteristic surface peaks from vanadyl groups are not visible anymore, replaced probably by the methanol C-O and CH_3 rocking

modes. In the second part of the experiment, 1Å of iron was evaporated at the clean V_2O_3 (0001). As in the previous example, the peak from vanadyl groups disappeared, while the bulk peak at ~680 cm^{-1} decreased its intensity by half. The argument for that intensity may be an insufficient amount of iron at the surface. Still, the presented result show that vibrational action spectroscopy is a highly surface sensitive method.

4.2. Thermal channel

A characteristic feature for single crystal oxides is sample warm-up caused by the excitation of bulk polaritons. Based on the dielectric theory, the heating power $P_{heat}(\omega)$ is equal to the power of the incident beam minus the power of the beam part reflected by the sample surface. For the TiO$_2$ the formula can be adapted as follows, assuming that all the IR light, which is not reflected at the sample, is absorbed by it: [38]

$$P_{heat}(\omega) = \left(1 - R_{TiO2(110)}(\omega)\right) x\, P_{FEL}(\omega) \qquad (4.1)$$

where:

$R_{TiO2(110)}(\omega)$ is the reflectance of the sample;

$P_{FEL}(\omega)$ is the FEL beam power;

ω is the light angular frequency.

The TiO$_2$ (110) single crystal was prepared by cycles of Ar$^+$ sputtering (1 keV, 5 μA) for 30 min at room temperature, followed by annealing at 970 K for 20 min. The initial colour of the crystal is light blue, however, due to annealing, it turns darker. Below (Fig. 25), LEED images of TiO$_2$ are presented. On the left side, the characteristic (1x1) termination of TiO$_2$ (110) is shown. Then, in the next column of images, one can see how the LEED image is changing after dosing Ne/Ar. Both gases desorb easily at low temperatures, as shown in the next column. The far-right image presents the state of the crystal after desorption- clear, bright spots; image comparable to the pre/absorption one.
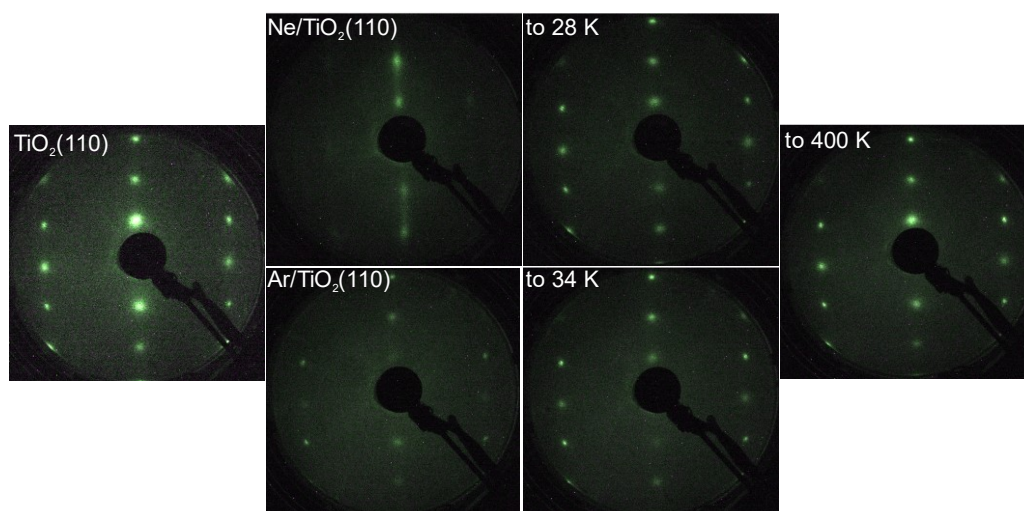
Figure 25 LEED images of TiO₂ (110) clean (the first image), after Ne dosing and annealing to 28K (upper row): Ar dosing and annealing to 34 K (lower row) and after complete desorption of both gases at 400K (the last image).

Figure 26(a) shows an action spectrum obtained for rutile TiO_2 (110) with neon as a rare gas messenger. The blue line displays Ne desorption depending on IR irradiation. The black curve shows the temperature changes, much higher than in the case of $V_2O_3(0001)/Au(111)$. Both lines have two main peaks at 372 and 453 cm^{-1} which correspond with previously reported bulk polaritons. [43] At the same time, the appearance of temperature peaks exactly in the same position as desorption ones, indicates that the process was caused by the sample warm-up [Fig. 26 (b)]. The desorption peaks have a rather symmetric shape, whereas the temperature curve is rather asymmetrical. It suggests that the vibrational energy transfer has also some contribution to desorption. On the other hand, it may also result from temperature maxima.
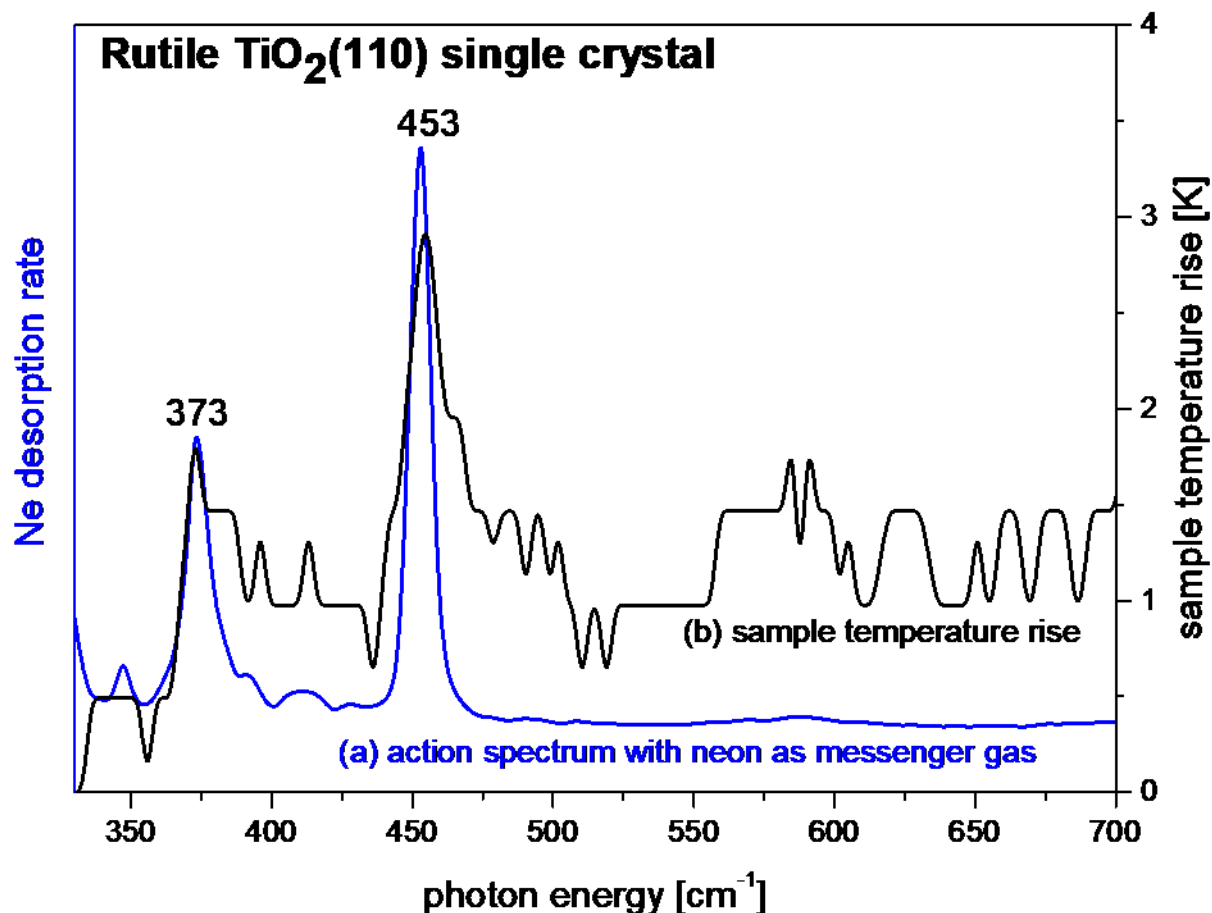
Figure 26. Infrared action spectroscopy spectrum of TiO₂ (110) compared to curve of sample temperature rise.

During the measurement, the temperature increased over 2K, which is higher than in the direct vibrational coupling example for V_2O_3 (0001) on Au (111). [24] The exact temperature is not known, which is connected with mentioned before, inaccurate temperature readings. Probably, due to FEL short, intensive pulses, the temperature is even higher than predicted 2K at the sample surface. The thermal effect can be presumably reduced by lowering the FEL power beam or by improving the conductivity with a thin oxide layer. Another solution may be widening the illuminated area and avoiding local heating.

4.3. Summary

The new FHI FEL apparatus has been successfully used in surface action spectroscopy with rare gas messenger atoms. As shown in the examples above, the method is sensitive to vibrations localized at the surface and rather insensitive to sub-surface and bulk vibrations. The rare-gas desorption can be probably induced just by a single photon, but also due to the excitation of bulk-related states. In that case, it is a thermal process. The results obtained for V_2O_3 (0001)/Au (111) are similar to already published results obtained with IRAS and HREELS. Yet, vibrational action spectroscopy does not require reference spectra and has high resolution. The method may be applied in a wide spectrum of topics in surface science, such as analysing the structural changes in the deposited clusters as well as localized sites like defects at oxide surfaces. Another idea is to decorate only certain areas of the sample with rare gas atoms, by changing the adsorption parameters such as temperature or the amount of the rare gas.

5. *Introduction to CeO$_2$*

Cerium is one of the rare earth elements, which can be found in the Earth's crust. Oxidation of metal Ce with O$_2$ creates various phases. The most common compositions are Ce$_2$O$_3$ (oxidation state III) and CeO$_2$ (state IV). [44] Cerium dioxide (CeO$_2$) has a fluorite structure (CaF$_2$), space group Fm3m. The structure formed by Ce cations is a face-centred cubic with O anions arranged in the simple cubic. [5]
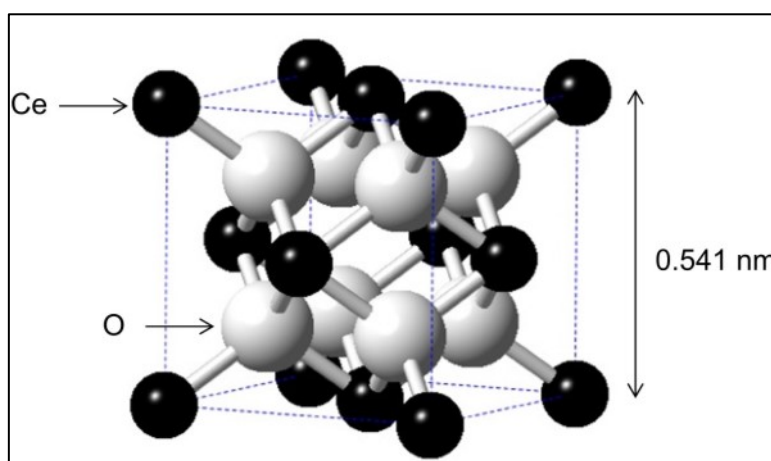

Figure 27. CeO$_2$ structure adapted from [5]

As shown in figure 27, the Ce atoms are bonded to eight neighbouring O atoms, while O anions bond with four Ce cations. Reduced CeO$_{2-x}$ can be formed by diffusion of oxygen, triggered by high-temperature treatment in vacuum or at lower temperatures in a chemically reducing atmosphere. After the diffusion, electrons previously creating a bond with oxygen, occupy 4f band and as a result, ceria is reduced from Ce (IV) to Ce (III) [45]. The reduced CeO$_{2-x}$ has also a fluorite-like structure, with oxygen atoms loosely arranged or ordered around Ce atom. [46]
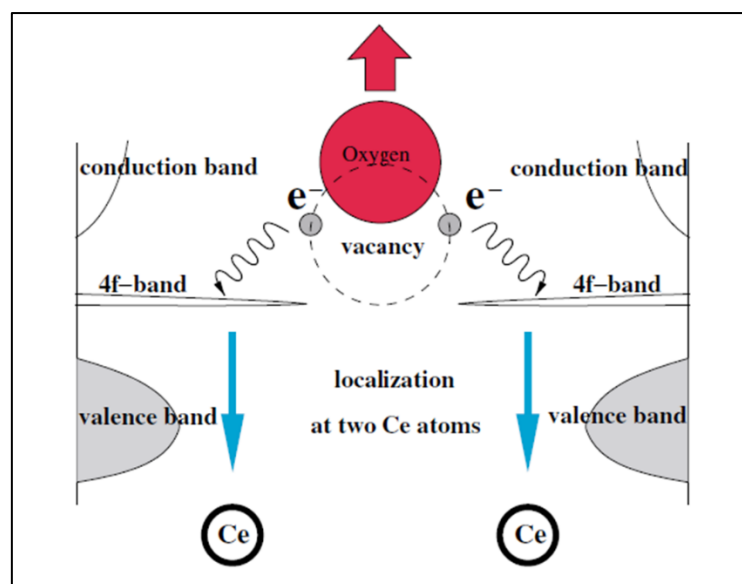
Figure 28 Illustration showing the CeO2 reduction, when oxygen desorbs from the surface creating a vacancy. Adapted from [47].
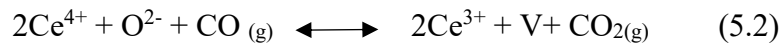
In the case of CeO_2 (111), even though each layer is charged, the charges are balanced within the trilayer, resulting in a lack of dipole moment perpendicular to the surface. Also, CeO_2 (111) is more stable than the (100) and (110) surfaces. [48] It is known from the literature that the band gap of bulk CeO_2 is wide (E_g =4.5 eV). The d shell is closed, which indicates that the electronic configuration is $^1S_0$ state. [5]

Cerium oxide is a prominently applied in many heterogeneous catalytic processes. The most well-known technology, where ceria or its mixed oxide is used, is the three-way catalysts. Three-way catalysts (TWC) is a method of controlling environmental pollution produced by car engines. The method supports the simultaneous CO and hydrocarbons oxidation while reducing NO_x. [44] TWC is a very dynamic process, because of the constant fluctuations in composition, changing temperature and flow rate of an engine's exhaust gases. As a result, it is difficult to characterize the chemical processes that determine the efficiency of the TWC. In order to reduce the fluctuations, it is required that the support structure of the noble metals is able to store oxygen under 'lean'

conditions (high supply of oxygen) and release in 'rich' conditions (oxygen deficiency in the feed). This kind of support has a property called oxygen storage capacity (OSC) and can perform in a wide range of air/ fuel ratios. As an example, it can provide oxygen in CO and hydrocarbons oxidation and cause a reduction of NO_x, when under the 'lean' conditions. To find support with perfect activity, selectivity and durability, many rare-earth metals were investigated [5]. It was proven that one of the most suitable metal oxides is cerium oxide (CeO_2), due to its reversible conversion between Ce^{4+} and Ce^{3+} oxidation states. The process of OSC can be expressed by the *Kröger-Vink* notation:

$$2Ce^{4+} + O^{2-} \longleftrightarrow 2Ce^{3+} + V\bullet + \frac{1}{2}O_2 \qquad (5.1)$$
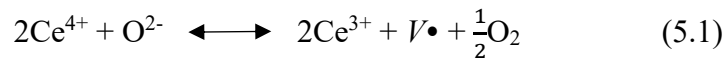
Here, $V\bullet$ is an oxygen vacancy. The equation is also valid in case of reduction at high temperature in a vacuum or in inert gas. Reactions below show the process of reduction with CO or oxidation with H_2O.

$$2Ce^{4+} + O^{2-} + CO_{(g)} \longleftrightarrow 2Ce^{3+} + V + CO_{2(g)} \qquad (5.2)$$

$$2Ce^{3+} + H_2O_{(g)} \longleftrightarrow 2Ce^{4+} + O^{2-} + H_{2(g)} \qquad (5.3)$$

As shown by calculations, the energy required to form oxygen vacancies at the surfaces is 30% lower than in the bulk [45], which additionally increases the dynamics of the reactions. As a result of changing regulations of fuel combustion, higher gas emission temperatures must be obtained. That decreases the performance of CeO_2 in TWC, hence Zr^{4+} were inserted into the ceria lattice, creating a new ceria-zirconia $Ce_xZr_{1-x}O_{2-\delta}$ material. [44] The exact reasons why this material has such good heat resistance and high OSC are still under the investigation.

Another interesting application of cerium dioxide in chemical technology is based on its interaction with hydrogen. Up to date, the main source of hydrogen for the chemical and petrochemical industries is the steam reforming of hydrocarbons:

$$C_nH_m + nH_2O \longrightarrow nCO + (n+m/2)H_2 \qquad (5.4)$$
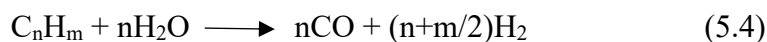
The reaction results with around 10% of CO as an impurity, which requires further processes to provide clean hydrogen. One of them is the CO oxidation:

$$CO + 0.5O_2 \longrightarrow CO_2 \qquad (5.5)$$
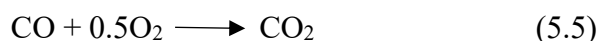
The other is water gas shift (WGS):

$$CO + H_2O \longrightarrow H_2 + CO_2 \qquad (5.6)$$
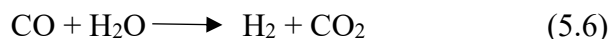
During the reaction, a mixture of Fe-Cr or Zn-Al-Cu is usually used for catalysis. Unfortunately, this procedure requires lengthy and complex activations steps, which lead the scientist to search for alternatives. J. B. Pack and associates report in their work high efficiency in WGS for metals such as Au, Cu and Pt mixed with CeO_2. [49] However, without the support from other metals, ceria has rather poor catalytic properties in WGS. Yet, several studies show that ceria plays an important, but an unknown role in the reaction. [44] [50] The great example is nanoparticles of pure gold and gold oxides on nanoceria. Each of them separately is not able to catalyze the WGS reaction, gold nanoparticles cannot even dissociate water, but together $Au-CeO_2$ has high activity. [51]

Regarding hydrogen, it was demonstrated that the appearance of H species in subsurface layers increases the efficiency of hydrocarbons hydrogenation over Pd surface. [44] The straight forward conclusion would be that the presence of hydrogen in CeO_2 can lead to a similar result. So far, experiments with hydrogen have been conducted only on powder

surfaces with ambiguous conclusions. [5] Analysis using thin films provide a couple additional advantages, compared to single crystal experiments. They allow influencing the structural and electronic properties of the film, depending on the support and increasing the charge transfer between ceria and the substrate. [22] Some studies show that hydrogen absorbs only at the surface [52], others claim that also bulk CeO_2 plays an import role in the hydrogenation [53] [9].
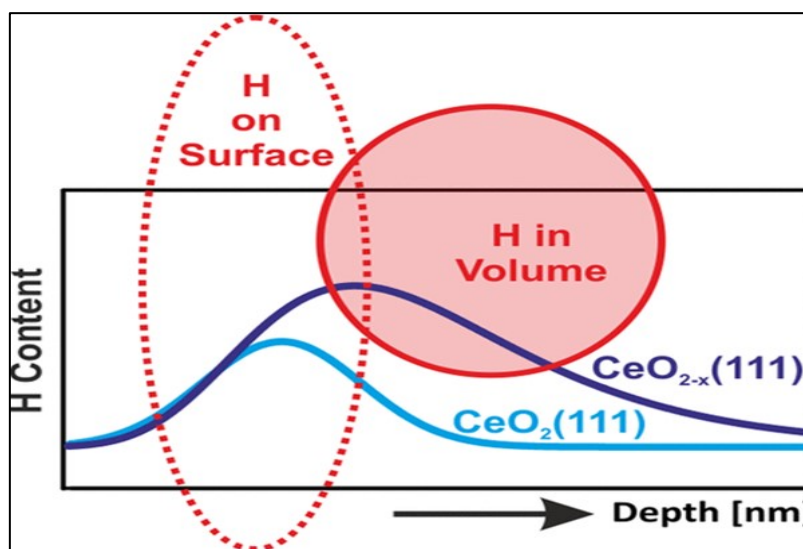

Figure 29 Hydrogen distribution in the stoichiometric and reduced CeO₂ (111) reported by [7]

Werner *et al*. [7] investigated the interaction of H_2 with CeO_2 (111) thin film using IRAS and NRA. As a result, they found that H_2 dissociates in mbar regime pressure. Under this condition, hydrogen dissociates on the stoichiometric surface by forming hydroxyl groups with oxygen from the film. In their work NRA hydrogen depth profiles [Fig. 29] were obtained after a hydrogen treatment at 300 K of stoichiometric CeO_2 (111) and reduced CeO_{2-x} (111). The analyses show that when it comes to the stoichiometric film, H species are in majority located on the surface and only in minor parts in shallow, subsurface region. [7] Since every, even freshly oxidized stoichiometric CeO_2 has a certain number of subsurface defects, such a result is reasonable. Regarding the reduced film, NRA

studies demonstrate H species not only in the surface region but as well in deeper layers, close to 1 nm. [7] Yet, after repeating the studies, only half of the species were detectable, suggesting that H species in CeO_{2-x} are not stable. The hydrogen species formation is still poorly understood. There is little known about the morphology and the electronic state of CeO_2 after hydrogenation. Results presented in this work partially make that process more understandable.

6. Interaction of hydrogen with CeO₂ at room temperature.

In the presented work two systems were studied: 'stoichiometric'- well-ordered CeO_2 (111) and 'reduced'- CeO_{2-x} (111) films on Ru (0001). This section is devoted only to experiments conducted at room temperature.

6.1 Stoichiometric film (CeO₂).

The stoichiometric CeO_2 was prepared as reported. [54] The Ru (0001) single crystal used as a support for CeO2 was cleaned by repeated cycles of sputtering with argon ions of 1000eV energy for 40 min, and then annealing at 1200K for 20 min. As a result, a sharp p(1x1) LEED pattern was obtained as shown in figure 30(A). Once the crystal was clean, it was annealed in 1x10-6 mbar O_2 at 680K to form a 2x2 buffer layer (Fig. 30 (B)). In the next step of the film preparation, ceria was evaporated from Mo crucible at 150K in $1x10^{-6}$ mbar O_2 for about 10 min, then the temperature was increased at the constant rate 1 K/s to 680K. Next step was annealing in the same pressure but at 980K for 20 min. Figure 30(C) shows the characteristic LEED pattern for the first layer of CeO_2, where the Ru(0001) spots are visible. The process of deposition at 680 K, followed by oxidation at 980K, was repeated until the film was about 10 nm thick. The preparation finished with short (~5 min) annealing at 1000K to trigger lattice relaxation. The final state of CeO_2 shows p(1.4x1.4) pattern (Fig.30(D))
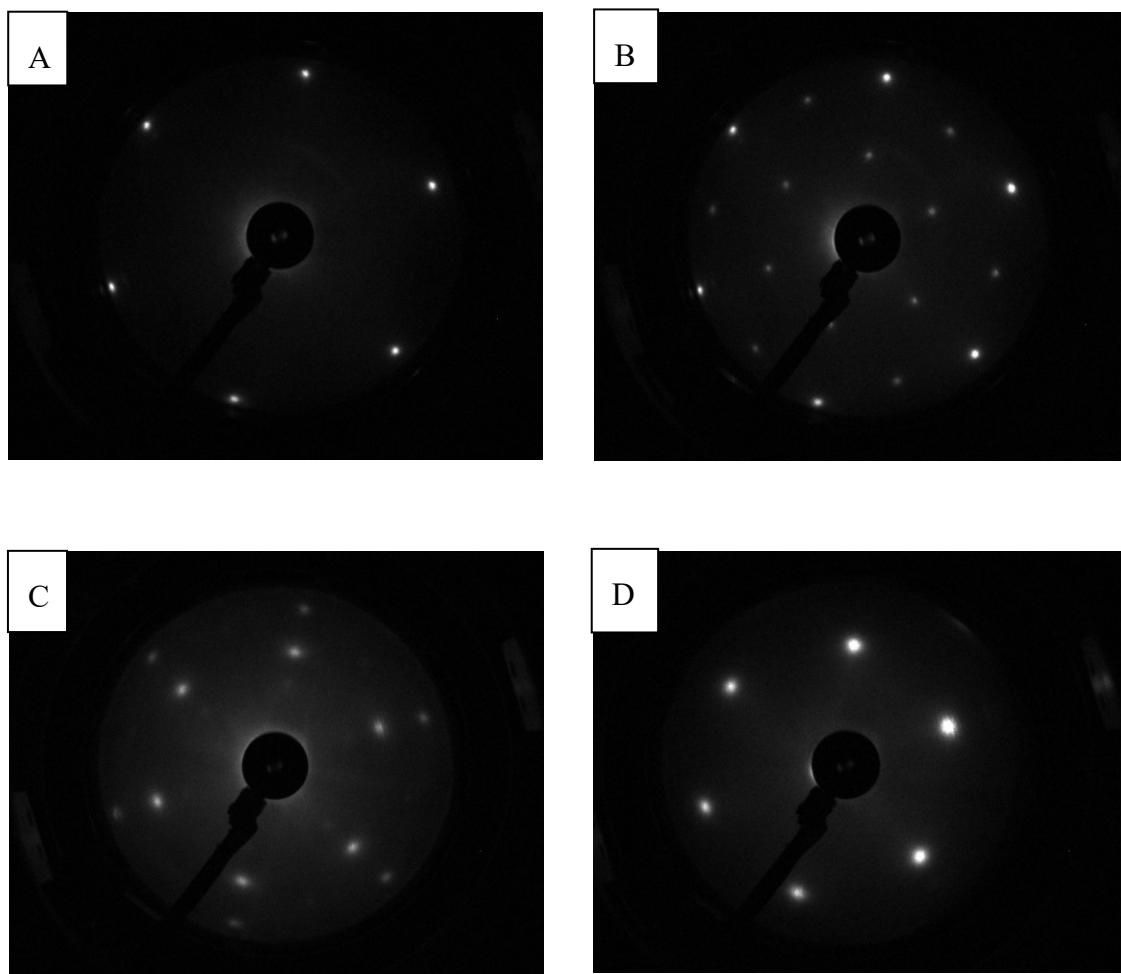
Figure 30. LEED pattern obtained for the clean Ru (A), 2x2 oxygen layer (B), monolayer (C) and 10 nm layer (D) of

CeO$_2$ (C) at 67 eV.

During the sample preparation, an additional experiment has been made. It is common, that after longer exposure to high temperatures thick CeO$_2$ film tends to 'crack', creating terraces and exposing deeper layers. [55] The effect may not be seen in LEED or HREELS results, as the sample penetration by electrons is too low, but may cause false results in the TPD. As a reference, Ru (0001) with 2x2 oxygen layer was treated under the same parameters as later CeO$_2$. Below, figure 31 presents the data of temperature programmed desorption after dosing 10 mbar of H$_2$ for 15 min at the Ru (0001) crystal at room temperature.
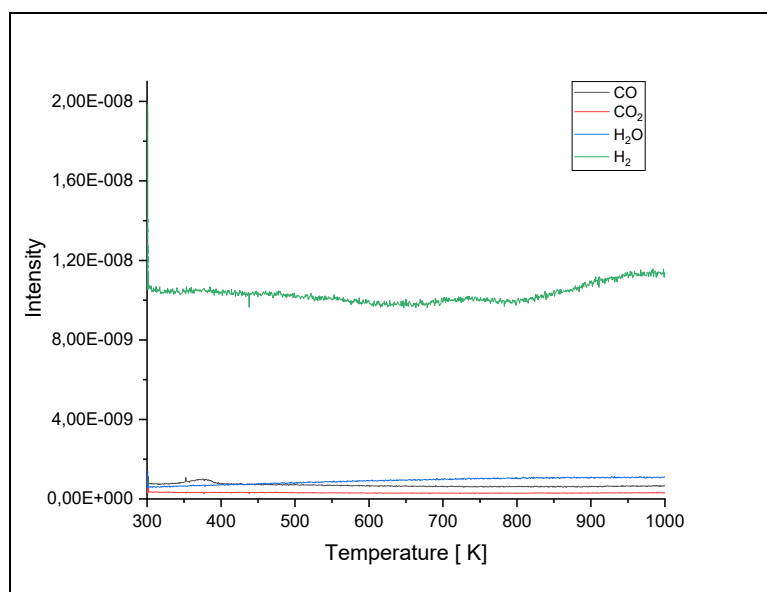
Figure 31 TPD Spectrum of Ru (0001) with 2x2 O layer.

Neither hydrogen nor water desorbs from the surface. The only small peak at around 260 K is visible in the CO curve, which corresponds with was reported before, that this molecule easily absorbs at Ru (0001) [6]. Subsequently, CeO_2 was prepared as in the written above recipe.

The quality of the CeO_2 surface was examined in the TPD experiment. For that, the sample was transferred to the high-pressure cell, where 10 mbar of H_2 for 15 min was dosed. The TPD experiment had two purposes. Firstly, a reference spectrum of the oxidized surface was required, as we assume that the number of vacancies play important role in hydrogenation. Secondly, verifying the result obtained by Werner *et al*. [7], suggesting the formation of the hydroxyl group. Figure 32 presents data obtained through temperature programmed desorption. The experiment was performed until 1000 K with a constant rate of 1K/s. From the desorption curves, one can see that there are no desorption peaks from hydrogen, which means that under described parameters, it cannot absorb at the surface. This result corresponds with reports on the relationship between H_2

dissociation efficiency and the pressure. [9] At the same time, there is no contamination

in the form of either CO or CO_2, which agrees with previous reports. [5] What is

characteristic in these results, is the lack of water desorption, which also corresponds with

HREELS results. Results of previous studies show that hydroxyls cannot be formed by

exposure to molecular H_2 at low pressures [9], unfortunately, no studies were done for

high-pressures hydrogenation. However, hydroxylation of CeO2(111) can be achieved by

dissociation of water on reduced CeO_2(111) [56] [57] or by adsorption of atomic H [58]
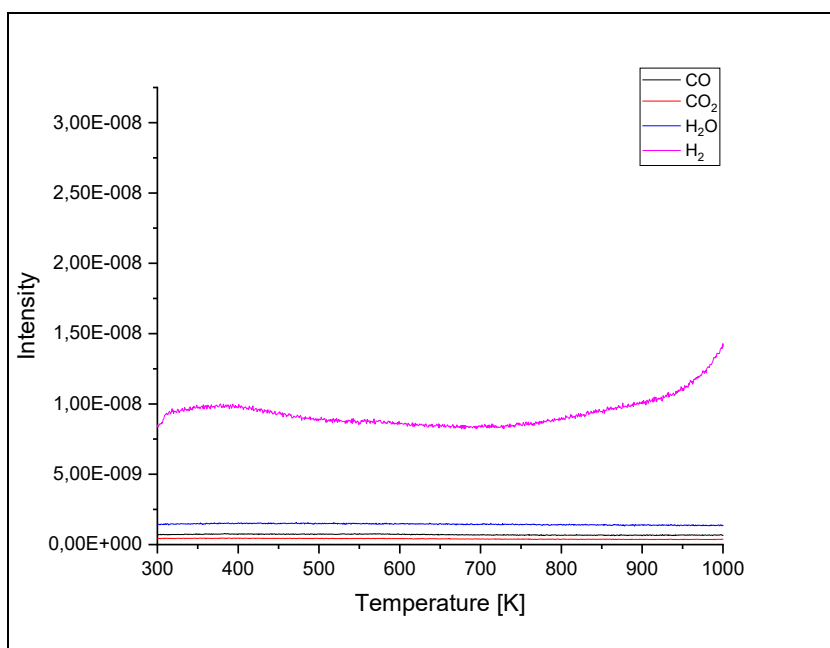
[59].

Figure 32 Temperature programmed desorption curve of the stoichiometric CeO2.

Vibrational properties of the CeO_2 were investigated using HREELS technique. The

figure shows a typical HREELS spectrum of CeO_2 with the characteristic peak at 67

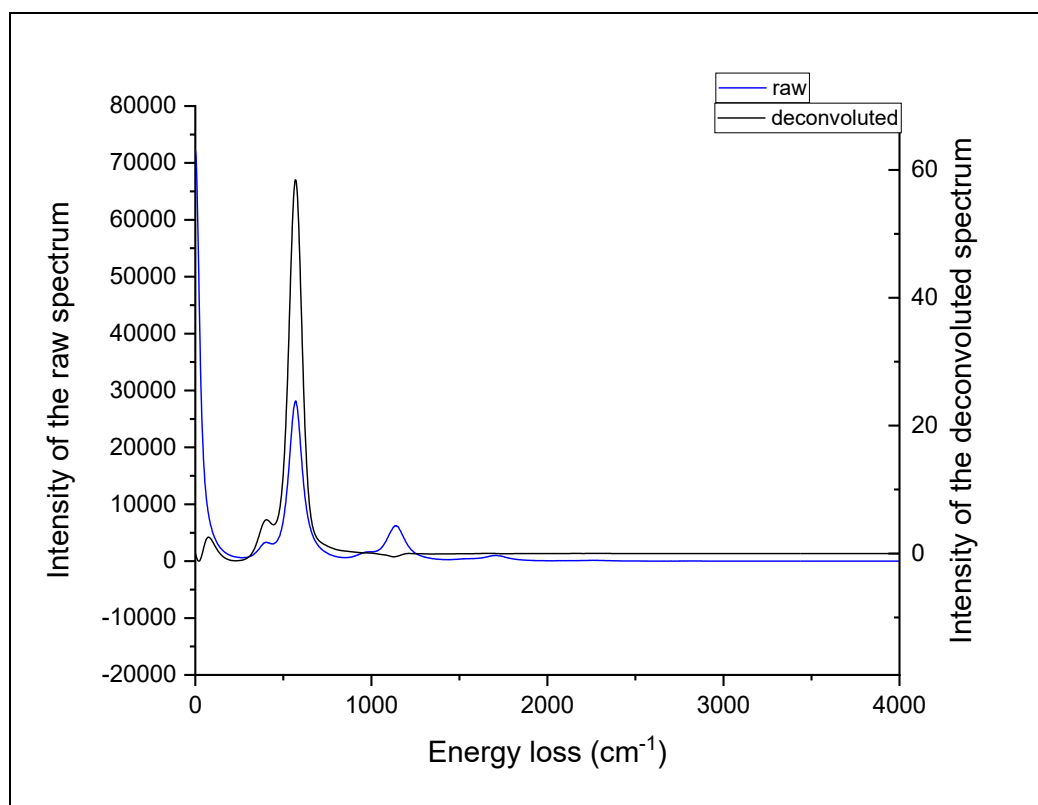meV. Presented spectrum is in a good agreement with the spectra reported previously [5].

Figure 33 Deconvoluted HREELS spectrum of the stoichiometric CeO₂ (black line) compared to the raw spectrum (blue line). FWHM= 4meV.

An EELS spectrum [Fig. 34] of the stoichiometric CeO₂ surface shows an increase of intensity at about 3 eV with two main losses at 4 and 7 eV. The calculated energy gap for this region is equal to 3 eV, which corresponds with the presented results. The energy loss I at 4 eV is correlated with O2p→Ce4f charge transfer transition. [60] The excitation of an electron from the oxygen valence band into ceria's empty band gap state is required for the charge transfer. The transfer leads to the change of configuration to Ce $4f^1$ and to splitting from $^1S_0$ ground state to $^2F_{5/2}$ and $^2F_{7/2}$ states. [61] The second energy loss at 7 eV is correlated with the band gap transition between O 2p and Ce 5d/Ce 6s conduction band states, from DFT calculations this value should be around 5 eV. [60]
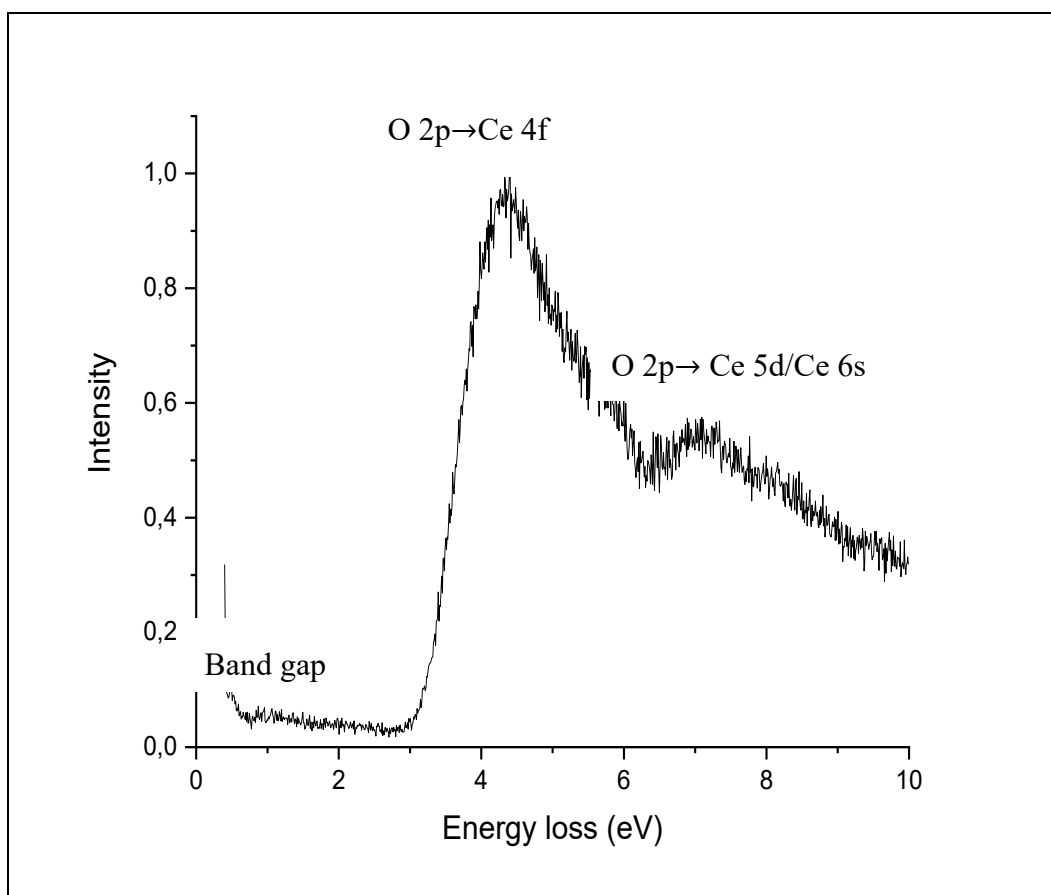
Figure 34. EELS spectrum of the stoichiometric CeO$_2$.

It should be mentioned that STM experiments were performed in the different UHV

chamber than experiments with other, already mentioned methods. Still, the film was

prepared using the same recipe and the quality of the surface was compared using LEED.

However, the STM images may not fully represent the surfaces obtained with the

HREELS technique. The STM investigation shows that the quality of the CeO$_2$ film may

vary between the preparations. The low conductivity of the stochiometric thick film

required using very low tunnelling current, plus sample was slightly reduced- CeO$_{1.99}$.

[54] The surface is not completely flat, but it includes terraces, plus structure seems

granular [Fig. 35]. All the STM images presented in this thesis were obtained using Pt-Ir

tips at room temperature. The sample bias voltage was 4 V and tunnelling current around
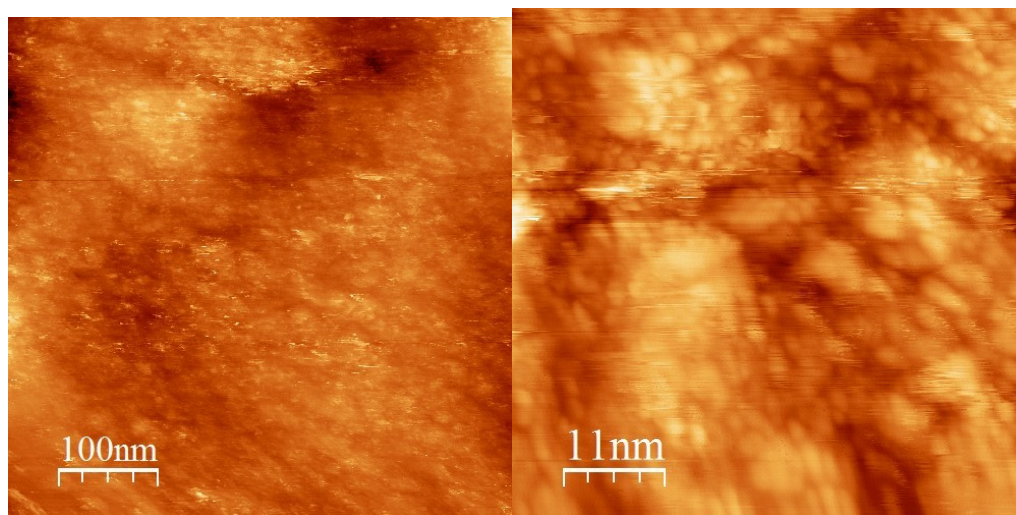
0.2 nA. The surface roughness was around 3.6 nm.

Figure 35. STM images of 10 nm ceria grown at 680 K. Bias voltage=4 V, tunnelling current=0.2 nA.

6.2 Reduced film (CeO$_{2-x}$).

Introduction

A significant amount of scientific work has been contributed towards understanding

reduced surface and bulk CeO$_2$. Oxygen vacancy defects play an important role in the

surface reactions. [59] [7] There are different forms of vacancies. Single vacancies are the

rarest, linear clusters appear only under special treatment, while the most common is the

triple vacancy. [48] As the AFM study by S. Gritschneder shows [45], the freshly

prepared stoichiometric CeO$_2$ is covered with a mixture of defects and adsorbates from

the residual gas, such as water. A number of studies report, that due to the oxygen defects

formation, f states of the ceria atoms, placed nearest to the vacancy NN (Nearest

Neighbours) are occupied. [46] [62] [63] V. Ganduglia-Pirovano *et al.* showed theoretical

proof that the oxygen subsurface vacancy is more stable than the surface one. [53] In her

work she demonstrates this stability is resulting from defect-induced lattice relaxation.

The model in figure 36 shows the ion distribution in the reduced (2x2) model unit cell.
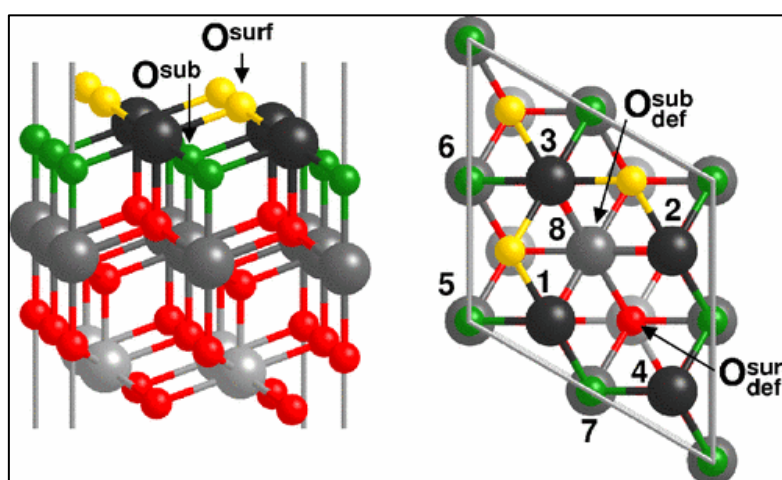

Figure 36. Structural model of the (2x2) CeO$_2$ cell. Adapted from [53]

In case of surface vacancy, the two additional electrons can situate either on two Nearest

Neighbours (NN) Ce (atoms 1 and 4 on the Fig. 36) sites or a mixed pair NN and Next-

Nearest Neighbour (NNN) (atoms 2,4 and 3 on the Fig. 36). [53] Subsurface vacancy has

an additional choice of sole NNN location. She reports that after creating a surface

vacancy NN ceria atoms move away from the empty negative ion, whereas NNN are

attracted by the vacant site, which produces tension-compression centres in the lattice. To

support this theory, the Madelung potential [1]was calculated for all possible positions of

ions in surface and subsurface configurations. The lowest magnitude was obtained for the

subsurface defects, with Ce^{4+} ions in NN position.

---

[1] Madelung potential describes the electric potential of all ions in lattice on the individual ion.

Results

The reduction of the film was performed by annealing the sample for 5 min in 1200 K in vacuum. Since reduced film attracts more contamination than the stoichiometric film, before the experiments with hydrogen, the CeO_{2-x} was additionally flashed to 500 K in UHV in order to desorb any molecules that could adsorb from the background pressure of residual gases. The quality of the film after reduction can be seen on the LEED image (Fig. 37). The spots are blurry and less intense, plus the background is brighter.
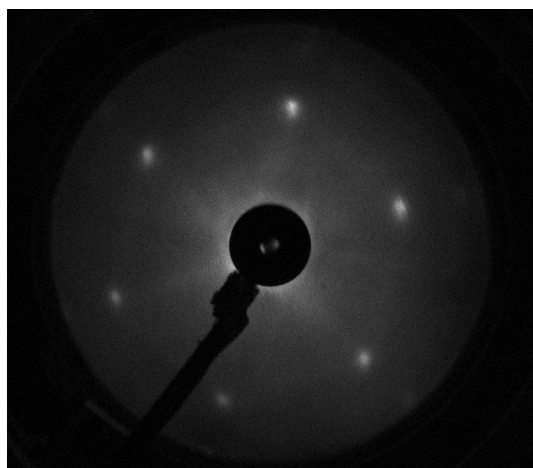

Figure 37. LEED image of the reduced CeO₂ obtained at 67 eV.

The effect of reduction was also significantly visible in the EELS spectrum, due to the appearance of Ce^{3+}, which modifies the local electronic structure and geometry. EELS spectra before and after reduction by annealing are shown in figure 38. The temperature treatment causes a decrease in the loss I, which is a fingerprint of reduction Ce^{4+} to Ce^{3+}. Special attention should be paid to the band gap region of the spectrum since the occupation of the band reflects the lower oxidation state. Reduction of the ceria atoms should lead to increasing of the intensity in this region, as seen in the spectrum, reflecting the presence of Ce 4f electrons; as a result, the band gap region is shorter. Higher

intensity of the curve around 1 eV may be also caused by be multiple phonon loss
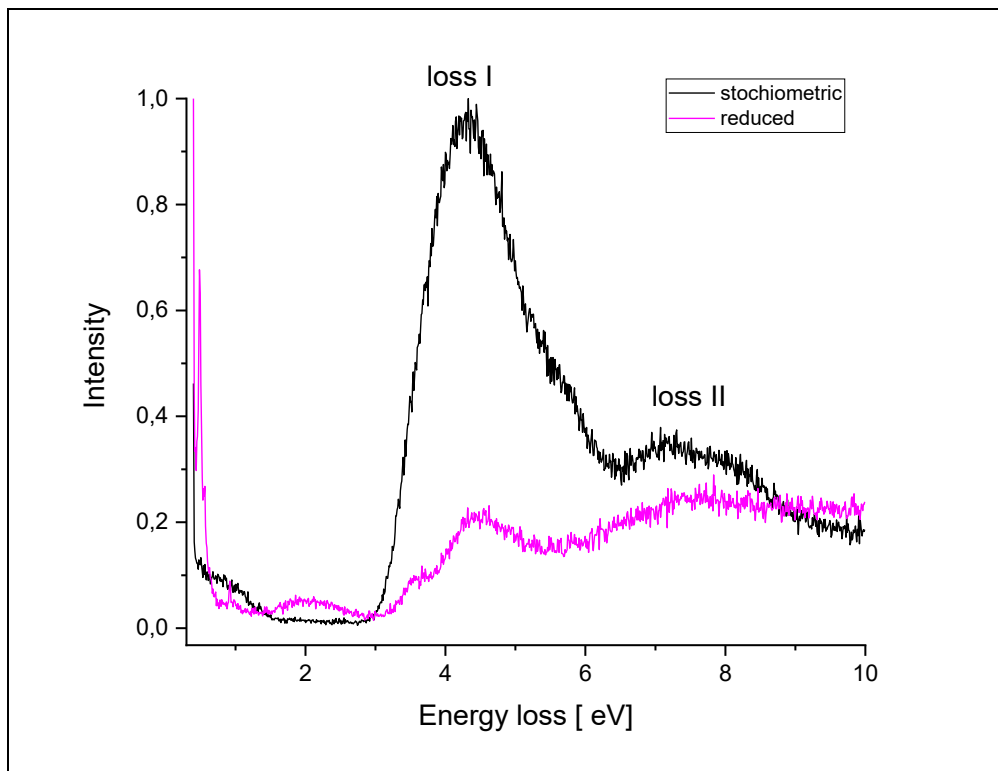
intensity. [60]

Figure 38. EELS spectrum of the reduced CeO2-x compared to the stoichiometric CeO2.

As mentioned before, the quality of the film and the concentration of the defects can vary

between the preparation conditions. Since the STM results were obtained in the different

UHV setup, the correlation with the HREELS results may not be straightforward. Figure

39 displays the STM image of the reduced CeO_{2-x}. As in the case of stoichiometric film,

the surface consists of the large terraces with additional defect sites seen as dark and very

bright points, which may be associated with the oxygen vacancies. Those irregular sites

(defects, terraces and steps) may later play an important part in the hydrogen adsorption.

However, due to the reduction process, the roughness of the film decreased to 2,2 nm.
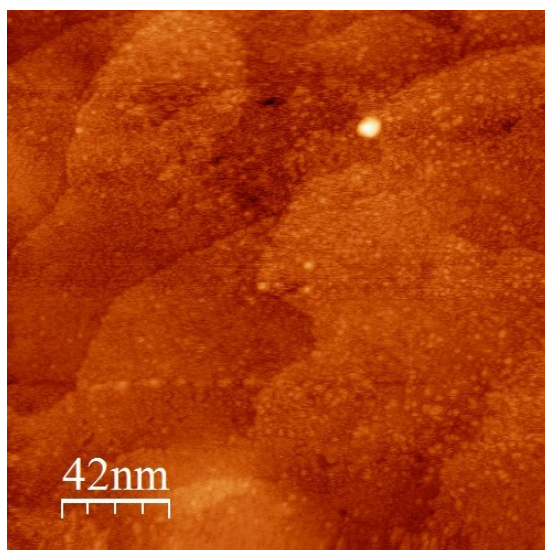
Figure 39. STM image of the reduced CeO2. Bias voltage=4V, tunneling current=0.2 nA.

Figure 40 demonstrates the TPD results of the reduced CeO_2. In this case, the sample was transferred to the high-pressure cell, however, no hydrogen was dosed. The point of this experiment was to control the influence of contamination from the background pressure in the high-pressure cell, which during experiments with hydrogen was usually in the 10^{-9} mbar range.
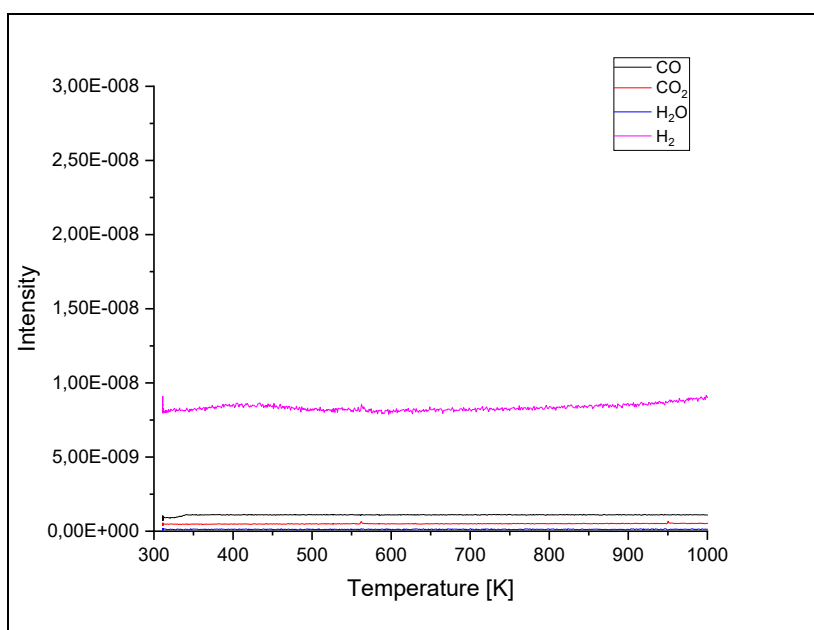

Figure 40. Temperature programmed desorption curve of the reduced CeO_{2-x}.

As seen on the curve above, there is no sign of hydrogen desorption. The only visible peak is at about 400 K, which was previously reported for the Ru (0001). [64] Apparently, during reduction, the CeO_2 must have cracked in the way that it is exposing the substrate, as previously assumed from the LEED image. Rise in the hydrogen curve at around 850 K is created by desorption from the sample plate, which was later confirmed in the blank experiment, without the sample. Importantly, neither CO nor CO_2 adsorbed at the surface, meaning that theoretically, they should have no influence on the hydrogenation results.

6.3 Interaction with hydrogen.

<u>Ceria and hydrogen</u>

Apart from the cases mentioned in chapter 5, redox properties of ceria can be also used in the hydrogenation reactions such as partial hydrogenation of light alkynes in the gas phase and complex alkynes in the liquid phase. [54] The studies show that the highest efficiency of the reaction was on condition of elevated temperature (>500 K) and large hydrogen excess (H_2/ alkyne > 25). During the reaction, hydrogen dissociates on the ceria surface instead of creating oxygen vacancies. There are two different mechanisms of the interaction between H_2 and CeO_2. The first one assumes the homolytic split and formation of two O-H groups, the second- heterolytic split with Ce-H and O-H as an outcome. Likewise, experimental methods provide similar results of hydrogen dissociation over metal oxides with either homolytic O-H or mixed with metal-hydrogen bands infrared spectra. [44] [10] A mechanism was proposed by Vile and co-workers, where homolytic

dissociation takes place, but this time forming Ce hydride intermediates instead of O-H.
[65] Moreover, they suggested heterolytic dissociation of hydrogen on Ce-O bond and as
a result transfer of H atom to Ce. However, their work was performed on the CeO_2 rods,
with an unclear amount of surface defects. Still, there is no vibrational spectrum proving
Ce hydride formation over CeO_2, which would be visible in the 1500-2000 cm^{-1} range.

The experiment

The experiment with hydrogen took place in the high-pressure cell. Before transferring
the sample from the main chamber, it was flashed to 500 K to remove any contamination.
As mentioned before, that was not the only precaution against impurities in the chamber
[see section 3.1.]. After the sample transfer, the valve between the chamber and the cell
was closed. Next, 10 mbar of H_2 was dosed for 15 min. The dosing took place at room
temperature, with the constant gas flow. The sample was then transferred to HREELS
chamber, as the experiments were always in the order HREELS> LEED > TPD, to
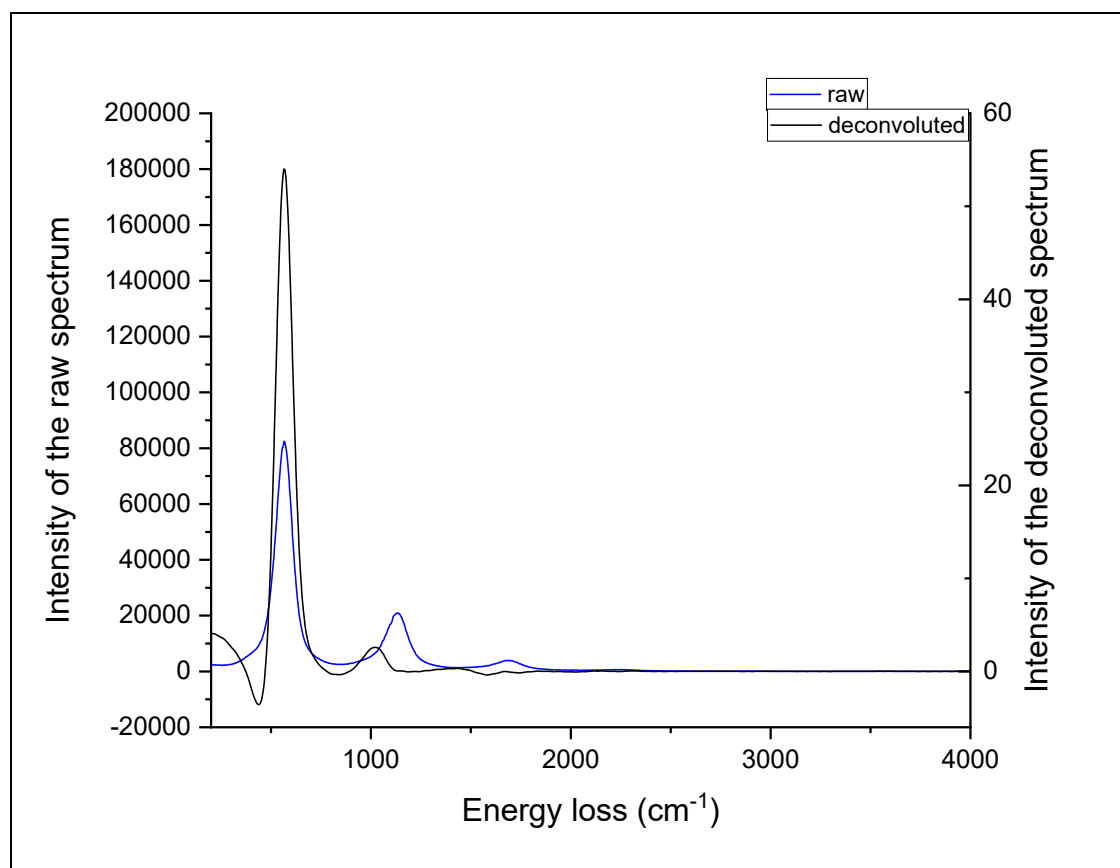prevent the destruction of the hydrogen layer.

Figure 41. HREELS spectra of the CeO$_{2-x}$ after hydrogenation before (blue line) and after (black line) deconvolution.

FWHM=6 meV.

Figure 41 demonstrates HREELS spectrum of CeO$_2$ after interaction with hydrogen.

What is significant here is that there are no signs of reduction at the surface, such as

changes in the peak shape. [60] The characteristic vibrational frequencies for adsorbed

OH and H$_2$O species in the range of 3600-3900 cm^{-1} are not visible. That proofs that

hydrogen did no dissociate forming stable O-H bond. Werner *et al.* presented the DFT

calculations showing that as much as on the surface it is not favourable to form H$^-$ in the

oxygen vacancies (endothermic process, ΔE H$_2$= + 76 kJ/ mol), the same behaviour in the

bulk is energetically neutral (+ 4kJ/ mol). [7] Moreover, it is more suitable than -OH

formation with ΔE= 39 kJ/mol. According to work by Z. Wu hydrogen species may be

visible in the range around 1000 cm^{-1} [66] , which is the position of the peak in the

HREELS spectrum. The intensity may also be an artefact of the deconvolution process.

Therefore, I cannot clearly assign the intensity to hydride vibrations, but it is possible that

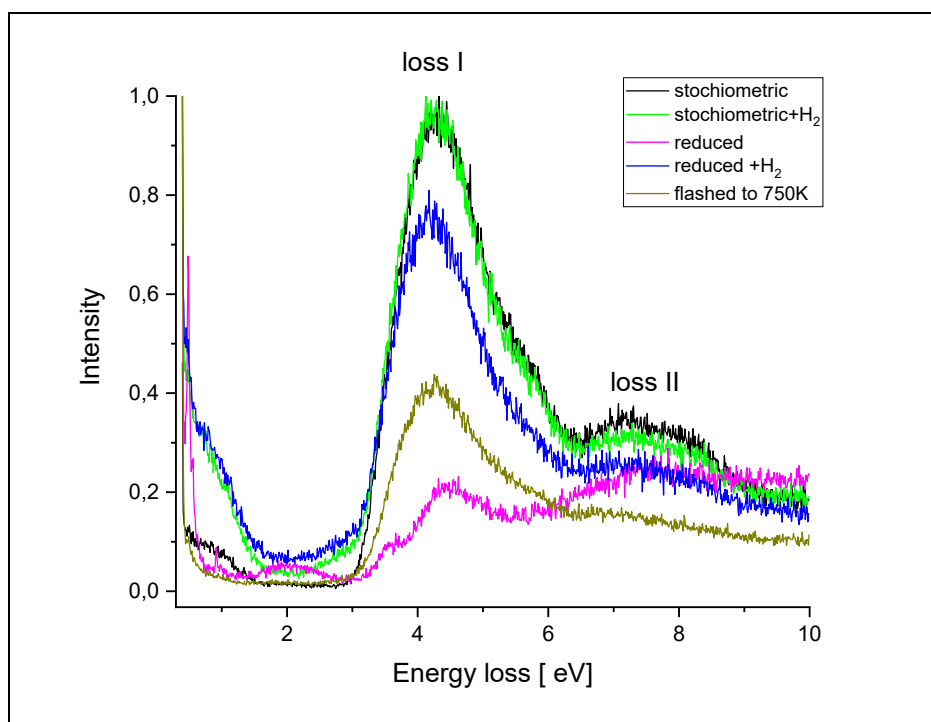at least part of the intensity is due to such vibrations.

Figure 42. EELS spectra of stochiometric, reduced and reduced after hydrogenation ceria film.

The EELS spectrum [Fig. 42] demonstrates that the presence of H can reconstruct the

valence band structure. As the valence band is determined by, among others, the atomic

positions, the H_2 must have some sort of influence on the atomic structure of the surface.

Oxidation from Ce^{3+} to Ce^{4+} is possible, as the intensity of the loss I after hydrogenation

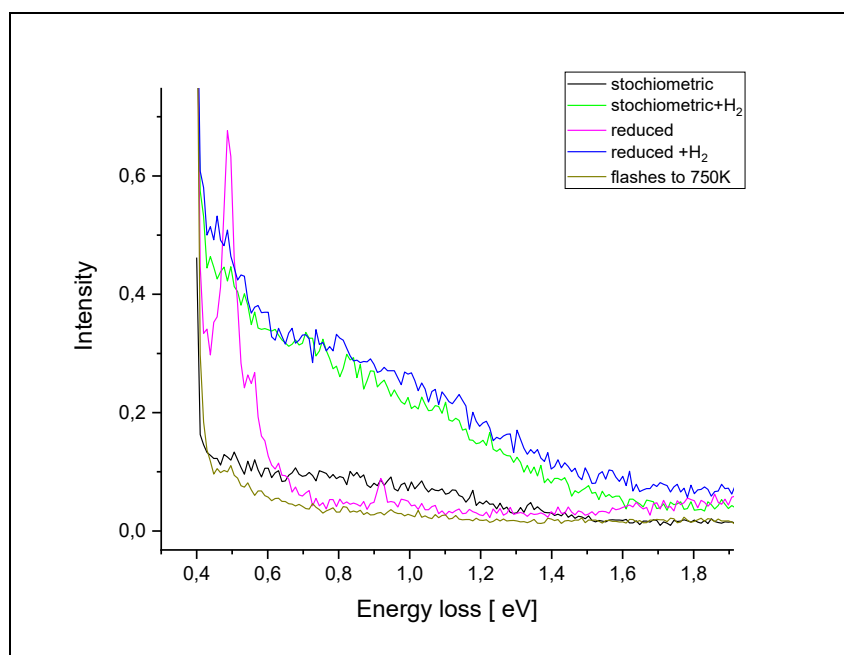is almost as high as the intensity of the stoichiometric film.

Figure 45 Part of EELS spectra with the zoomed in band gap region.

Figure 45 presents the first 2 eV of the EELS spectra, the band gap region. In the cases of
both stoichiometric and reduced samples with hydrogen, compared to the surfaces
without hydrogen, there is a rise of intensity from 0.4 to 1.8 eV. It may be an indication of
a hydride formation. The intensity does not come from Ru, as the stoichiometric film
complete covers the metal, which was examined by LEED. Plus, after flashing the
samples to the temperature where hydrogen desorbs ~750K, the intensity of the curves
degreases.

Another argument favouring the reconstruction of the reduced film by hydrogen is
provided by the LEED experiment. The result is shown in figure 46. As in the case of the
stoichiometric film, the spots in the diffraction pattern are sharp and bright and the
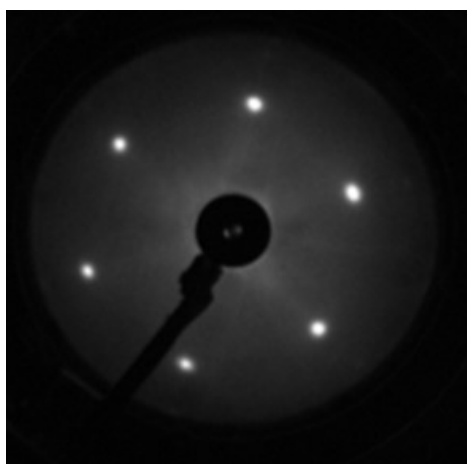background intensity is low.

Figure 46. LEED image of the re-oxidized CeO$_2$ after the interaction with H$_2$, taken at 67 eV.

Figure 47 presents the thermal desorption spectra of H$_2$, CO, CO$_2$ and H$_2$O measured after adsorption of hydrogen at room temperature. Hydrogen curve (pink colour) has two main features starting at around 550 K and 650 K. Because those results were not observed before by other groups, the experiment was repeated three times. Still, the origin of the peaks is not yet clear. They may be attributed to hydrogen desorbing from the surface or near-surface oxygen vacancies in case of the peak at 550K and deeper, bulk oxygen vacancies at 650 K. Interestingly, still there is no contribution from water as well as contamination in the form of CO or CO$_2$.
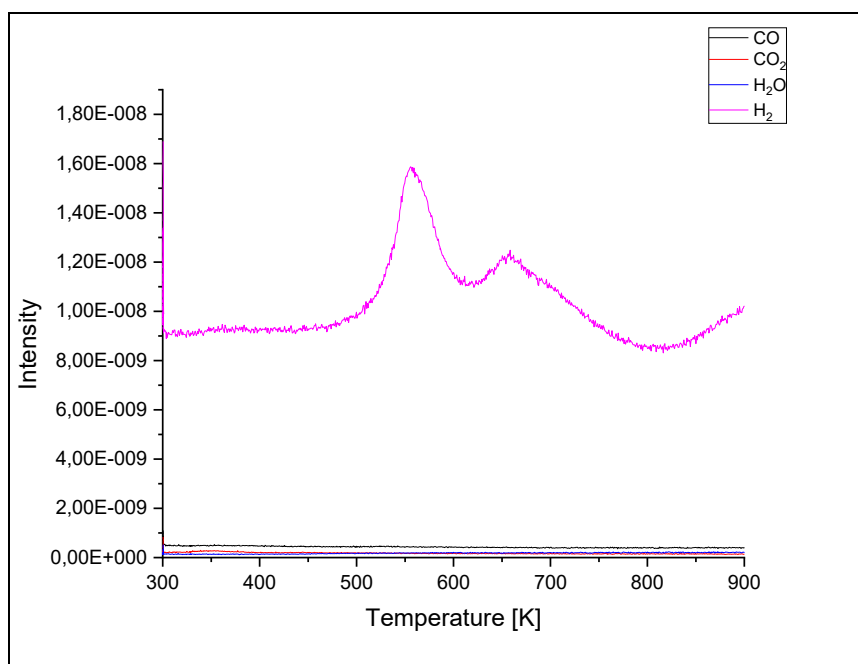
Figure 47. TPD spectra of H_2, H_2O, CO and CO_2 after hydrogenation of CeO_{2-x}.

To better understand the origin of the thermal desorption peaks, additional measurements
have been performed, where the surfaces had a different state of reduction. The state of
reduction is based on the intensity of the fingerprint Ce^{3+} peak observed in the EELS
spectra (loss I) [Fig. 48]. It was assumed that the lower intensity is equal to a more
reduced state. The reduction degree was also confirmed with LEED measurements, where
with an increasing amount of vacancies, spots at the images were becoming blurry while
the background was more intense [Table 1]. The results let suggest that despite the state
of reduction, hydrogen is covering the surface in the same degree. In both cases of weak
and strongly reduced film, with the same procedure of hydrogen exposure, the same
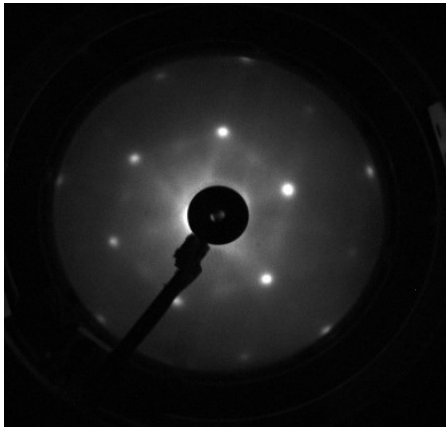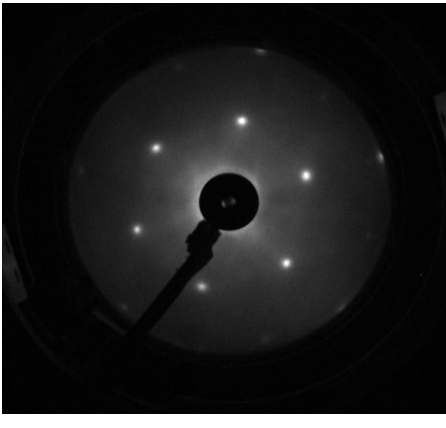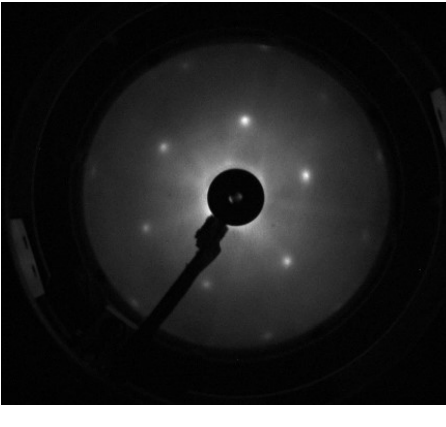results were obtained with the nearly stoichiometric electronic state.
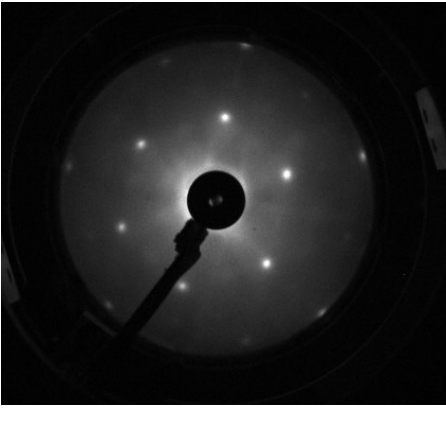
	Reduced	After hydrogenation
Weakly reduced		
Strongly reduced		

Table 1. Comparison of LEED images of CeO$_{2-x}$ with different degrees of reduction.
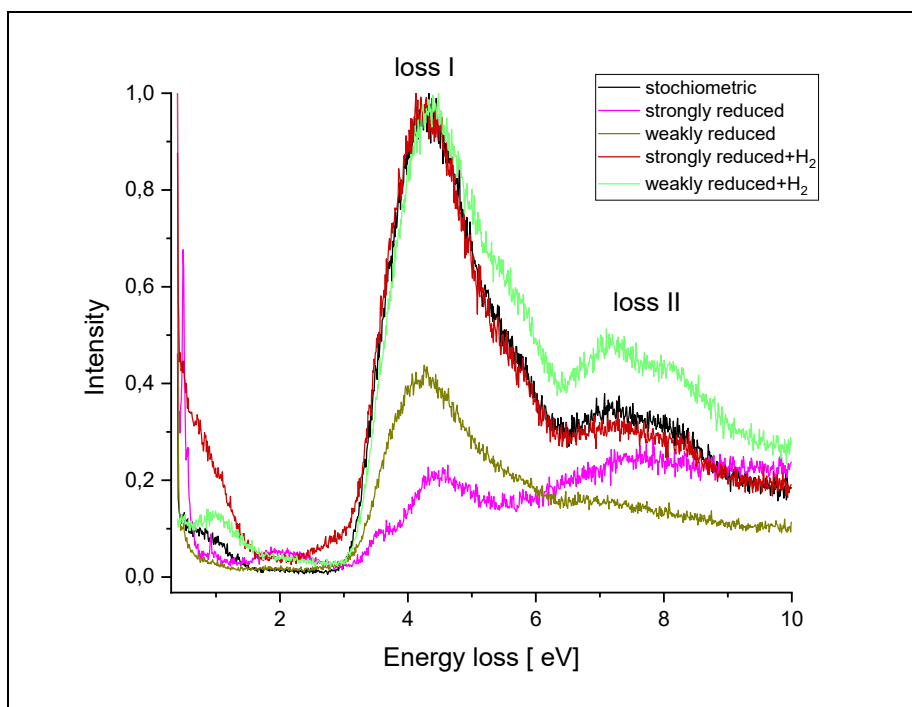
Figure 48. The comparison of the EELS spectra for the hydrogenation of CeO$_2$(111) with different degrees of reduction.

The STM image [Fig. 49] demonstrates that on the contrary to what previous methods showed, hydrogen is negatively changing the surface. Compared to the STM image before the hydrogenation, the amount of protrusions is much higher with some sort of clusters being created. The roughness also increased to around 11 nm.

Figure 49 STM image of the CeO$_{2-x}$ after hydrogenation. Bias voltage= 4V, tunnelling current=0.2 nm.

6.4 Reduced CeO$_2$ after the hydrogen desorption.

After desorption of hydrogen, the CeO$_2$ surface was further investigated. The purpose of this part of the experiment was to evaluate the influence of hydrogen and other contaminations on the sample. Based on the literature, it was expected that elevated temperature during the TPD 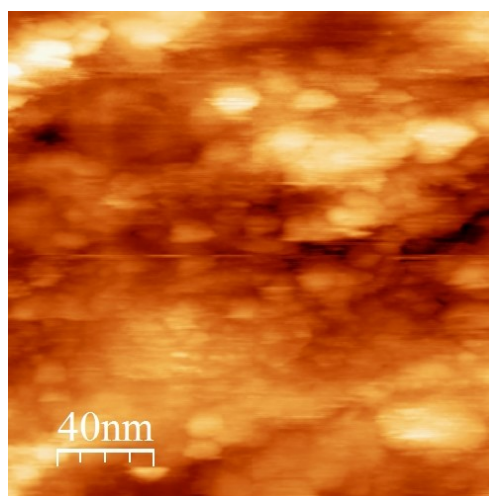will activate the reduction by hydrogen [66], which in this case was not seen. Figure 50 presents the desorption of gases from the reduced surface, after exposing it to residual gases for one hour. Still, there is no hydrogen no water desorbing from the surface. There is a small peak at the CO curve, probably from exposed Ru (0001).
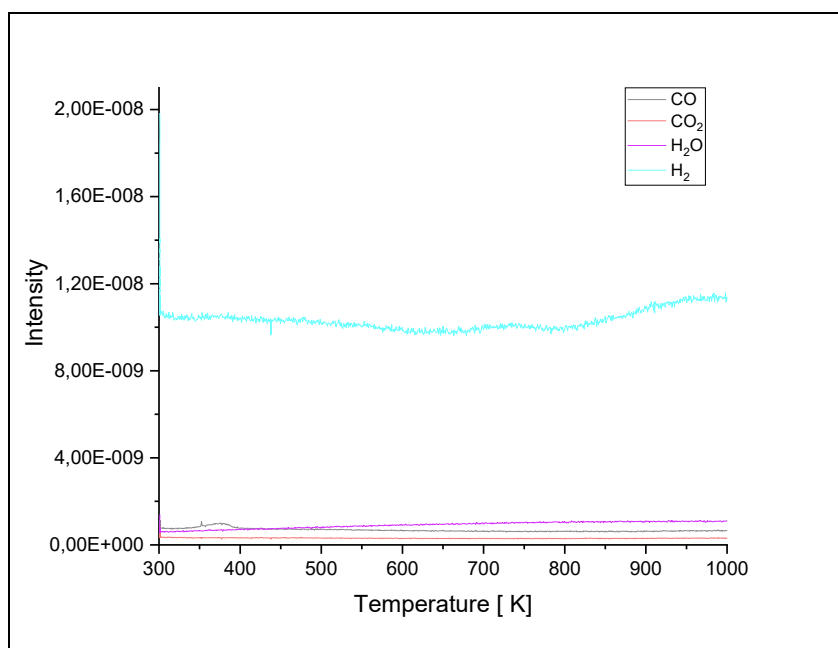

Figure 50 Temperature desorption spectrum of the CeO$_{2-x}$ after hydrogen desorption.

The comparison of EELS spectra is presented in figure 51. The dark blue curve, representing the electronic state of the sample after the TPD is more intense in the loss I than the curve of the reduced sample. It can be explained by results reported by *Duchon*

et al. [67] that in the case where the surface of the film is partially reduced, at the
temperature around 600 K, oxygen from the bulk of the CeO_2 is being transported to the
top layers. Such behaviour results in the formation of CeO_{2-x}, both in the top and sub-
surface layers. In EELS spectra such behaviour would appear in the almost stoichiometric
intensity of the loss I. It is important to mention that according to the EELS data, after the
hydrogen desorption, the surface can be re-oxidized to the stoichiometric form and the
hydrogenation process can be repeated.
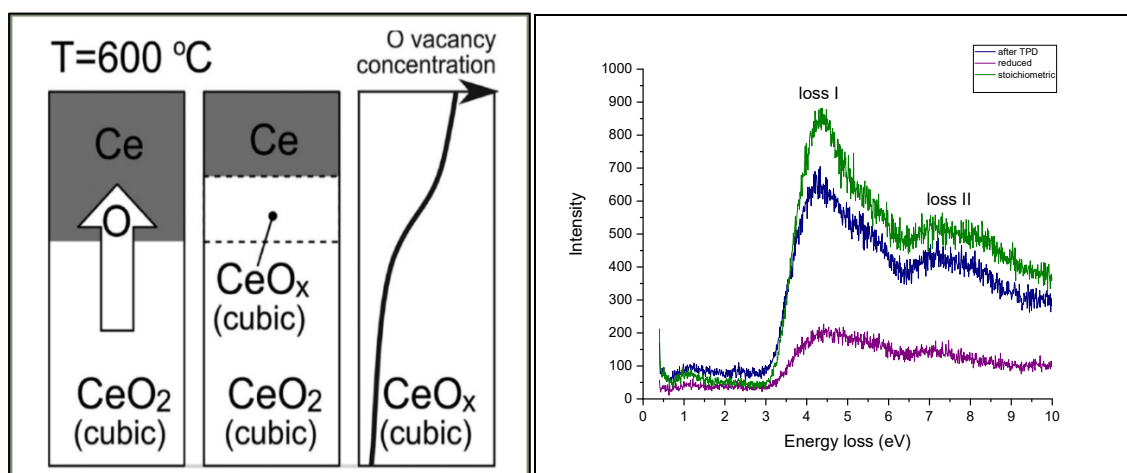
*Figure 51. The mechanism of the oxidation of the reduced CeO_x film triggered by annealing, adapted from [67]. EELS
spectrum of the reduced CeO_{2-x} after the TPD, with the intensity of the I loss explained by Duchon's mechanism.*

On the other hand, STM images show that the sample is in the irreversible state [Fig. 52].
The roughness of the sample is in the 6 nm range which is higher than before
hydrogenation. Moreover, one can still see cluster-like formations at the surface.
However, it is not clear whether this result refers to all the samples or only those prepared
in the STM chamber where the STM. Also, the LEED image shows similarities to the
reduced sample, with blurry spots and high intensity of the background, yet it is difficult
to judge if the sample is more reduced [Fig. 52].
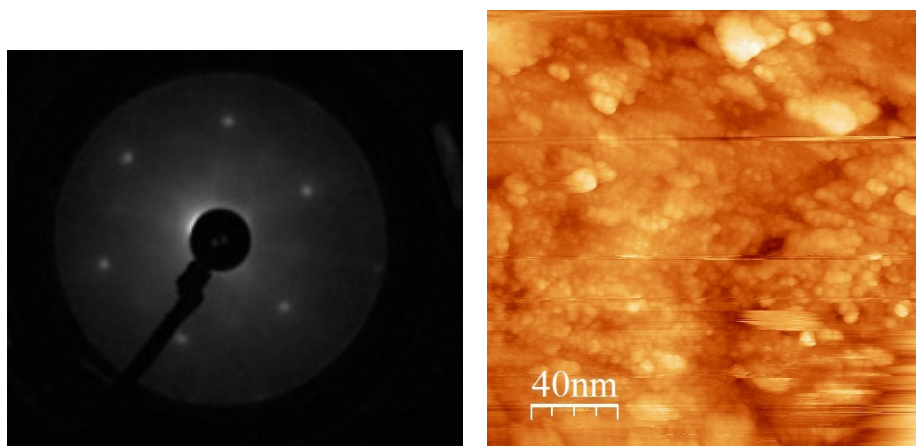
Figure 52 LEED image of the reduced sample obtained at 67 eV (on the left) and the STM image of the sample (on the right).

6.5 Summary

The described experiments demonstrate the influence of H_2 at the CeO_2 surface. As much as in the case of the stoichiometric film no difference in the state of the film was observed after the hydrogen treatment, the reduced sample interacts easily with the hydrogen molecule. Consequently, the sample is re-oxidized, with a possibility of hydride formation.
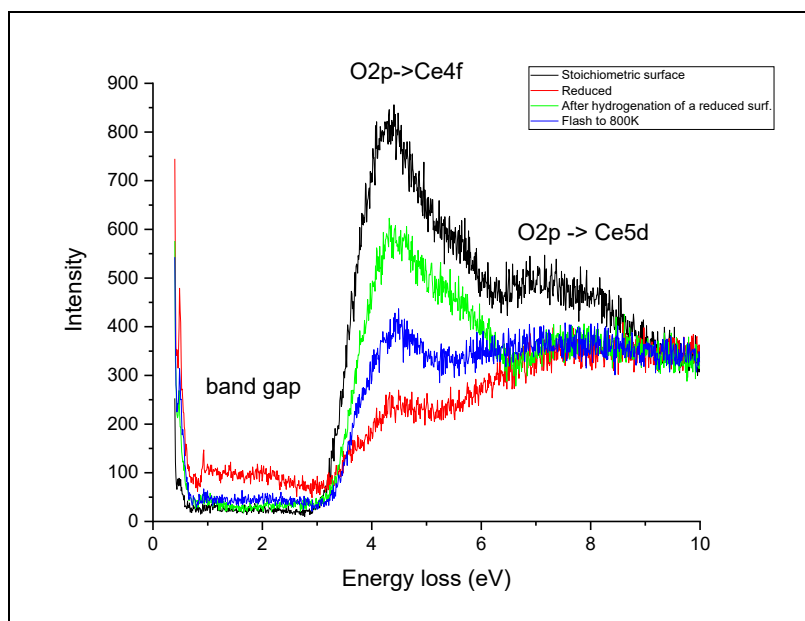
Figure 53. The summary of the EELS spectra obtained during the hydrogenation at room temperature. Stoichiometric

surface is compared to the reduced one, after hydrogen treatment, followed by flashing to 800 K.

EELS spectra show an increase of the intensity in the O2p- Ce4f transition region, which

is a fingerprint of the reduction state [Fig. 53]. That indicates that hydrogen is stabilized,

probably in the oxygen vacancies, with the possibility of forming hydride species.

Furthermore, in the HREELS spectra, there is a peak in the region where Ce-H vibrations

are expected. Due to annealing, hydrogen desorbs from the surface at about 550K

(probably from sub-surface) and 650K (surface). Additionally, STM studies show that

hydrogen changes the morphology of the film. As a result, I suggest that even though

after re-oxidation of the reduced film the electronic structure may seem very similar, the

film is changed irreversibly.

7. Hydride formation at high temperatures.

This chapter describes the adsorption and reaction of H_2 on CeO_2 (111) on the Ru (0001) at elevated temperatures (400-700K). Utilizing TPD, LEED, and HREELS, the adsorbed H_2 species were identified and their influence on the sample was examined.

Introduction

Experiments at elevated temperatures were inspired by a publication by Z. Wu et al, who reported for the first time direct experimental proof of formation Ce-H due to the interaction of H_2 with CeO_2. [66] The main method they used was inelastic neutron scattering (INS) spectroscopy, supported by IR, Raman, and DFT calculations.
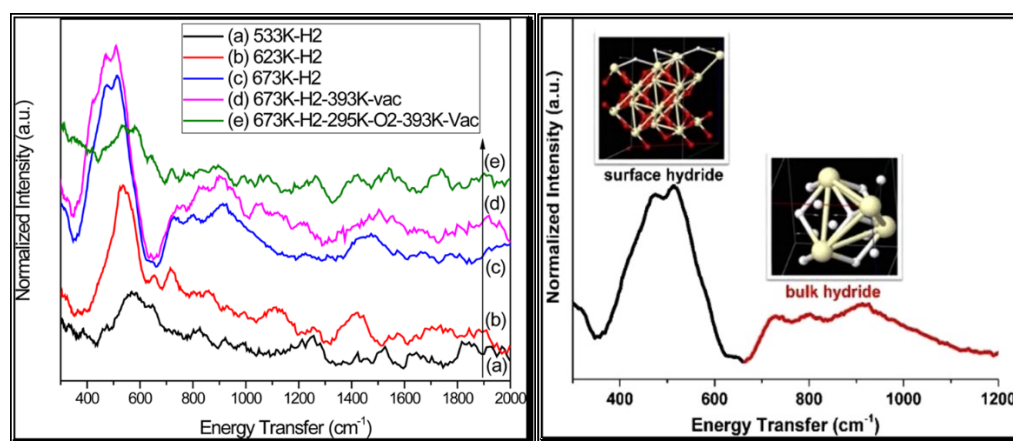
Figure 54 INS spectra of CeO₂ collected after H₂ treatment at various temperatures. Adapted from [66]

As shown in figure 54, after hydrogen treatment at 533K, reaction processes in a homolytic way- forming surface OH groups, seen as a wide feature around 575 cm^{-1}. After increasing the temperature to 623 K during hydrogen dosing, the strong band appears at 540 cm $^{-1}$ and it shifts to 495 cm^{-1} after treatment at 673 K. At the same time, a

broad feature in the range 650-1300 cm^{-1} starts appearing. After treating the sample with oxygen, both features disappear, which eliminates the origin of them in OH groups. Wu proposes that the features are representing the Ce-H groups, he supports this idea with the DFT calculations. As a result, they suggest the assignment of INS bands as follows:

Frequency range (cm^{-1})	Assignment of the vibrational modes
400-650	Ce-H deformation of surface hydride, CeH$_3$ local structures
750-1100	Ce-H deformation in bulk hydride, CeH$_2$ and CeH$_3$ structures
1300-1800	Combination and overtone of the two first modes

Figure 55. Suggest deformation modes, adapted from [66]

The aim of my experiment was to examine Wu's theory by using the same parameters during the experiment, but with thick CeO$_2$ film on Ru (0001) instead of nanorods. My main investigation methods were HREELS, LEED, and TPD.

Results and discussion

Stoichiometric CeO$_2$ was first flashed to 500 K to remove the contamination and then transferred to the high-pressure cell. After inserting the sample on the heating stage above the halogen lamp, it was exposed to molecular hydrogen. Then the sample was annealed at 400 K, 533 K or 670 K for 15 min, depending on the experiment. Each time the sample was heated with around 2 K/s rate. Hydrogen was pumped away from the high-pressure cell only after the sample was cooled down to the room temperature. Even though at RT the same film was usually employed in the series of experiments, here it was not always

possible to re-oxidize the sample to the stoichiometric form. In case of 500 K and 670 K treatment, hydrogen was so invasive, that the new film had to be prepared.

Figure 55. EELS spectra of the stoichiometric sample compared to results after treatment at 400, 533 and 600 K and the experimental results when the reduced sample was treated with hydrogen at 670 K.

Figure 55 shows results obtained after the hydrogen treatment at high temperatures, compared to the stoichiometric film. In the first experiment, hydrogen dosing took place at 400 K temperature. EELS spectrum from that temperature demonstrates advanced reduction of the CeO_2, with a strong peak in the band gap region coming from electrons at *f* orbital. However, HREELS [Fig. 56] spectrum shows very little change compared to the stoichiometric film, which is complementary to the results reported by Z. Wu. [66]. The next set of experiments was prepared at 533 K. Here, in the EELS spectrum the peak representing the transition of O2p to Ce4f (loss I) is even lower juxtaposed with the 400

K spectrum. The major difference is visible int the HREELS spectrum, with two peaks erasing. The first peak is in the range 800- 1200 cm^{-1}, followed by the second peak at 1200-1500 cm^{-1}.
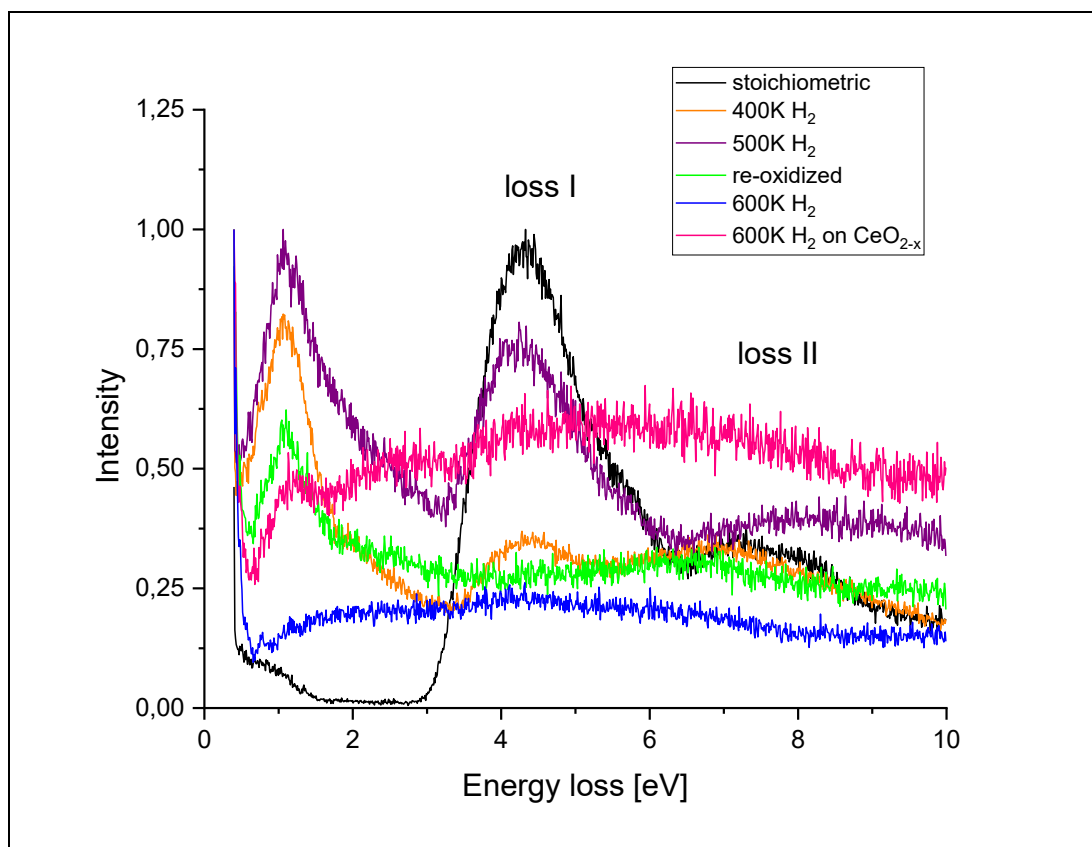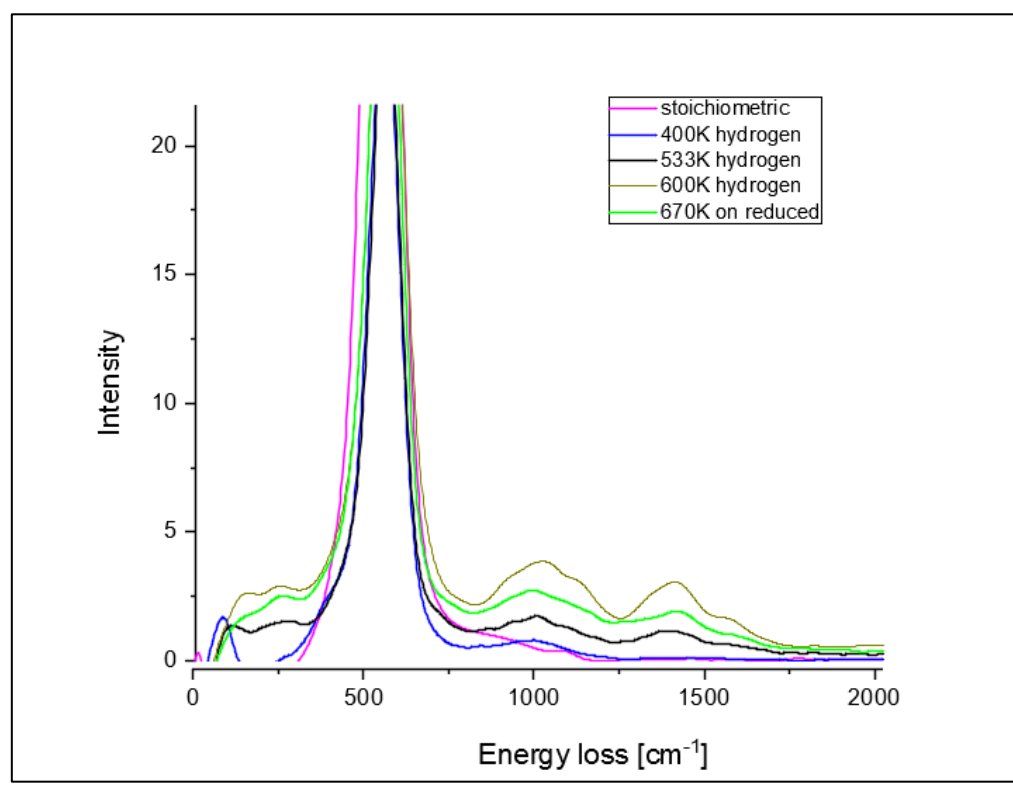

Figure 56. HREELS spectra of the stoichiometric sample compared to results after treatment at 400, 533 and 600 K and the experimental results when the reduced sample was treated with hydrogen at 670 K.

A special focus should be put on the band gap region. In this range, it is not yet clear if the intense peak is originating from the Ce4f or hydrogen adsorbed at Ru. The second case is possible if the film is de-wetted in an extensive way and starts cracking, exposing the metal. An additional experiment was performed on the reduced surface. The hydrogen was dosed at 670. In the consequence, very similar results to the stoichiometric film were obtained, but with even higher intensity in hydrogen species region [Fig. 56]. That behaviour suggests that oxygen vacancies induce the hydride formation.

Figure 57. TPD result of the CeO2 after hydrogenation at 400 K (on the left) at 600 K (on the right).

In order to follow the interaction of hydrogen with CeO_2, TPD experiments have been performed. Figure 57 shows curves obtained after the hydrogen treatment at 400 and 600 K. In the case of 400 K, there are weak desorption peaks in the 400-500 K range for both molecular hydrogen and CO. The presence of those peaks implies that the CeO_2 is reduced to the point w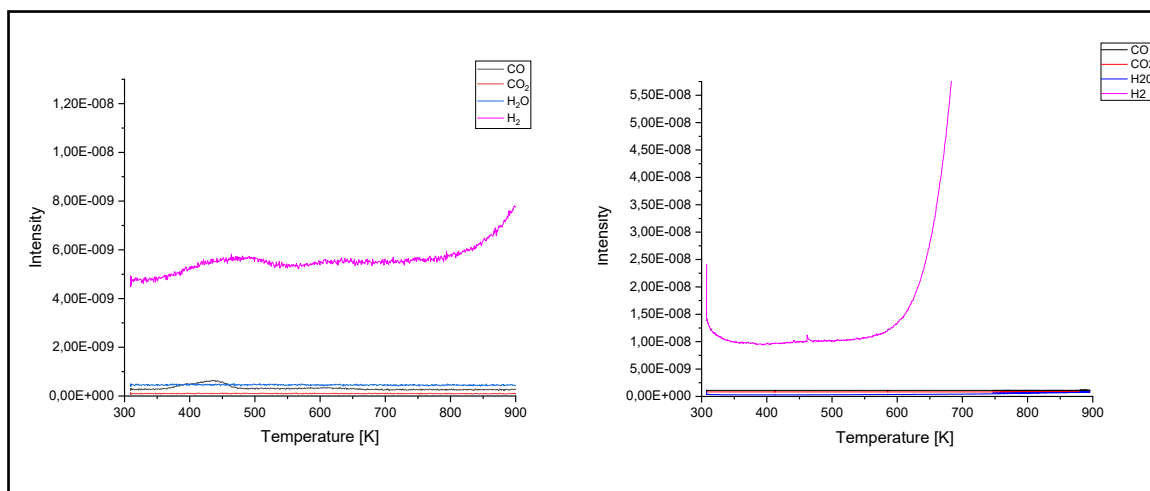here Ru is exposed. Probably at this temperature hydrogen is reducing the sample as seen in the EELS spectrum, by -OH formation, with a low amount of hydride. It cannot be seen in the H_2O desorption curve, due to the fact that the hydrogen treatment takes place at constant flow and any contamination is being immediately pumped away. The curves from the experiment at 600K demonstrate desorption of high amount of hydrogen. The peak increases rapidly from around 600 K., which is similar to the desorption after the hydrogen treatment at RT. There is also no contribution from CO anymore. As a reference, the same experiment was performed without the sample, proving that desorption does not occur from the part of the sample holder at lower than around 850 K temperatures. The intensity of the hydrogen curve must be coming from the hydride desorption, which formation was already suggested by the HREELS measurement discussed in the previous section.
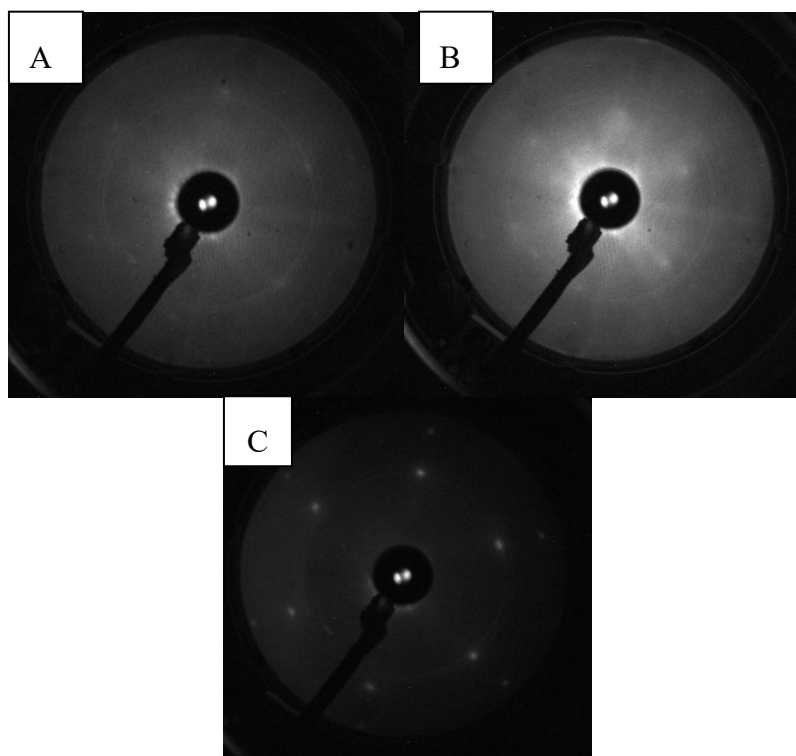
Figure 58. LEED images on the CeO2 after H2 treatment at 670K obtained at A) 67 eV B) 107 eV and C) at 400K obtained at 67 eV.

Analogous conclusions can be made from the LEED images. As shown above in figure 58 (A) and (B), after hydrogenation at 400K the film is reduced, with visible Ru (0001) peaks, which indicates de-wetting. The treatment at 670 K almost completely damages the surface; the peaks are hardly visible and blurry. Moreover, the intensity of the background is noticeably high.

Computational studies

The stability of the hydride in the CeO_2 (111) was calculated by a group of scientists from the Humboldt University in Berlin: Dr. Xiaoke Li, Dr. Joachim Paier, and Prof. Joachim Sauer. The calculations were performed using DFT+U method, described in detail in their paper. [68] First, they analysed the hydride formation at the surface of the reduced CeO_2 (111). With the agreement to my conclusions, after hydrogenation a layer of CeH_x is

formed, as shown on the models (Fig. 59). Moreover, Ce^{3+} close to the layer is oxidized to Ce^{4+}. They also suggest that hydride formation is an exothermic process. [68]
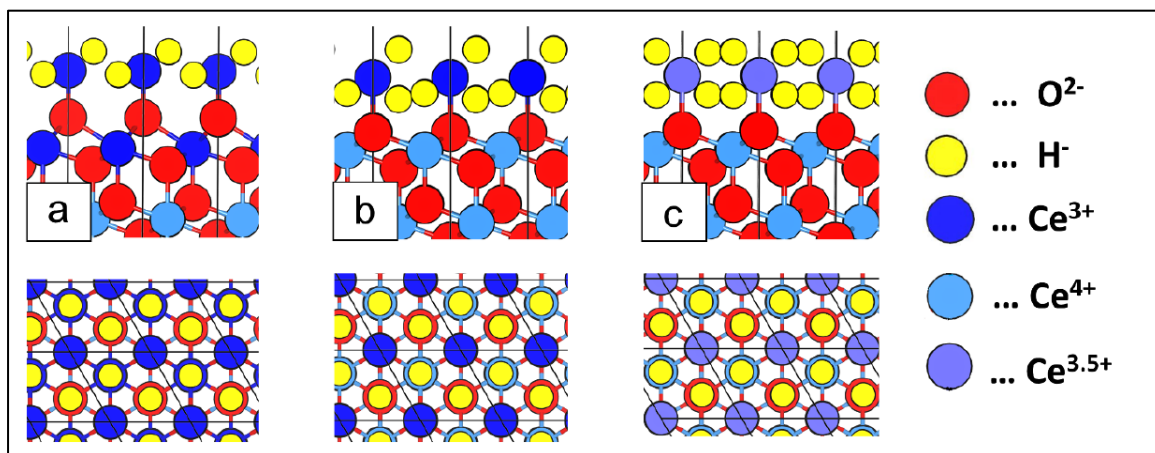
Figure 59. Modelss of the CeH_x structures across the layer (top row) and from the top (bottom row) of CeH_2 (a), CeH_3 (b), and CeH_4 (c). Adapted from [68]

The formation energies were calculated based on the give equation:

$$Ce_4O_6(111)\text{ -}(1\times1) + n/2\text{ } H_2 \rightarrow CeH_n\cdot Ce_3O_6(111)\text{ -}(1\times1) \text{ with } n = 2, 3, 4.$$
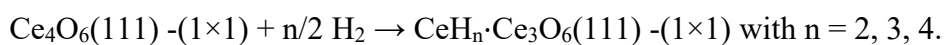
The calculated results and vibrational frequencies for various species of CeH_x (111) are presented in the table (Fig. 60). The vibrational frequency for Ce-H is in the range 967-1278 cm^{-1}, which directly corresponds with the HREELS results. [68]

Structure	Formation Energy [eV]		Vib. Frequency [cm-1] ν(Ce-H)
	PBE+U	HSE	
CeH	-1.85	-2.06	1278
CeH_2	-1.08	-1.41	1107
CeH_3	-0.37	-0.57	967

Figure 60. Calculated formation energies and vibrational frequencies for different CeH_x species. Adapted from [68].

Another aspect investigated by Li and his colleagues was the formation energy of hydrides at different degrees of $CeO_2(111)$ reduction. The calculations included single O vacancies, a pair of vacancies; and a cluster formed from 4 vacancies [Fig. 61].
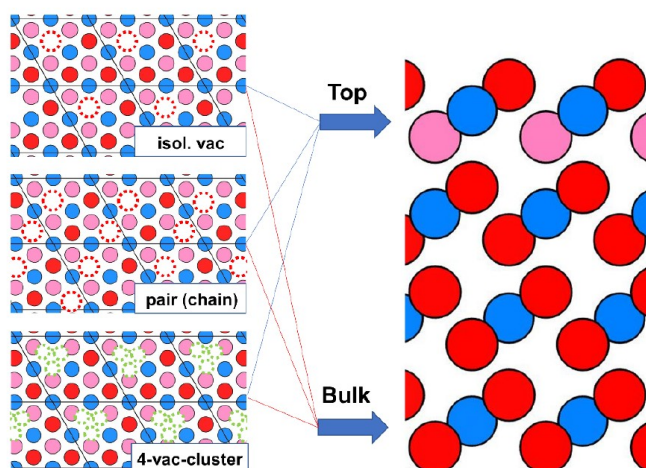
Figure 61. Illustration of O-vacancy structures required to calculate hydride formation energies. Adapted from [68].

The next calculations performed by Li and colleagues were regarding the position of the O vacancies. They calculated the formation energies for defects both on the surface and in the bulk, based on the model presented in figure 62.
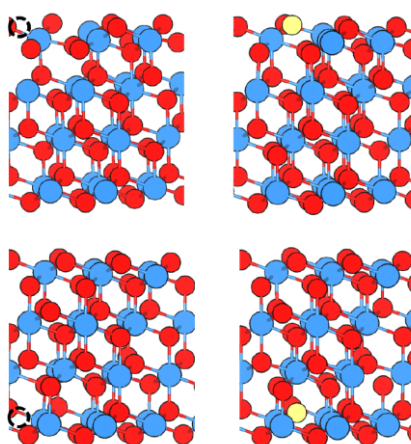
Figure 62. Models presenting different positions of O vacancies (on the left) and hydrogen incorporated in those defects (on the right). Adapted from [68]

The result shows that the formation of hydride in the bulk is more exothermic than on the surface. For example, the formation energies in case of a single vacancy are 0.44 eV for the surface and 0.01 eV for the bulk. For a pair of vacancies, they are 0.69 eV and -0.39 eV, respectively, with the biggest difference for the cluster vacancies- 0.62 eV surface and -0.83 for the bulk. [68] The presented results correspond with conclusions drawn in this thesis.

8. *Conclusions*

Vibrational action spectroscopy has been so far successfully applied only for gas phase aggregates. In this thesis, the first set-up for the method using infrared radiation from a free-electron laser on the solid surfaces was described. The results from the performed vibrational action spectroscopy experiments prove the high sensitivity of the method. During the experiments, it was possible to detect the characteristic V=O bond, located only at the surface of a thin $V_2O_3(0001)$ film on Au (111). We suggest that the rare gas atoms desorption was performed through the *direct vibrational coupling*, insensitive to bulk vibrations. The results were compared to those obtained with IRAS and HREELS. In both cases, vibrational action spectroscopy performs better due to the high resolution, surface sensitivity and no need of a reference spectrum. Another described here channel, observed for the TiO_2 (110) single crystal is thermal. Thermal desorption is induced by the heating up of the crystal, due to the absorption of the infrared light. The thermal channel can be minimised by adjusting the beam power and choosing the sample with better heat conductivity. Nevertheless, the method is a perfect tool for studying the vibrations at the surface with high sensitivity and resolution.

The second purpose of the presented thesis was to investigate the interaction of molecular hydrogen with stoichiometric CeO_2 (111) and reduced CeO_{2-x} (111), both at room and elevated temperature. A detailed description of the experiments including preparation, surface characterization, morphology and electronic state was presented. Experiments were carried out under the UHV conditions, using various surface science techniques including high resolution electron energy loss spectroscopy (HREELS) as well

as scanning tunnelling microscopy (STM), low energy electron diffraction (LEED) and temperature programmed desorption (TPD). The compilation of these techniques resulted in an exceptional outcome. At room temperature hydrogen does not interact with the stoichiometric CeO_2 surface. However, on the reduced CeO_{2-x} hydrogen induced some form of 'oxidation', when as seen on EELS spectra; Ce^{3+} is being oxidized to Ce^{4+}. The experiments observations were supported by the theoretical studies performed by Li *et al.*. The computational results show that suggested hydride formation on the reduced CeO_2 (111) is thermodynamically allowed. Hydrides incline the location near O vacancies, especially in agglomerates. The studies also support the suggestion that Ce^{3+} ions are re-oxidized to Ce^{4+}, with H species formed below the surface.

9.   Bibliography

[1]   J. Niemantsverdiet, Spectroscopy in Catalysis, Wiley-CH, 2007.

[2]   H.-J. Freund, "The Surface Science of Catalysis and More, Using Ultrathin Oxide Film as Templates: A Perspective," *J. Am. Chem. Soc.,* pp. 138, 8959-8996, 2016.

[3]   M. S. a. H.-J. Freund, "Properties of Oxide Surfaces," in *Surface and Interface Science: Properties of Composite Surfaces: Alloys, Compounds, Semiconductors*, Wiley-VCH, 2014, pp. 229-244.

[4]   J. A. Venables, Introduction to Surface and Thin Film Processes, Cambridge University Press, 2000.

[5]   D. R. Mullins, "The surface chemistry of cerium oxide," *Surf. Sci. Rep.,* pp. 70, 42-85, 2015.

[6]   R Mullins, P. Radulovic, S. Oversbury, "Ordered cerium oxide thin film grown on Ru(001) and Ni(111)," *Surf. Sci.,* pp. 429 (186-198), 1999.

[7]   K. Werner, X. Weng, F. Calaza, M. Sterrer, T. Kropp, J. Paier, J. Sauer, M. Wilde, K. Fukutani, S. Shaikhutdinov, H.-J. Freund "Toward an Understanding of Selective Alkyne Hydrogenation on Ceria: On the Impact of O Vacancies on H2 Interaction with CeO2(111)," *J. A. Chem. Soc.,* pp. 138, 17608–17676., 2017.

[8] Ch. Schilling, A. Hofmann, C. Hess and M. V. Ganduglia-Pirovano "Raman Spectra of Pollicrystalline CeO2: A Density Functional Theory Study," *J. Phys. Chem.,* pp. 121, 20834-20849, 2017.

[9] K. Sohlberg, S. Pantelides, S. J. Pennycook, "Interactions of Hydrogen with CeO2," *J. Am. Chem. Soc.,* pp. 123, 6609-6611, 2001.

[10] G. Vile, J. Bidier and J. Perez-Ramirez, "Ceria in Hydrogenation Catalysis: High Selectivity in the Conversion of Alkynes to Olefins," *Angew. Chem.,* pp. 51, 8620-8623, 2012.

[11] K.R. Asmis, A. Fielicke, G. v. Helden, G. Meijer, "Vibrational Spectroscopy of Gas-Phase Clusters and Complexes," in *The Chemical Physics of Solid Surfaces: Vol. 12, Atomic Clusters: From Gas Phase to Deposited*, Elsevier, 2007, pp. 327-375.

[12] W. Schöllkopf, S. Gewinner, H. Junkes, A. Paarmann, G.v. Helden, H. Bluem, A. Todd, "The new IR and THz FEL Fascility at the Fritz Haber Institute in Berlin," in *Advances in X-ray Free-Electron Lasers Instrumentation III*, 9512, 95121L.

[13] R. Egerton, Electron Elenrgy-Loss Spectroscopy in the Electrone Microscope, Springer, 1996.

[14] M. Rocca, L. Savio, "High Resolution Electron Energy Loss Spectroscopy (HREELS): a sensitive and versatile surface tool," in *Surface Science Techniques*, Springer, 2013, pp. 3-30.

[15] "Wikipedia," [Online]. Available:

https://images.app.goo.gl/NNQJobWTFvUQPgzf8.

[16] L. Vattuone, L. Savio, M. Rocca, "High Resolution Electron Energy Loss Spectroscopy (HREELS): A sensitive and Versatile Surface Tool," in *Surface Science Techniques*, Springer, 2013, pp. 499-528.

[17] H. Ibach and P. Hawkes, Electron Energy Loss Spectrometers: The Technology of High Performance, Springer Series in Optical Sciences, 1991.

[18] H. Ibach and D. Mills, Electron Energy Loss Spectroscopy and Surface Vibrations, Academic Press, 1982.

[19] R. Fuchs a. K. Kliewer, "Optical Modes on Vibration in an Ionic Crystal Slab," *Phys. Rev.,* pp. 140, 6A, 1965.

[20] A. Cox, W. Flawell and A. Williams, "Application of Fourier transform techniques to deconvolution of HREEL spectra," *Surf. Sci.,* pp. 153, 784-790, 1985.

[21] P. Atkins, Physical Chemistry, Oxford University Press, 2010.

[22] H. Lüth, Solid Surfaces, Interfaces and Thin Films, Springer, 2010.

[23] K. W. Kolasinski, Surface Science − Foundations of Catalysis and Nanoscience, Wiley, 2009.

[24] Z. Wu, A. Plucienik, F. Feiten, M. Naschitzki, W. Wachsmann, S. Gewinner, W. Scholkopf, H. Kuhlenbeck aand H.-J. Freund "Vibrational Action Spectroscopy of Solids: New Surface-Sensitive Technique," *PRL,* pp. 119, 136101, 2017.

[25] M. N. Huda, "Epitaxial growth of lateral graphene / hexagonal boron nitride heterostructures," (thesis), 2016.

[26] D. J. Harding, G. Meijer, A. Fielicke, S. M. Hamilton, W. S. Hopkins, S. R. Mackenzie, S. P. Neville and T. R. Walsch, "Probing the structures of gas-phase rhodium cluster cations by far-infrared spectroscopy" *J. Chem. Phys,* pp. 133, 214304 , 2010.

[27] J. A. Fournier, C. Wolke, C. Johnson, N. Heine, S. Gewinner, W. Schollkopf, T. Esser, M. Fagiani, "Site-specific spectral signatures of water molecules in the 'magic' H3O clusters in the regions of the OH streches and low frequency vibrations.," *PNAS,* pp. 111, 181327, 2014.

[28] S. Warnke, J. Seo, J. Boschmans, F. Sobott, J. Scrivens, M. Bowers, S. Gewinner, "Protomers of Benzocaine: Solvent and Permittivity Dependence," *J. Am. Chem. Soc,* pp. 137, 4236, 2015.

[29] J. Harding, T. R. Walsh, S. M. Hamilton, W. S. Hopkins, S. R. Mackenzie, P. Gruene, M. Haertelt, G. Meijer and A. Fielicke, "Communications: The structure of Rh+8 in the gas phase," *J. Phys. Chem. ,* pp. 132, 011101, 2010.

[30] K. R. Asmis, "Structure characterization of metal oxide clusters by vibrational spectroscopy: possibilities and prospects," pp. 14, 9270, 2012.

[31] K. Watanabe, " Laser-induced Reactions of Methane Adsorbed on Transition Metal surfaces," The Graduate University for Advanced Studies in Japan, 1998.

[32] J. W. Gadzuk, L. J. Richter, S. A. Buntin, D. S. King, and R. R. Cavangh "Laser-excited hot-electron induced desorption: a theoretical model applied to NO/Pt (111)," *Surf. Sci,* no. 344, L1252, 1995.

[33] C. E. Bartosch, N. S. Gluck, W. Ho and Z. Ying "Laser-surface-adsorbate interactions: Thermal versus photoelectronic excitation of Mo(CO)6 on Si(111)," *Phys. Rev. Letts.,* no. 57, 1425, 1986.

[34] F. Pfuner, J. Schoiswohl, M. Sock, S. Surnev, M. G. Ramsey and F. P. Netzer "The metal-insulator transition in V2O3(0001) thin films: surface termination effects," *J. Phys. Condens. MAtter,* p. 17(4035), 2005.

[35] F Pfuner, J. Schoiswohl, M. Sock, S. Surnev, M. G. Ramsey a. F. P. Netzer "The metal-insulator transition in V2O3(0001) thin films: surface termination effects," pp. 17,4035, 2005.

[36] M. Abu Haija, S. Guimond, A. Uhl, H. Kuhlenbeck, H.-J. Freund, "Adsorption of water on thin V2O3(0001) films," *Surf. Sci.,* pp. 600, 1040-1047, 2006.

[37] M. Abu Haija, S. Guimond, Y. Romanyshyn, A. Uhl, H. Kuhlenbeck, T. K. Todorova, H.-J. Freund, " Low temperature adsorption of oxygen on reduced V2O3(0001) surfaces,," *Surf. Sci.,* pp. 600, 1497–1503, 2006.

[38] J. T. Yates and C. Powell, "Methods of surface characterization," in *Vibrational Spectroscopy of Molecules on Surfaces*, Springer Science+ Business, 1978.

[39] D. Gobke, Y. Romanyshyn, S. Guimond, J. M. Sturm, H. Kuhlenbeck, J. Döbler, U. Reinhardt, M. V. Ganduglia-Pirovano, J. Sauer, H.-J. Freund, "Formaldehyde formation on vanadium oxide surfaces V2O3(0001) and V2O5(001): how does the stable methoxy intermediate form?," *Angew. Chem. Int. Ed.,* pp. 48,3695, 2009.

[40] H. Schlichting, "Ph.D thesis," Technische Universitat München, 1990.

[41] F.E. Feiten, J. Saifert, J. Paier, H. Kuhlenbeck, H. Winter, J. Sauer and H.-J- Freund, "Surface Structure of V2O3 (00=1) Revisited," *Phys. Rev. Lett.,* pp. 114, 216101, 2015.

[42] H. Abu Haija,M. Guimond, S. Romanyshyn, Y. Uhtl, H. Kuhlenbeck, T. T. G.-P. M. D. J. H.- J. Freund. *Surf. Sci.,* pp. 600, 1497, 2006.

[43] N. Ashkenov, S. Schloche, T. Hofmann, R. Korlacki, T. E. Tiwald and M. Schuber "Infrared dielectric anisotropy and phonon modes of rutile," *Journal of Applied Physics,* no. 16,133, 2013.

[44] A. Trovarelli and P. Fornasiero, Catalysis by Ceria and Related Materials, Imperial College Press, 2013.

[45] S. Gridchneller and M. Reichling, "Structural Elements of CeO2 (111) surfaces," *Nanotech.,* pp. 18, 044024, 2007.

[46] N.V. Skorodumova, R. Ahuja, S. I. Simak, A. Abriskosov and B. I. Lundqvist, "Electronic, bonding and optical properties of CeO2 and Ce2O3 from first principles," *Phys. Rev.,* pp. 64, 115108, 2001.

[47] N.V. Skorodumova, S. Simak, B. I. Lundqvist, I. A. Abrikosov and B. Johansson, "Quantum Origin of the Oxygen Storage Capability of Ceria," *Phys. Rev. Lett.,* pp. 89, 166601, 2002.

[48] D. R. Mullins, P. M. Albrecht and F. Calaza "Variations in Reactivity on Different Crystallographic Orientations of Cerium Oxide," *Top Catal.,* pp. 56, 1345-1362, 2013.

[49] Joon B. Park, J. Graciani, J. Evans, D. Stachiola, M. Shuguo, J. Rodriguez, "High catalytic activity of Au/CeOx/TiO2(110) controlled by the nature of the mixed-metal oxide at the nanometer level Akira Nambu, Javier Fernández Sanz, Jan Hrbek, and José A. Rodriguez," *Proc. Natl. Acad. Sci.,* pp. 106, 4975-4980, 2009.

[50] X. Wang, J. H. Rodriguez, D. Gammara, M.-A. Arias, M. Fernandez-Garcia, "In situ studies of the active sites for the water gas shift reaction over Cu-CeO2 catalysts:

complex interaction between metallic copper and oxygen vacancies of ceria.," *J Phys Chem B.* , pp. 110, 428-434, 2006.

[51] M Baron, O. Bondarchuk, D. Stacchiola, H.-J. Freund, "Interaction of gold with cerium oxide supports: CeO2(111) thin films vs CeOx nanoparticles," *J PHYS CHEM,* pp. 113, 6042-6049, 2009.

[52] N. Lopez and M. Garcia-Melchor, "Homolytic Products from Heterolitic Paths in H2 Dissosiation on Metal Oxides: The example of CeO2.," *J. Phys. Chem.,* pp. 118, 10921-10926, 2014.

[53] M. Veronica Ganduglia-Pirovano, F. D. Silva and J. Sauer "Density-Functional Calculations of the Structure of Near-Surface Oxygen Vacancies and Electron Localization on CeO2(111)," *Phys. Rev. Lett.,* pp. 102,026101, 2009.

[54] T. Monitini, M. Melchiona, M. Monai and P. Fornasiero "Fundamentals and Catalytic Applications of CeO2- Based Materials," *Chem. Rev.* , pp. 116, 5987-6041, 2016.

[55] S. Grintschneder and M. Reichling, "Structural elements of CeO2 (111) surfaces," *Nanotech.,* pp. 18, 044024, 2007.

[56] C. Barth,C. Laffon, R. Olbrich, A. Ranguis, P. Parent and M. Reichling "A perfectly stoichiometric and flat CeO2(111) surface on a bulk-like ceria film," *Sci Rep.,* pp. 6, 21165, 2016.

[57] Y. Seminovski, P. Tereshchuk, A. Kiejna, and J. L. F. Da Silva "The role of the cationic Pt sites in the adsorption properties of water and ethanol on the Pt4/Pt(111) and Pt4/CeO2(111) substrates: A density functional theory investigation," *J. Phys. Chem,* pp. 145, 124709, 2012.

[58] F. Shahed, A. Beniya, H. Hirata, T. Watanabe, "Morphology of size-selected Ptn clusters on CeO2(111)," *Surf. Sci. ,* pp. 628, 30–35, 2014.

[59] Y. Gao, R. Li, S. Chen, L. Luo, Ti. Caoa and W. Huang, "Morphology-dependent interplay of reduction behaviors, oxygen vacancies and hydroxyl reactivity of CeO2 nanocrystals," *J. Phys. Chem. C ,* pp. 117, 5800–5810, 2013.

[60] A. Pfau and K. Schierbaum, "The electronic structure of stoichiometric and reduced CeO2 surfaces: an XPS, UPS and HREELS study," *Surf. Sci.,* pp. 321, 71-80, 1994.

[61] K. Schierbaum, W. Göpel and A. Pfau, "The electronic structure of CeO2 thin films: the influence of Rh surface dopants," *Surf. Sci.,* pp. 331-333, 1479-1485 , 1995.

[62] F. Esch, S. Fabris, L. Zhou, T. Montini, C. Africh, P. Fornasiero, "Electron Localization Determines Defect Formation on Ceria Substrates," *Science,* pp. 752, 2005, 309.

[63] B.-T. Tenga S-Y Jianga, Z-X Yang, M-F Luoa, Y-Z Lana, "A density functional theory study of formaldehyde adsorption and oxidation on CeO2(1 1 1) surface," *Surf. Sci.,* pp. 576, 217, 2015.

[64] F. Buatier de Mongeot, M. Sherrer, B. Gleich, E. Kopatzki,. R. Behm, "CO adsorption and oxidation on bimetallic Pt/Ru(0001) surfaces-– a combined STM and TPD/TPR study," *Surf. Sci.,* pp. 411, 249–262, 1998.

[65] G. Vilé, S. Colussi, F. Krumeich, A. Trovarelli, J. Perez-Ramirez, "Opposite face sensitivity of CeO_2 in hydrogenation and oxidation catalysis.," *Angew Chem Int Ed Engl,* pp. 45, 12069-72, 2014.

[66] Z. Wu, Y. Cheng, F. Tao, L. Damen, G. Shiou Foo, L. Nguyen, X. Zhang, A. Beste and A. J. Ramirez-Cuesta "Direct Neutron Spectroscopy Observation of Cerium Hydride Species on a Cerium Oxide Catalyst," *J. Am. Chem. ,* pp. 139, 9721-9727, 2017.

[67] T. Duchoň, J. Hackl, J. Höcker, K. Veltruska, V. Matolin, J. Falta, S. Cramm, S. Nenayake, C. M. Schneider, "Exploiting micro-scale structural and chemical observations in real time for understanding chemical conversion: LEEM/PEEM studies over CeOx–Cu(111).," *Ultramicroscopy,* pp. 183, 84-88, 2017.

[68] X. Li, J. Paier, J. Sauer, "arxiv.org Condensed Matter," 2019. [Online]. Available: arXiv: 1904.13200..

Frequently used abbreviations

E_{des}	Desorption activation energy (adsorption energy)
FWHM	Full width at half maximum
HOMO	Highest occupied molecular orbital
HREELS	High resolution electron energy loss spectroscopy
hv	Photon energy
IRAS	Infrared reflection absorption spectroscopy
K	Kelvin
LEED	Low energy electron diffraction
LUMO	Lowest unoccupied molecular orbital
QMS	Quadrupole mass spectrometer
STM	Scanning tunnelling microscopy
TPD	Temperature programmed desorption
UHV	Ultrahigh vacuum

Acknowledgments

When I arrived to the FHI for the job interview, it was the first the in my life that I saw an UHV chamber. Now, after 4 years of work, I can proudly say that I start to understand what I'm doing. I am grateful to each person in the department for making my life easier.

I'm especially thankful to Prof. Hans-Joachim Freund for giving me a chance. Your decision to hire me changed my life. Thank you for all the support and supervision. I also thank Prof. Hildebrandt for his kind support as my second supervisor. This thesis couldn't be made without one special person- Helmut Kuhlenbeck. Thank you for all the inspiring discussions, hours of talking about science and life. I wish everyone to have a group leader like you.

I thank Matthias Naschitzki and Walter Wachsmann for patiently answering all my questions and taking care of the machines. You are silent heroes of the Institute. I also thank Uwe Härtel for technical and moral support. I am grateful to Klaus Peter Vogelgesang for also being there for me. I thank Manuela Misch and Daniela Nikolaus for their kind and professional help in everything that needed to be organized.

Over those 4 years I met many amazing people. I especially thank Smadar Attia, Heloise Tissot, Giulia Berti, Francesca Mirabella, Earl Davis and Kristin Werner for many funny moments that help me go through the hard times. I also thank all my other colleagues. Sometimes a simple 'Hello' or a smile can improve somebody's day.

With my whole heart I would like to thank Marc Zaku. You are the most amazing person in my life, and I adore and value you so much. I appreciate your care and support, thank you for always being there for me!

Specjalne podziękowania należą się mojej rodzinie. Dziękuję moim rodzicom za to ze dali mi wszystko- wsparcie, miłość i wiarę w zwycięstwo. Moje sukcesy są miarą waszej pracy. Dziękuję mojej siostrze- najlepszej przyjaciółce, za lata pełne śmiechów i wzruszeń. Jesteś moja inspiracją. Na koniec dziękuję mojej babci i dziadkowi za ciepło i cierpliwość każdego dnia.

Publications:

1. Z. Wu, A. Plucienik, Y. Liu, M. Naschitzki, W. Wachsmann, S. Gewinner, W. Schöollkopf, H. Kuhlenbeck and H.-J. Freund, *Surface action spectroscopy with rare gas messenger atoms,* Rev. Sci. Instrum. *89, 083107 (2018)*

2. Z. Wu, Agata Płucienik, F. E. Feiten, M. Naschitzki, Walter Wachsmann, S. Gewinner, W. Schöllkopf, V. Staemmler, H. Kuhlenbeck and H.-J. Freund,
 Vibrational Action Spectroscopy of Solids: New Surface-Sensitive Technique, PRL 119, 136101 (2017)

3. N. F. Richte, F. E. Feiten, J. Pal, A. Plucienik, E. Emmez, S. Shaikhutdinov, H. Kuhlenbeck, T. Risse, H.-J. Freund, I. Goikoetxea, R. Włodarczyk, J. Sauer, *Characterization of Phonon Vibrations of Silica Bilayer Films*, J. Phys. Chem. C2019123,127110-7117

Selbstständigkeitserklärung

Hiermit erkläre ich, die Dissertation selbstständig und nur unter Verwendung der angegebenen Hilfen und Hilfsmittel angefertigt zu haben. Ich habe mich nicht anderwärts um einen Doktorgrad in dem Promotionsfach beworben und besitze keinen entsprechenden Doktorgrad. Die Promotionsordnung der Mathematisch-Naturwissenschaftlichen Fakultät, veröffentlicht im Amtlichen Mitteilungsblatt der Technische Universität Berlin, habe ich zur Kenntnis genommen.

02.09.2019 Berlin

Selbstständigkeitserklärung